# Inkjet Structuring on Electrode Surfaces

**Dissertation**
**zur Erlangung des Grades eines Doktors der Naturwissenschaften**
**-Dr. rer. nat.-**

Von

Ina Rianasari

aus

Indonesien

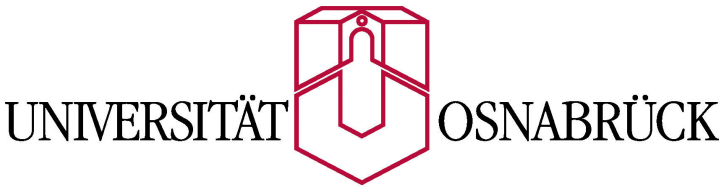


Fachbereich Biologie / Chemie

Institute für Chemie

Osnabrueck 2010

Die experiementallen Arbeiten wurden von Januar 2006 bis August 2009 im Institutes für Chemie der Universität Osnabrück unter der Leitung von Herrn. Prof. Dr. Lorenz Walder durchgeführt.

# Acknowledgements

First and foremost, I give thanks and honor to God for giving me strengths and abilities to accomplish so many things in my life.

Here, I would like to thank those who made my research experiences in the University of Osnabrueck are so fulfilling. I would like to express my sincere gratitude to my *Doktorvater* Prof. Lorenz Walder for his guidance throughout my research. He provided me flexibilities in exploring my research and guided me to express myself. I also appreciate the discussion and knowledge about Marangoni with Prof. Uwe Beginn. I would also thank the group members: Tesfaye, Burkhardt, Christine, Simona, Claudia, Alina, Dereje, Kathir, Holger, Dirk, Tamara, Benedik, and Angelina. The life in the lab will not be joyful without you guys. Our lunch discussions which were “not always about science” - themes are unforgettable. Aside from the group members, I would thank Frau Ripenhausen for helping me with my visa at my early stage at University of Osnabrueck.

I would also like to thank to Prof. Gunter Wittstock and his group members at University of Oldenburg. The collaboration opened significant results of my research. For Malte Burchardt, I really appreciate your hospitality and kindness during my visits in the group. Special thanks also go to Izabella Brandt, for PMIRRAS measurements which provided further insight.

The sweetest greeting goes to my parents. Your pray, blessings, and unconditional love always accompany me. Thank you for teaching me to understand the values of life. For my best friend and husband Reza, I am grateful for your love and supports. Let’s continue our journey. For my brothers and sister, your supports keep my spirits alive. The last but not least, Indonesian friends in Osnabrueck: Ida, Tira, Diah and Sri. You always cheer me up and ease my home sick.

# Table of Contents

# Chapter 1 : INTRODUCTION

## 1.1 Overview of Inkjet Printing Technology

Inkjet printing is considered as an emerging technology and has been pursued into an important structuring technique. The inkjet printing technique has been applied in various fields, both on pilot lab- and industrial scales, such as electronic circuitry and display technology[1-3], combinatorial studies of new materials[4, 5], biological application[6-8] (cell patterning or tissue engineering) and so forth. These emerging applications are due to the inherent ability of inkjet to deliver a picolitre volume of drops which are fired from its nozzles at the printhead. The ordinate positions of drops can be addressed in a precise manner by utilizing a microtranslation stage which is usually already built-in in the printing system. Complex patterns can be easily created and realized since most of the inkjet printers are computer controlled and compatible to many graphic softwares. Even 3D structuring is possible by repetitive jetting over the same region. Inkjet printing is also termed as so-called “direct writing” technique, whereby no mask is required to create a relief of patterns, in contrast to lithography, this leads to a reduction of process steps and, therefore, increases the economic value. During printing, no contact actions are involved which reduces the possibility of cross contaminations between inkjetted substances or materials. Inkjet printing is also considered as a flexible and a high throughput technique. It allows to print different materials using multiple reservoirs and the printing area can be below 1 $cm^2$ up to several $m^2$.

The history of inkjet printing was started by a study of liquid drop generation by Lord Rayleigh in1878[9]. Herein, a pressure wave was induced to a liquid stream which breaks the stream into regular drops (Figure 1.1). It took about a century until Richard G. Sweet discovered that such a drop generated from the liquid stream can be controlled upon application of charges. The findings turned out to be key point of further developments and led into an economic commercialization of the inkjet printer which is used in almost every household today.

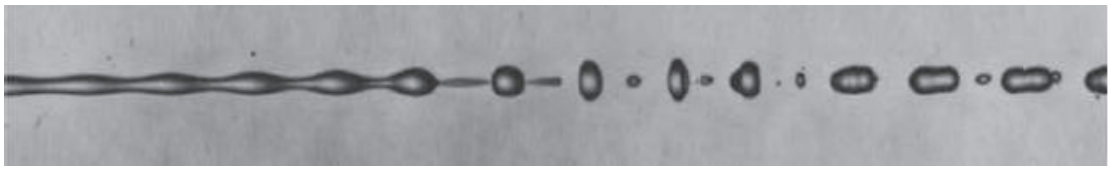

**Figure 1.1** The phenomenon of Rayleigh instability droplets formation in a liquid jet which is driven by surface tension.[10]

According to the path on how drops are generated, inkjet printing is classified into two classes: continuous inkjet and drop-on-demand inkjet.

(i) Continuous Inkjet[11, 12]

Continuous Inkjet has been widely used in industry for labeling and coding products or packages (see Figure 1.2). The working principle is what Richard Sweet has implemented. The contractions of a piezo element attached on the dispenser breaks the liquid into regular, uniform

drops. The induced charge on the drops can be used to control and address the drops to desired positions on the substrate underneath. The less charged or uncharged drops are collected by a gutter and brought back to the ink dispenser. The process continues until a pattern is produced. The process is fast but less efficient, because many drops are lost in the deposit and do not reach the substrate. In addition, the resulting patterns have low resolution.

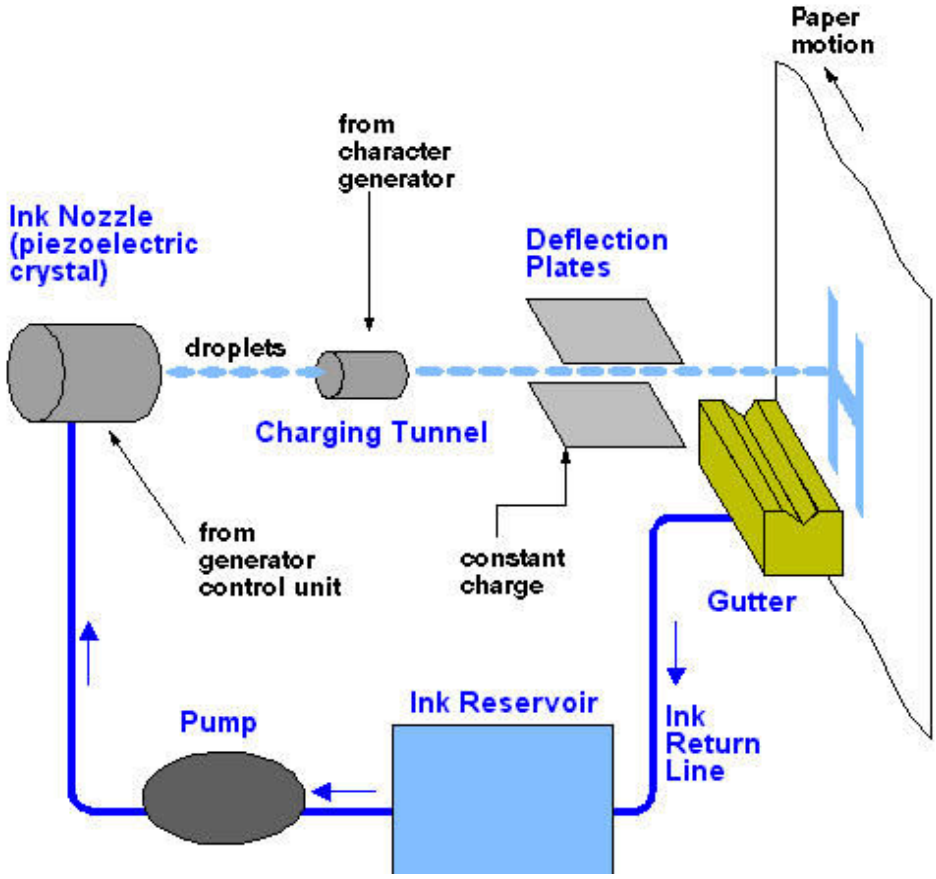


**Figure 1.2** The scheme of working principle in the continuous inkjet printer (courtesy of Computer desktop encyclopedia).

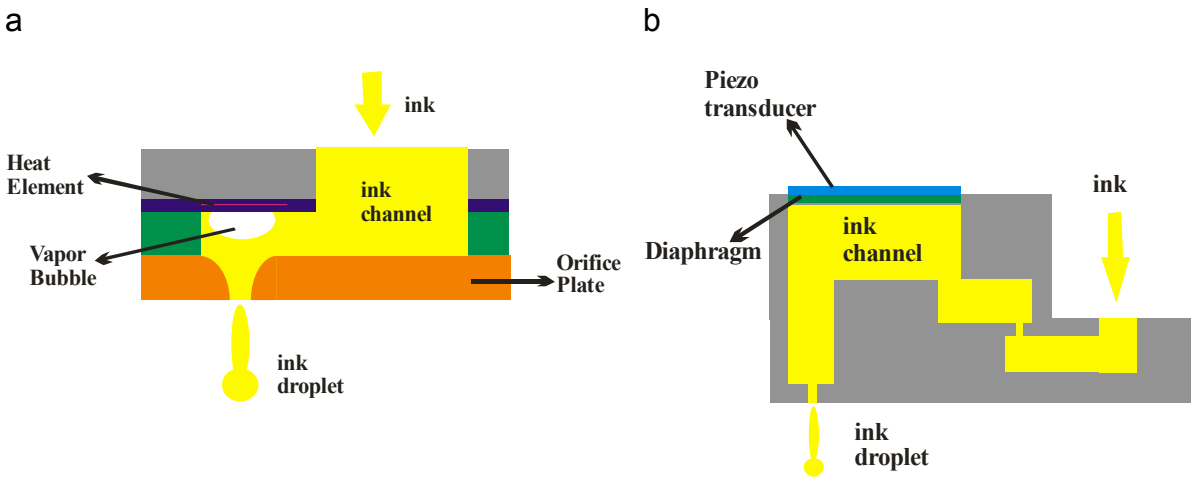


**Figure 1.3** Schemes of cartridge used according to the type of inkjet printer: thermal–based inkjet printer (a) and piezo–based inkjet printer (b). The schemes are adapted from Eric Hanson, Society of Imaging Science and Technology.

(ii) Drop-on-Demand Inkjet

In the drop-on-demand inkjet system, microsecond pulses regulate the drops generation and more importantly, the drops can be shot to certain positions. Two types of printers belong to this system, the thermal inkjet printers and the piezo inkjet printers (Figure 1.3). In the thermal inkjet printers, small current pulses regulate the drop formation. The current pulses thermally produce a vapor bubble inside the ink reservoir and consequently increase the internal pressure. A portion of liquid is driven outside and accumulated at the nozzle tip as a pendant drop. As soon as the vapor bubble collapses, the pendant drop is fired toward the surface. The generation and collapse of vapor bubbles is repeated until a desired

pattern is produced. In the piezo inkjet printers, small pressure pulses produced from the contraction and retraction of a piezo element regulate the generation of drops. For the purpose of printing organic substance from solutions, as it is demonstrated in this work, a piezo inkjet printer is more preferable compared to a thermal inkjet printer. The heating process and the development of vapor bubbles inside the ink reservoir (cartridge) of a thermal inkjet printer could restrict its use to thermally non-sensitive substances.

In this work, a piezo-based inkjet printer is used, a modified EPSON stylus photo R200. Principally, the ejection process of drops in a piezo inkjet printer based on DoD is based on acoustic waves disturbance which results from the micro voltage pulse applied to the piezo element.[13-15] Figure 1.4 shows a scheme of a microdispenser attached to a piezo element surrounding the dispenser's outer wall. In the capillary, the open end connects to the ink reservoir while the close end connects to the nozzle tip, through which drops are ejected. As a voltage is applied to the piezo element, the volume of the dispenser is expanded, which leads to a generation of pressure waves inside the capillary (Figure 1.4(b – 1)). The pressure splits into two waves of equal magnitude traveling in opposite directions. They are reflected back at the capillary ends (Figure 1.4(b – 2 and 3)). Since there is a large difference in diameter between the open and close ends, the wave reflected from the open end reverses its phase. Both waves then collide at a mid point inside the capillary (Figure 1.4(b – 4)). This causes a pressure drop inside the capillary and generates a compression force in the liquid due to capillary inward

contraction. As a result, the compression force doubles the pressure of the reflected fluid wave reflected from the open end (Figure 1.4(b – 5)). The wave then travels, approaches the nozzle tip and pushes the liquid pendant to the air (ejection) (Figure 1.4(b – 6)). The drop ejection happens only if the pressure magnitude is higher than the surface tension, i.e. the force that holds the fluid pendant at the nozzle tip.

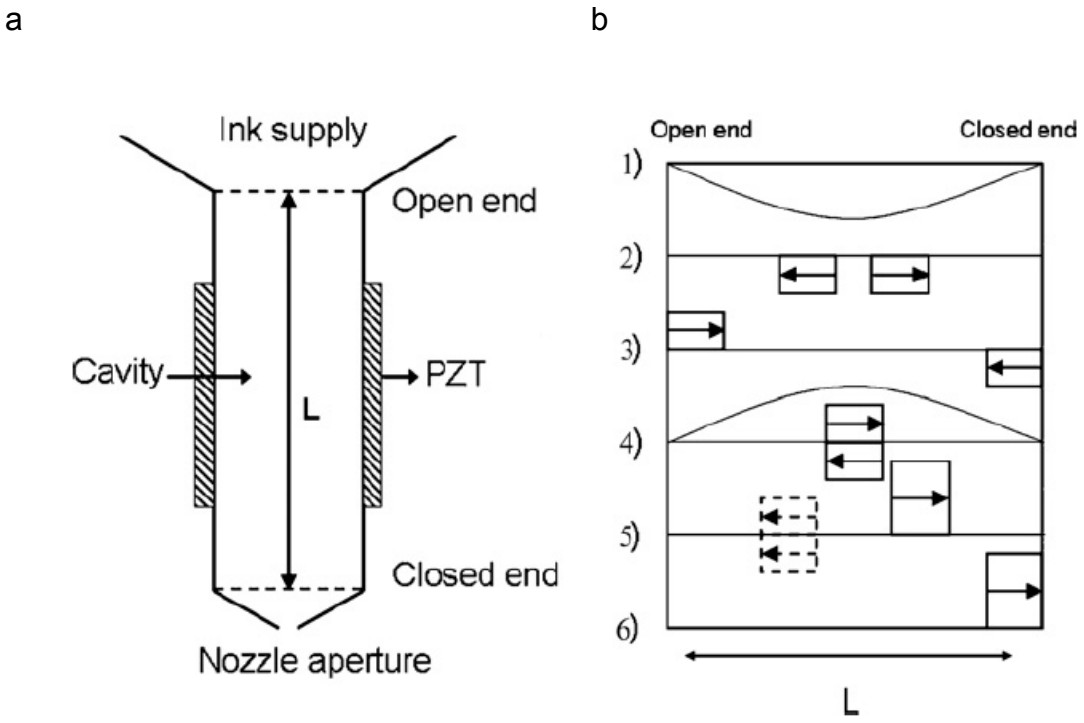


**Figure 1.4** The process of drops generation inside piezo–based inkjet printer.

In numerous experiments, it is observed that the liquid jet may break up into smaller drops, i.e. a drop is accompanied by a satellite. The satellites are

usually considered as defects in printing process because they disturb the precision of drop deposition on a surface.

A stroboscopic photographic system has become a standard method to study the drop and satellite formations.[16-18] The temporal resolutions of capturing the flying drops can reach the time range of 250 ns with an interframe time of 1 μs.[19] Such a high speed photographic system provides detailed analysis of the entire drop formation and propagation process.

The formation of satellite(s) is often observed due to capillary pitching of the tail of the free liquid jet. The capillary pitch is affected by the ink properties and by the printing parameter adjusted. [18, 20-22] A recent experimental study on the drop generation featured that a drop can be recombined with the satellite during the flying toward a surface underneath.[22] This recombination depends on the final velocity and size of the primary drop and the satellite.

This work focuses on the applications of inkjet printing technique to immobilize monolayers on gold and also as a tool to deliver nano grams of organic nanoparticles. General overviews of thiolate monolayers and printing of inorganic materials, i.e. oxide nanoparticles, will be described in the following sections.

## 1.2 Self–Assembled Monolayers (SAMs) of Thiolates on Gold Surfaces

Self – assembly is a spontaneous organization of molecular constituents which results in a high degree of molecular orientation, order and packing. In biological systems, such as cells, proteins or viruses encounter self–assembly is often observed and may lead to well-ordered molecular and supramolecular arrays.[23, 24] Besides living systems, many organic and inorganic systems show

self-assemble mechanism.[24, 25] Molecular order, nanosized–systems, multifunctionality sites, and surface–interface phenomena can be achieved or are related to self–assembly. This work will not emphasize on all self–assembled monolayer systems but rather on the thiolates deposited on gold surfaces. More general, comprehensive descriptions of monolayer systems have been described elsewhere.[26-29]

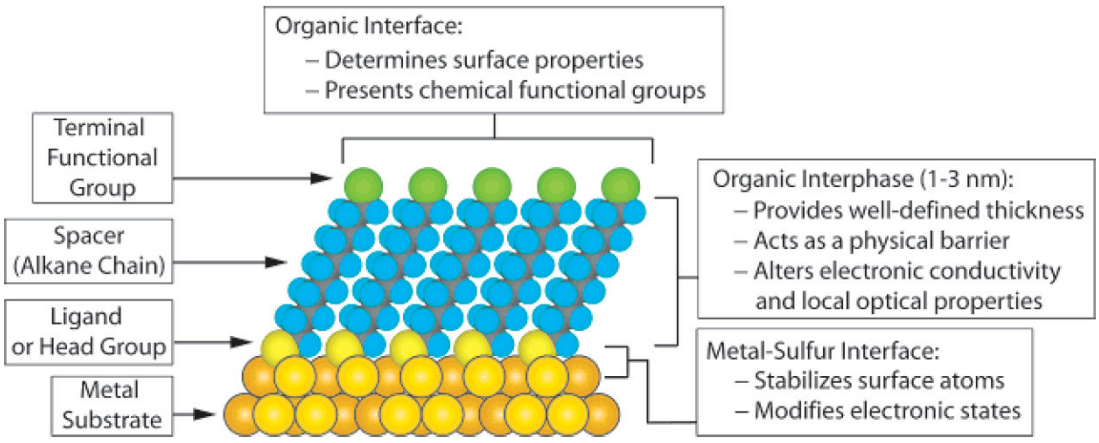


**Figure 1.5** The schematic of the commensurate molecular arrangement structure of alkanethiolates on Au(111).[28]

Self–assembled monolayers of thiolates are formed by spontaneous chemisorption of the thiolate headgroups from solutions or from vapor onto a noble metal surface. Thiolate monolayers have been considered as a convenient and simple method to tailor surface–interface properties and nowadays, they are commercially available. Figure 1.5 shows a scheme of

thiolates on a gold surface (111). The sulfur headgroup cleaves and facilitates the specific affinity to the gold surface according to the following reaction: [30, 31]

$$Au_{(s)} + R\text{-}SH_{(solv)} \leftrightarrow RS - Au_{(s)} + \tfrac{1}{2}H_{2(solv)}$$

From the reaction above, the thiolates in the solution are directly attached on the surface and release hydrogen. The reversible character of the reaction indicates that the coverage is formed in a dynamic equilibrium.[31-33] The evidence stems from scanning probe microscopy methods.[27, 33-35]

The height of a thiolate is defined by the spacer length which normally consists of an alkane chain. The van der Waals interactions between alkane chains play a role in the order and packing density of the thiolates. Functional groups on top of a thiolate chain provide not only the surface properties (i.e. hydrophobic or hydrophilic) but also act as templates allowing the anchoring of further building blocks.

The rate of formation of thiolates on gold surfaces has been thoroughly investigated.[26, 29, 36-38] Many factors affect the quality of the monolayers, in essence the crystalinity of the molecular structure, as a function of length of the thiolate spacer, concentration, solvent used, temperature, cleanliness of the gold substrate, and so forth. In general, the mechanism of growth of thiolates from solution involves two time regimes.[26, 36, 39, 40] At the first regime (i.e. within a few minutes), about 90 % of a surface is covered. In this stage the thiolates are initially adsorbed in a lying–down phase. As the immersion time progresses, the surface coverage increases and the thiolates are then in a standing–up phase, creating well–separated islands. The isolated islands of thiolates then

grow and touch each other. The second regime involves the reorganization on the molecular level and results in the highest packing density minimizing the defects. The mechanism of self-assembly follows the first–order Langmuir adsorption kinetics except for the fact that in self–assembly the thiolates interact with each other while growing.[32, 41, 42] The first regime becomes negligible as the concentration of thiolates in solution increases. A full coverage of alkanethiols on a gold surface is exhibited by a molecular arrangement of $\left(\sqrt{3}x\sqrt{3}\right)R30°$ relative to the gold atom underlayer. The packing arrangement is depicted by a thiol–thiol distance of 5 Å and the area pro-molecule is 21.6 $Å^2$ with a tilt angle of ~ 32° (see Figure 1.6).

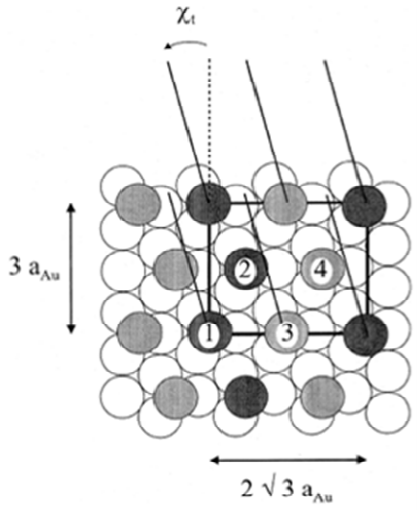


**Figure 1.6** 2D schematic arrangement of monolayer of dodecanthiol on Au(111) with $\chi_t$ is the tilt angle of alkanechain relative to the 2D plane.[26]

## 1.3 Printing of Inorganic Conductive Nanomaterials

Applications of inkjet printing technique in delivering inorganic conductive nanomaterials have achieved special attention, especially in the field optoelectronics (i.e. electrical circuitry and displays). Limited materials sources (e.g. rare earth substances), demand on production efficiency (i.e. simple and economics), and environmental concerns are some of motivations to use inkjet printing technique as an alternative to other techniques that are industrially used today (e.g. vacuum deposition, photoengraeving, and lithography).

Among various nanomaterials, silver nanoparticles have been widely explored due to their high conductivity and commercial availability combined with inexpensive prices.[43-46] The silver nanoparticles are normally dissolved in dispersants (stabilizers) resulting in a homogenous colloidal solution. Printings of colloidal solutions in the form of line circuitries with conductivities higher than 5 MS $m^{-1}$ have been reported.[46, 47] Printing or inkjet printing of silver conductive tracks on flexible substrates have potential applications, such as radio frequency identification (RFID) tags.[48, 49] Alternatively, various other conductive nanoparticles are inkjetted to form conductive lines with thicknesses in the range of ten micrometers to several millimeters, such as gold[50, 51], palladium[52], nickel[53] etc.

Small mass deliveries in each printing cycle have made it possible to control the deposited mass on the substrate and, therefore, to adjust the transparency of the substrate after nanoparticle depositions. When this function is combined with the flexibility of the inkjet printing technique in preparing complex structures, the realization of cheap plastic electronics is feasible.

Bühler et al.[54] deposited ITO nanocrystals on a transparent plastic substrate at ambient condition by inkjet printing. The resulting electrical properties of the coated film exhibited a sheet resistivity of 7 x $10^{-2}$ Ω $cm^{-2}$ at a layer thickness of 500 nm. In addition, a library of oxide nanoparticles was prepared by printing two different nanoparticle solutions with various compositions which provides a straightforward way to combinatorial chemistry.[55, 56]

In chapter 5, the function of inkjet printing as a tool of small mass delivery of cerium dioxide ($CeO_2$) precursor solution onto Antimony tin oxide (ATO) mesoporous film is studied. Multiple printing cycles were introduced and the delivered mass was analyzed by Quartz Crystal Microbalance (QCM).

## 1.4 Objectives of the Thesis

Despite the versatilities of inkjet printing technique described in the previous sections, there are still only a few systematic reports utilizing the abilities of the inkjet printing, as a delivery tool for self–assembled monolayers and inorganic nanoparticle systems. Self–assembled monolayers are commonly used as models in interface studies while nanoparticles have got many interests in nanotechnology. Thus, it is of interest to systematically investigate the benefit of inkjet printing technique in these systems which may provide positive additions in the preparation or production processes.

Having the objectives, at the primary stage, systematic studies were conducted with various thiolates of different chain lengths to address the following questions:

(i) Are conditions related to inkjet printing compatible with SAM formation?

(ii) What is the behavior of evaporating droplets and what is the effect on the resulting monolayers?

(iii) Can inkjet printing be used as a direct writing tool to prepare microelectrodes (e.g. disks and bands)? Herein the morphology of the resulting structures is investigated and more importantly, the ability of the inkjet printer to shoot two different thiols on one surface plane has to be addressed.

Benefitting from the existence of multiple reservoirs on the print head, with the monolayer systems, mixing of two thiols at the same time would be of interest in preparing tailored mixed SAMs and SAMs with chemical gradients. Therefore, the following questions must be addressed:

(i) How is the steepness of the resulting gradient?

(ii) How is the mixing behavior of the thiolates?

(iii) How is the morphology of the tailored mixture or chemical gradient?

Unlike in the thiolates, whereby the surface reactions are encountered, the ability of inkjet printing in delivering step–wise small mass of nanoparticle of $CeO_2$ are also examined. Therefore, the following subjects are also addressed:

(i) The sensitivity of a Quartz Microbalance to detect inkjetted nanopaticles;

(ii) Examination on mass delivered depending on the printing cycle;

(iii) The porous sensitivity of the solvent flow in between the nanonetworks.

## 1.5 References


(1) Guo, T. F.; Chang, S. C.; Pyo, S.; Yang, Y. *Langmuir* **2002**, *18*, 8142-8147.

(2) Hebner, T. R.; Wu, C. C.; Marcy, D.; Lu, M. H.; Sturm, J. C. *Applied Physics Letters* **1998**, *72*, 519-521.

(3) Moller, M. T.; Asaftei, S.; Corr, D.; Ryan, M.; Walder, L. *Advanced Materials* **2004**, *16*, 1558-1562.

(4) de Gans, B. J.; Schubert, U. S. *Macromolecular Rapid Communications* **2003**, *24*, 659-666.

(5) Mohebi, M. M.; Evans, J. R. G. *Journal of Combinatorial Chemistry* **2002**, *4*, 267-274.

(6) Allain, L. R.; Askari, M.; Stokes, D. L.; Vo-Dinh, T. *Fresenius Journal of Analytical Chemistry* **2001**, *371*, 146-150.

(7) Mironov, V.; Boland, T.; Trusk, T.; Forgacs, G.; Markwald, R. R. *Trends in Biotechnology* **2003**, *21*, 157-161.

(8) Pardo, L.; Wilson, W. C.; Boland, T. J. *Langmuir* **2003**, *19*, 1462-1466.

(9) Rayleigh, L. *Proceedings of the London Mathematical Society* **1878**, *10*, 4-13.

(10) Lohse, D.; van der Meer, D. *Nature* **2009**, *459*, 1064-1065.

(11) Chaudhary, K. C.; Redekopp, L. G. *Journal of Fluid Mechanics* **1980**, *96*, 257-274.

(12) Pimbley, W. T. *IBM Journal of Research and Development* **1976**, *20*, 148-156.

(13) Bogy, D. B.; Talke, F. E. *IBM Journal of Research and Development* **1984**, *28*, 314-321.

(14) Shield, T. W.; Bogy, D. B.; Talke, F. E. *IBM Journal of Research and Development* **1987**, *31*, 96-110.

(15) Tekin, E.; Smith, P. J.; Schubert, U. S. *Soft Matter* **2008**, *4*, 703-713.

(16) de Gans, B. J.; Duineveld, P. C.; Schubert, U. S. *Advanced Materials* **2004**, *16*, 203-213.

(17) Tirtaatmadja, V.; McKinley, G. H.; Cooper-White, J. J. *Physics of Fluids* **2006**, *18*, 043101-043118.

(18) Lin, S. P.; Reitz, R. D. *Annual Review of Fluid Mechanics* **1998**, *30*, 85-105.

(19) Rembe, C.; Patzer, J.; Hofer, E. P.; Krehl, P. *Proc. SPIE*; San Jose, CA, USA, 1996; pp 400-404.

(20) Notz, P. K.; Basaran, O. A. *Journal of Fluid Mechanics* **2004**, *512*, 223-256.

(21) Xu, Q.; Basaran, O. A. *Physics of Fluids* **2007**, *19*, 102111-102113.

(22) Dong, H. M.; Carr, W. W.; Morris, J. F. *Review of Scientific Instruments* **2006**, *77*, 085101-085108.

(23) Sowerby, S. J.; Heckl, W. M. *Origins of Life and Evolution of the Biosphere* **1998**, *28*, 283-310.

(24) Whitesides, G. M.; Grzybowski, B. *Science* **2002**, *295*, 2418-2421.

(25) Shevchenko, E. V.; Talapin, D. V.; Murray, C. B.; O'Brien, S. *Journal of the American Chemical Society* **2006**, *128*, 3620-3637.

(26) Schwartz, D. K. *Annual Review of Physical Chemistry* **2001**, *52*, 107-137.

(27) Poirier, G. E. *Chemical Reviews* **1997**, *97*, 1117-1127.

(28) Love, J. C.; Estroff, L. A.; Kriebel, J. K.; Nuzzo, R. G.; Whitesides, G. M. *Chemical Reviews* **2005**, *105*, 1103-1169.

(29) Schreiber, F. *Progress in Surface Science* **2000**, *65*, 151-256.

(30) Widrig, C. A.; Chung, C.; Porter, M. D. *Journal of Electroanalytical Chemistry* **1991**, *310*, 335-359.

(31) Schessler, H. M.; Karpovich, D. S.; Blanchard, G. J. *Journal of the American Chemical Society* **1996**, *118*, 9645-9651.

(32) Karpovich, D. S.; Blanchard, G. J. *Langmuir* **1994**, *10*, 3315-3322.

(33) McCarley, R. L.; Dunaway, D. J.; Willicut, R. J. *Langmuir* **1993**, *9*, 2775-2777.

(34) Yang, G. H.; Liu, G. Y. *Journal of Physical Chemistry B* **2003**, *107*, 8746-8759.

(35) Poirier, G. E.; Tarlov, M. J. *Journal of Physical Chemistry* **1995**, *99*, 10966-10970.

(36) Bain, C. D.; Troughton, E. B.; Tao, Y. T.; Evall, J.; Whitesides, G. M.; Nuzzo, R. G. *Journal of the American Chemical Society* **1989**, *111*, 321-335.

(37) Dannenberger, O.; Buck, M.; Grunze, M. *Journal of Physical Chemistry B* **1999**, *103*, 2202-2213.

(38) Vericat, C.; Vela, M. E.; Benitez, G. A.; Gago, J. A. M.; Torrelles, X.; Salvarezza, R. C. *Journal of Physics-Condensed Matter* **2006**, *18*, R867-R900.

(39) Yourdshahyan, Y.; Rappe, A. M. *Journal of Chemical Physics* **2002**, *117*, 825-833.

(40) Poirier, G. E.; Pylant, E. D. *Science* **1996**, *272*, 1145-1148.

(41) Buck, M.; Grunze, M.; Eisert, F.; Fischer, J.; Trager, F. *Journal of Vacuum Science and Technology A* **1992**, *10*, 926-929.

(42) Thomas, R. C.; Sun, L.; Crooks, R. M.; Ricco, A. J. *Langmuir* **1991**, *7*, 620-622.

(43) Magdassi, S.; Ben Moshe, M. *Langmuir* **2003**, *19*, 939-942.

(44) Lee, H. H.; Chou, K. S.; Huang, K. C. *Nanotechnology* **2005**, *16*, 2436-2441.

(45) Perelaer, J.; de Laat, A. W. M.; Hendriks, C. E.; Schubert, U. S. *Journal of Materials Chemistry* **2008**, *18*, 3209-3215.

(46) Nguyen, B. T.; Gautrot, J. E.; Nguyen, M. T.; Zhu, X. X. *Journal of Materials Chemistry* **2007**, *17*, 1725-1730.

(47) Fuller, S. B.; Wilhelm, E. J.; Jacobson, J. M. *Journal of Microelectromechanical Systems* **2002**, *11*, 54-60.

(48) Perelaer, J.; de Gans, B. J.; Schubert, U. S. *Advanced Materials* **2006**, *18*, 2101-2104.

(49) Reinhold, I.; Hendriks, C. E.; Eckardt, R.; Kranenburg, J. M.; Perelaer, J.; Baumann, R. R.; Schubert, U. S. *Journal of Materials Chemistry* **2009**, *19*, 3384-3388.

(50) Wang, J. Y.; Huo, S. J.; Cai, W. B.; Xu, Q. J. *Chemistry Letters* **2006**, *35*, 582-583.

(51) Chow, E.; Herrmann, J.; Barton, C. S.; Raguse, B.; Wieczorek, L. *Analytica Chimica Acta* **2009**, *632*, 135-142.

(52) Zabetakis, D.; Loschialpo, P.; Smith, D.; Dinderman, M. A.; Dressick, W. J. *Langmuir* **2009**, *25*, 1785-1789.

(53) Ishida, Y.; Nakagawa, G.; Asano, T. *Japanese Journal of Applied Physics Part 1* **2007**, *46*, 6437-6443.

(54) Buhler, G.; Tholmann, D.; Feldmann, C. *Advanced Materials* **2007**, *19*, 2224-2227.

(55) Zhang, Y.; Chen, L.; Yang, S.; Evans, J. R. G. *Journal of the European Ceramic Society* **2007**, *27*, 2229-2235.

(56) Chen, L.; Zhang, Y.; Yang, S.; Evans, J. R. G. *Review of Scientific Instruments* **2007**, *78*, 072210-072216.

# Chapter 2: Experiments

## 2. 1 Chemicals, Reagents, and Substrates

*Adsorbent materials*: Mercaptopropionic acid (HS-$(CH_2)_2$-COOH,Fluka), 11-amino-1-undecanethiol (AUT, HS-$(CH_2)_{11}$-$NH_2$, Dojindo), 11-mercaptoundecanoic acid (HS-$(CH_2)_{10}$-COOH, Aldrich), hexadecanethiol (HS-$(CH_2)_{15}$-$CH_3$, Fluka), and 3-(mercaptopropyl) trimethoxysilane ($(CH_3)_3O_3Si(CH_2)_3SH$, Aldrich) were used as received. Cer(III)nitrat hexahydrate ($CeNO_3O_9.6H_2O$) was obtained from Fluka. The Antimony tin oxide (ATO) paste was a gift from NTera.

*Solvents:* Absolute ethanol (in–house purified), isopropanol (Fluka, puris), tetraethylene glycol dimethylether (Fluka, puris), and glycerol ($C_3H_8O_3$, Riedel de Haen) were used without further purification. n–hexane (Riedel de Haen) and toluene (Fluka) were distilled from sodium hydride before use while chloroform (Merck), 1,2-dibromomethane (Fluka), and dichloromethane (Merck) were distilled from phosphorus pentoxide.

*Electrolyte and redox active species*: Potassium hexacyanoferrate (III) ($K_3[Fe(CN)_6]$, Fluka), 1-(ferrocenyl)ethanol ($C_{12}H_{14}FeO$, Fluka), and potassium chloride (KCl, Merck) were analytical grade and used as received.

*Substrates:* The gold plates used were home–made, purchased from Ssens (Hengelo, NL), and provided by Prof. Gunther Wittstock. The 6 MHz AT–cut quartz

crystals were purchased from Institute of Physical Chemistry Polish Academy of Science (Warsaw, PL).

a b

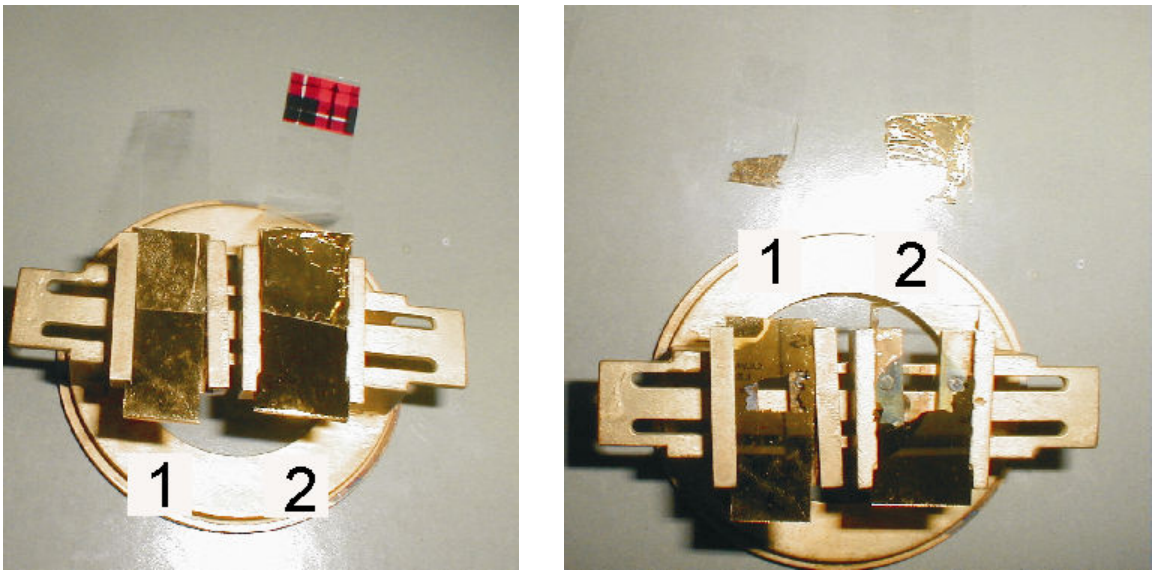


**Figure 2.1** Adhesive property of gold on mercaptopropionic silane modified glass (1) and unmodified glass (2). Before (a) and after (b) pilling test.

## 2. 2 Preparation of Transparent Gold Plates

A glass was cut into smaller plates (1.5 cm x 0.7 cm) before they are cleaned in ultrasound bath for 15 min. Afterwards, the small glass plates were dried under stream of Ar and put aside.

10 mL mercaptopropyl silane was diluted into 500 mL of a mix solvent of isopropanol and water (9:1 (v/v)). The mix solvent was heated and brought into reflux. The cleaned glass plates were immersed into the solvent under reflux for 10

min. The glasses were then rinsed with copius amount of isopropanol and dried under argon. The silane on glass curing was carried out by heating the glass in an oven for 10 min at 105 °C. The process was repeated for at least three times.

The silane modified glass was put into a chamber of Chemical Vapor Deposition (CVD) equipment. The vacuum pressure was adjusted. The rate of the gold deposition was regulated to achieve ca. 140 nm gold thickness. At this thickness, the gold remains optically transparent. The adhesion of gold–to–glass was characterized by so–called pilling test using transparent adhesive film (Figure 2.1). The result shows a good adhesion of the gold to the glass. The unmodified glass shows a poor adhesion property.

a b

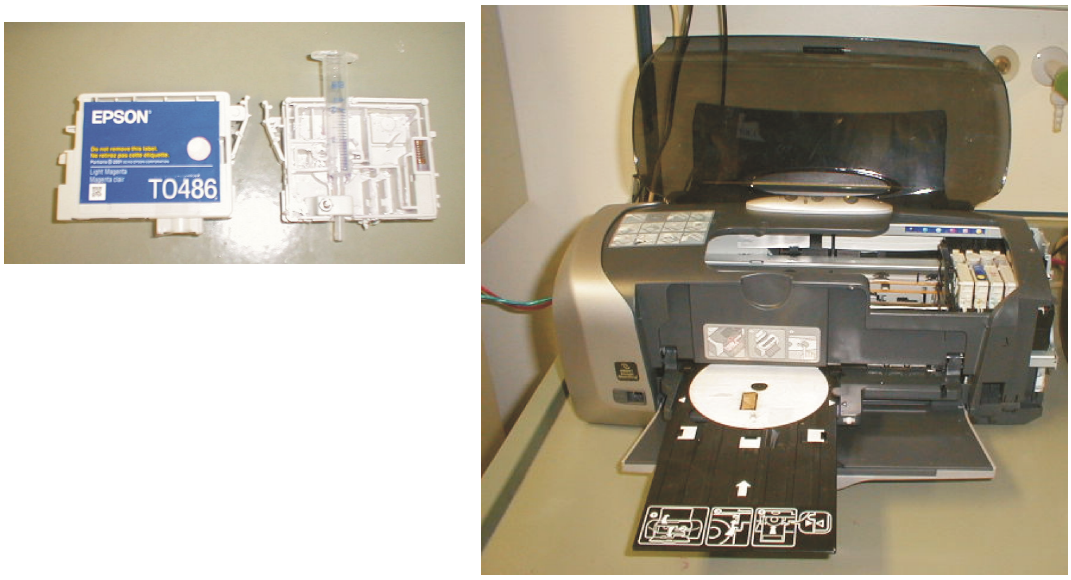


**Figure 2.2** Syringe of 2 mL replaces the original ink reservoir (a). Construction for the chemical printing job (b).

## 2. 3 Mechanical Inkjet Printer Modifications

The print head cover was dismantled to have access to the cartridges at the print head. The original cartridges were emptied from the original ink and washed with copious amount of water to clean the inner part. Plastic syringes (2 ml) were used as replacements of the original ink reservoirs. Each cartridge was mechanically bored to fit the syringe and the bottom part was screwed (Figure 2.2(a)). The gold plates and the ATO modified quartz crystals were placed on a caddy designed for printing graphics on a compact disk allowing perpendicular mounting to the print head. Two feed rolls were also dismantled, so that the substrate can move smoothly through the printer. The construction is shown in Figure 2.2(b).

## 2.4 Cleaning of the Substrates

(a) The Gold plates

The sputtered gold (200 nm) on glass plates (1.1mm thick) purchased from Ssens (Hengelo, NL) were first cut into 1 cm x 2.5 cm electrodes. Prior to use, the electrodes were exposed to air plasma (PDC - 32G, Harrick Scientific, Ithaca, NY) for 10 min. They were then immersed in absolute ethanol for about 10 min and dried under a stream of Ar. Used electrodes were cleaned prior to plasma treatment by exposing them to a Piranha solution, a mixture of $H_2O_2/H_2SO_4$ (1:3 v/v), at room temperature for about 3 min (**Caution**: *This mixture reacts violently*

*with all organic material. The solution has to be handled with extreme care to avoid personnel injury and property damage)*.

The fresh home–made transparent gold plates were cleaned by exposing into air plasma (PDC-32G, Harrick Scientific, Ithaca, NY) for 10 min, immersed in absolute ethanol for 10 min and dried under stream of Ar.

(b) The 6 MHz AT–Cut Quartz Crystals

The quartz crystals were also cleaned by immersing into the Piranha solution for 3 min and subsequently washed with distilled water and finally dried under a stream of Ar.

### 2. 5 Modifications of the Substrates

(a) Preparations of the Thiolate Monolayers

1. Immersion

The gold electrodes were immersed in a 1 mM ethanolic solution of the respective thiol for overnight at room temperature, washed with absolute ethanol, and dried under a stream of Ar.

2. Inkjet Printing (IJP)

The thiol inks were printed at 100% color density from the cartridges of the modified Epson stylus Photo R200, and each print was visually controlled for printhead clogging. (i) For printing nonstructured homogeneous SAMs, the yellow

cartridge channel with droplet density of 0.822 µL $cm^{-2}$ was used as the thiol reservoir. (ii) For printing structures using two thiols, the cyan (0.5474 µL $cm^{-2}$) and the magenta (0.6955 µL $cm^{-2}$) cartridges were used as thiol reservoirs. (iii) For printing structures using one thiol in the printing step, followed by backfilling (immersion). For printing the band electrodes, the yellow cartridge with 100 % color intensity (0.822 µL $cm^{-2}$) was applied whereas for printing disk microelectrodes the yellow cartridge with 1, 4, and 10% color intensity were applied ($V_Y$ < 0.012 µL $cm^{-2}$). (iv) For printing printing mixture of thiols, the cyan and magenta channels were employed. The thiolate mixture prepared by the pixel–based, 100 % color intensity from both channels were used whereas those prepared by droplet–based, the color intensities were varied according to the desired composition (see section 2.7). The mixture phenomena will be described in chapter 4. After modifications, the electrode was washed with absolute ethanol and dried under a stream of Ar.

3. Backfilling

The backfilling refers to a step in which the modified substrate is immersed in a second thiol solution. For backfilling, 1 mM of hexadecanthiol in absolute ethanol was used and the immersion was carried out for at least 1h. After backfilling the electrode was washed with absolute ethanol and dried under a stream of Ar.

(b) Preparation of Antimony Tin Oxide Mesoporous Films

The ATO paste was stirred overnight to maintain the homogenous dispersity of the particles. A small portion of the ATO paste was spread on a 6 MHz quartz crystal by the doctor blade technique to yield about 1 – 5 µm thick films. Afterwards, the ATO coated quartz was fired at 450 °C for 15 min and cooled down.

## 2. 6 Electrochemical, Spectroscopic, Quartz Microbalance and Optical Methods

(a) Cyclic Voltammetry (CV)

The measurements were performed in a three-electrode system using a PGSTAT 20 from AUTOLAB controlled by GPES (software version 4.9, ECO Chemie 1995). The modified gold electrode was used as a working electrode (active area 0.5 – 1 $cm^2$), the reference was an Ag|AgCl (Metrohm, 6.0724.140, separated by a salt bridge), and the auxiliary electrode was a Pt wire. Unless otherwise stated, the scan rate was 100 mV $s^{-1}$.

(b) Electrochemical Impedance Spectroscopy (EIS)

The EIS measurements were performed with the same potentiostat and setup as described for cyclic voltammetry. A single sine wave excitation with 10 mV amplitude at the dc potential of the redox couple (0.2 V vs Ag|AgCl) was applied.

The spectra were recorded from 100 or 10 kHz down to 10 mHz. The impedance data were analyzed by the fit programs incorporated in the FRA package using the equivalent circuits *R*s(*C*[*R*ct *Z*w]) and *R*s(*Q*[*R*ct *Z*w]).

(c) Quartz Microbalance

The modified quartz substrates of 6 MHz were put into sample holder and screwed from the back to fit the position and to avoid any leakage of fluids applied. The oscillation frequencies of the ATO coated quartz after each printing – firing cycle application were recorded. The measurements were conducted under Ar flow and under liquid of five different solvents which are n-hexane, toluene, dichloromethane, chroloform, and 1,2-dibromomethane.

(d) Optical Microscopy

A Biolux 654 optical microscope was used for the optical analysis of the ink printed on paper. An additional Peltier element was fitted to the top of the substrate holder, to study thiol structures on gold optically by specific water vapor condensation according to the hydrophilicity/hydrophobicity of the thiols present. The surface was illuminated from the side by a focused LED lamp for maximum optical contrast.

## 2. 7 Graphical Software for the Printing Jobs

(a) Printing Protocols for Thiolates Monolayers

Corel Draw X3 running on a PC was used to layout the SAM structure and to launch the printing job. All structures were drawn using the *rectangle tool* with the outline function (*stroke*) set to zero. In order to fill a structure with a single thiol, the structure was filled with pure color at 100% color density, that is, cyan, magenta, or yellow, with the color ink replaced by the corresponding thiol solutions in the cartridge. Because there are three channels (i.e. yellow, magenta and cyan) used at the printhead, the ejected amount varies slightly. Therefore, for 1 mM thiol solution and 100 % color intensity, the monolayer coverages are 0.822 x $10^{-9}$ mol $cm^{-2}$, 0.552 x $10^{-9}$ mol $cm^{-2}$ and 0.744 x $10^{-9}$ mol $cm^{-2}$ for yellow, magenta and cyan, respectively. The values are still in the range of the surface confinement of monolayers on gold. In order to get well-separated disks of thiols on gold with an average distance of ~250 $\mu$m, low color densities are used. The monolayer coverages are estimated by assuming that the printed droplets homogenously cover the surface. More detail about the surface coverages of the printed thiols upon color intensities will be emphasized in section 2.7.

(b) The Printing Protocol for the Cerium Precursor Solution

0.2 M $Ce(NO_3)_3.6H_2O$ in tetraethylene glycol dimethyl ether (Fluka, p.a) was prepared as the precursor ink solution which was used to apply homogeneous layers on the ATO coated quartz substrates with a thickness in the range of 2.5 to

5 µm. After printing, the substrate was heated at 120 °C to evaporate the precursor solvent. Afterwards, the sample was fired at 450 °C for 15 min. This printing–firing cycle was applied repeatedly and the mass deposited was analyzed by the Quartz Microbalance (QCM) method.

## 2. 8 The Calibration of The Jet Delivery

The main purpose on the jet delivery calibration is to obtain the volume densities and the corresponding surface coverages of inkjetted materials under a given set of parameters. As a reference, the calibration of each cartridge was done on the original inks of the printer. Color intensities between 0 to 100 were adjusted in Corel Draw and printed on transparent films. The colored transparent films were investigated by UV – vis spectroscopy, i.e. all spectra were recorded and each color intensity was repeated three times.

The surface concentrations of the inkjetted materials on a surface depending on the color intensity was calculated by taking the ratio of absorbance intensity of a known ink concentration in solution and the inkjetted materials on the transparent film. According to the Beer–Lambert law (equation 2.1), the absorbance is linearly proportional to the concentration of the absorbing species, c.

$$A = \varepsilon c l \qquad (2.1)$$

ϵ is molar absorptivity constant and L is the length path.

The absorbance ratios read on the reference solution and on the transparent films are used as correction factors for calculating the concentration of the ink

deposited on the transparent films depending on the color intensity introduced. The volume densities (µL $cm^{-2}$) for different color intensities ejected on a surface are then calculated by assuming that homogenous printings are encountered and ink concentrated on 1 ml solution is the same as those deposited on 1 $cm^2$ surface. Even though such assumptions deviate in the printings using low color intensities (i.e. 1 < 30 % color intensity), they suffice the printings at the higher color intensities where overlapping between droplets occurs. It is calculated that for 1 mM thiolate concentration, the volume densities are in the same magnitude to the surface concentration (mol $cm^{-2}$).

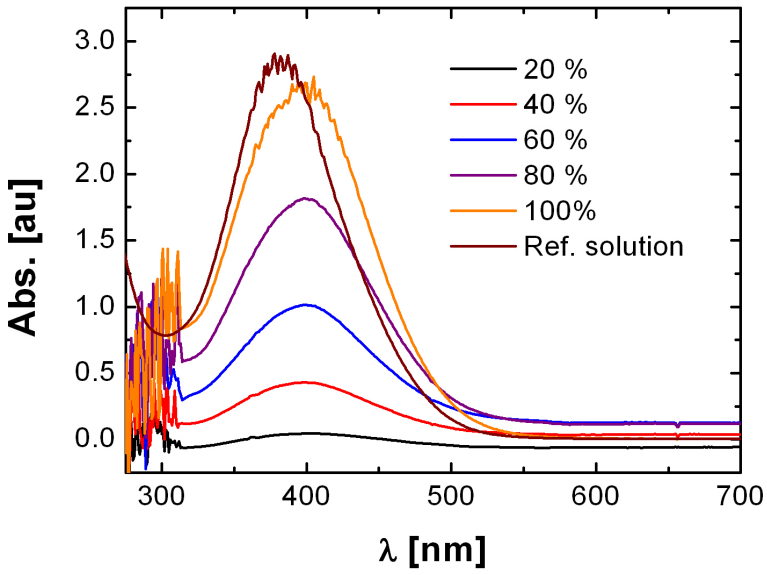


**Figure 2.3** Spectra of ink inkjetted from Yellow cartridge and corresponding reference solution.

It is worthy to note that in the calibration using the original inks, all ejected materials are absorbed on the surface (i.e. the transparent films). In the printing thiolates ink, the excess, unbounded thiolates will be washed away during the washing step. The study of the surface coverage of inkjetted thiolate will be emphasized in chapter 3.

(a) Yellow Cartridge

As a reference, the original yellow ink solution ($Y_{sol}$) of 15 µL was diluted into 25 mL by distilled water. The current ink concentration in 1 mL of the solution is 0.6 µL. The absorbances at 430nm read from the reference solution ($Y_{sol}$) and from the transparent plane film with intensity of 100 % ($Y_{100}$) are 1.50 and 2.05, respectively (Figure 2.3). Thus, the absorbance ratio between $Y_{sol}$ and $Y_{100}$ gives 1.36. Thus, the volume density of the inkjetted ink on transparent film with 100 % color intensity is 0.816 µL $cm^{-2}$.

**Table 2.1** Dependence of the inkjetted volumes from yellow reservoir upon adjusted color intensities

| Color Intensity [%] | $A_{430}$ [nm] | $V_Y$ [µL $cm^{-2}$] | $\Gamma_Y$ x $10^{-9}$ [mol $cm^{-2}$] |
|---|---|---|---|
| 100 | 2.048 | 0.822 | 0.822 |
| 80 | 1.333 | 0.535 | 0.535 |
| 60 | 0.705 | 0.283 | 0.283 |
| 40 | 0.312 | 0.125 | 0.125 |
| 20 | 0.029 | 0.012 | 0.012 |

Following the equation 2.1, the selected spectra, the corresponding volume densities and the surface concentration for 1 mM thiolate concentration are exhibited in Figure 2.3 and Table 2.1.

(b) Cyan Cartridges

Similar to the calibration on the yellow cartridge, an ink with concentration of 0.4 µL in 1 mL solution is used as a reference solution. The absorbance of the ink in the solution was compared with the cyan inkjetted on the transparent films and the corresponding volume density and the surface coverage for 1 mM thiolate concentration are presented in Figure 2.4 and Table 2.2.

a b

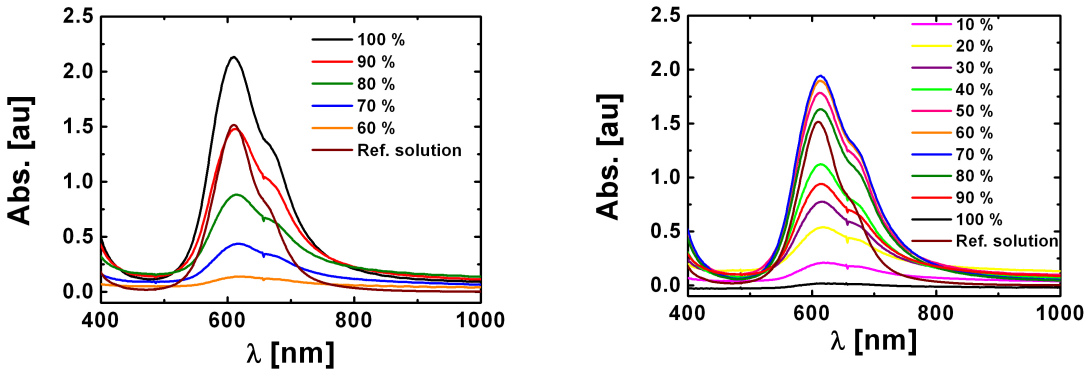


**Figure 2.4** Spectra of ink inkjetted from Cyan reservoirs and the corresponding reference solution.

Cyan channels consist of two ink reservoirs that are light Cyan and (dark) Cyan. Ejected cyan color at certain intensities might come out from a mixture of both reservoirs. Unfortunately, there is no function available to operate the reservoirs separately. The amount ejected from each reservoir can be discovered by putting an empty cartridge in light cyan during calibration of (dark) cyan cartridge, and vice versa. A small increment of color intensity was also introduced to obtain the transition from (dark) cyan to light cyan which is at 54% color intensity. The complete spectra are available in the appendix. Interestingly, the (dark) cyan only eject materials (e.g. inks) at higher color intensity, whereas the light cyan eject materials at all color intensities with the maximum point at around 70% color intensity.

**Table 2.2** Dependence of inkjetted volumes from cyan reservoirs upon adjusted color intensities

| Color Intensity [%] | Cyan | | | Light Cyan | | |
|---|---|---|---|---|---|---|
| | $A_{610}$ [nm] | Vs [μL $cm^{-2}$] | $\Gamma_C$ [mol $cm^{-2}$] | $A_{610}$ [nm] | Vs [μL $cm^{-2}$] | $\Gamma'_C$ [mol $cm^{-2}$] |
| 10 | - | - | - | 0.1546 | 0.0420 | 0.0420 |
| 20 | - | - | - | 0.3802 | 0.1033 | 0.1033 |
| 30 | - | - | - | 0.6515 | 0.1770 | 0.1770 |
| 40 | - | - | - | 1.0158 | 0.2959 | 0.2959 |
| 50 | - | - | - | 1.6561 | 0.4498 | 0.4498 |
| 60 | 0.0906 | 0.0246 | 0.0246 | 1.8137 | 0.4926 | 0.4926 |
| 70 | 0.3453 | 0.0938 | 0.0938 | 1.8538 | 0.5035 | 0.5035 |
| 80 | 0.7141 | 0.1939 | 0.1939 | 1.5528 | 0.4217 | 0.4217 |
| 90 | 1.3295 | 0.3611 | 0.3611 | 0.8207 | 0.2229 | 0.2229 |
| 100 | 2.0154 | 0.5474 | 0.5474 | 0.0169 | 0.0046 | 0.0046 |

(c) Magenta Cartridges

The magenta channels also consist of two reservoirs that are light magenta and (dark) magenta. Hence, the same calibration principle as conducted in the Cyan channels was applied to the magenta channels whereby the concentration of the ink is 0.8 µL in 1 mL solution. Figure 2.5 and Table 2.3 depict the selected spectra and the corresponding printed volume densities, respectively.

a b

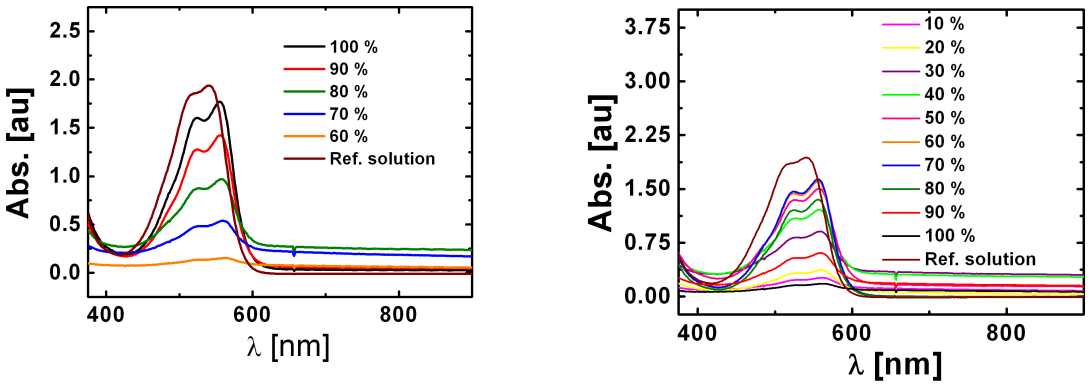


**Figure 2.5** Spectra of ink inkjetted from the Magenta reservoirs and the corresponding reference solution.

## 2. 9 Thiol Ink

Unless otherwise stated, a mixture of ethanol/glycerol of 6:1 (v/v) containing the thiol at 1 mM concentration was used. The ink viscosity under this condition was 2.5 cPa s, as measured by using an Ubbelohde viscosimeter. The capillary type 1c with a diameter of 0.78 mm was used. The viscosity measurements were

conducted at 25°C which was controlled by waterbath and the average from three measurements was taken.

**Table 2.3** Dependence of the inkjetted volumes from magenta reservoirs upon adjusted color intensities

| Color Intensity [%] | Magenta | | | Light magenta | | |
|---|---|---|---|---|---|---|
| | $A_{520}$ [nm] | Vs [µL $cm^{-2}$] | $\Gamma_M$ x $10^{-9}$ [mol $cm^{-2}$] | $A_{520}$ [nm] | Vs [µL $cm^{-2}$] | $\Gamma'_M$ x $10^{-9}$ [mol $cm^{-2}$] |
| 10 | - | - | - | 0.0649 | 0.0649 | 0.0649 |
| 20 | - | - | - | 0.1275 | 0.1275 | 0.1275 |
| 30 | - | - | - | 0.2280 | 0.2280 | 0.2280 |
| 40 | - | - | - | 0.3591 | 0.3591 | 0.3591 |
| 50 | - | - | - | 0.5323 | 0.5323 | 0.5323 |
| 60 | 0.0751 | 0.0082 | 0.0082 | 0.6328 | 0.6328 | 0.6328 |
| 70 | 0.3036 | 0.0490 | 0.0490 | 1.4259 | 0.6448 | 0.6448 |
| 80 | 0.6260 | 0.2318 | 0.2318 | 1.1861 | 0.5364 | 0.5364 |
| 90 | 1.2217 | 0.5408 | 0.5408 | 0.1687 | 0.1687 | 0.1687 |
| 100 | 1.5568 | 0.6955 | 0.6955 | 0.0877 | 0.0397 | 0.0397 |

# Chapter 3: Quality of Inkjetted Monolayers within Plane Gold Areas and on Evaporating Droplets

(This work is a part of a collaboration with University of Oldenburg and shared results are presented)

The electrochemical insulating quality of self–assembled monolayers immobilized homogenously by three different techniques (i.e. self assembling from solution, stamping, and inkjet printing) was analyzed by cyclic voltammetry and electrochemical impedance spectroscopy. The results suggest that the electrochemical insulating property which is related to the molecular structure of the monolayer prepared by inkjet printing is similar to that prepared by self–assembly from solution (i.e. under equilibrium condition). In addition, the morphology of the inkjetted thiolate inks in the form of isolated droplets is also investigated. The ink composition and the thiolate concentration have an influence on droplet structure on the electrode surface.

## 3.1 Electrochemical Insulating and Non–insulating Properties of Monolayers.

In chapter 1, the criteria for a closed packed monolayer are described. The preparation of monolayers by immersing a gold surface into a solution containing the thiolates is well known for the preparation of homogenous monolayers. However, it does not allow for the lateral structuring of monolayer which are of interest in many applications, such as (bio)sensors and electrical circuitry. Ink jet printing and stamping are mainly used for lateral structuring.

However, it is of course possible to generate “homogenously” printed areas, too, with the techniques. To check the quality of the corresponding homogenous monolayer, the homogenous printed SAM printed on gold electrodes with area of 1 $cm^2$ is investigated.

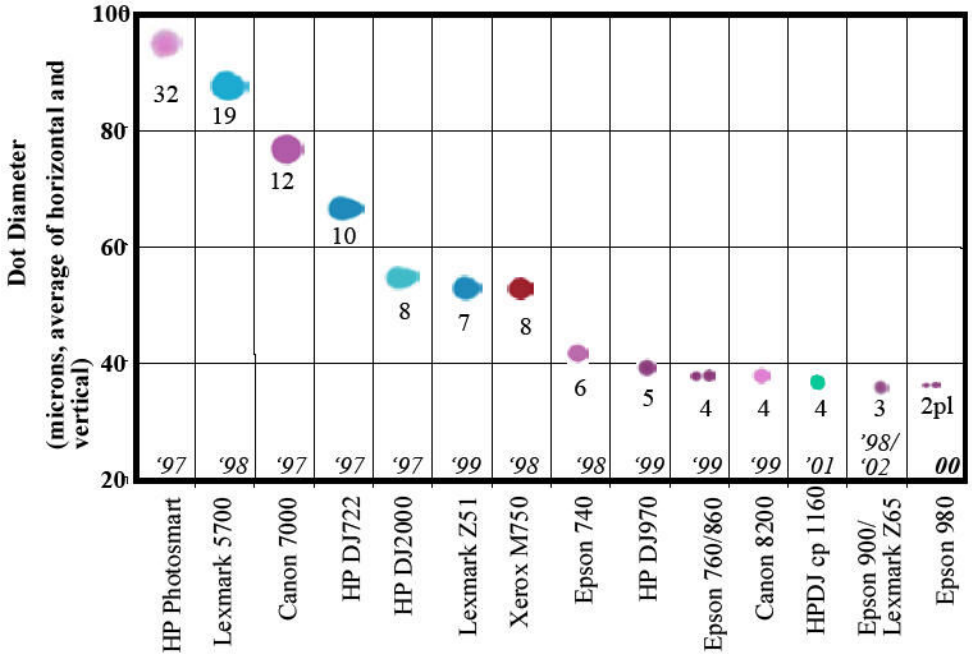


**Figure 3.1** Droplet ejected from different commercial printers as a function of the production year.

In inkjet printing, the deposition of a fired substance, i.e. thiolates, is comparable to printing ink on a paper. Using original EPSON inks and the EPSON stylusphoto R200, droplets of 3 pL volume are fired from each nozzle on the printhead. Interestingly, each droplet is always accompanied by a satellite, which is well known for EPSON printing system (Figure 3.1).[1] The same behavior was also observed for the thiol ink, pairs of droplet–satellites were also produced in the form of double disks or ellipsoidal structure of ~ 40

µm x 80 µm, if the disks are coalescent, according to the SECM measurement. More detailed studies about the droplets are provided in chapter 4.

The printer calibration of the volume jetted per $cm^{-2}$, at 100 % color intensity and 1 mM thiol concentration, yields average surface concentration, Γ, of 1 x $10^{-9}$ mol $cm^{-2}$. The value is slightly higher than theoretically necessary, i.e. self–assembled monolayers on gold show Γ = 7.6 x $10^{-10}$ mol $cm^{-2}$.[2, 3] After printing, the substrate was washed with copius of ethanol to eliminate excess physical bounded thiolates and also to eliminate the co–solvent glycerol which is used for adjusting viscosity.

The micro–contact printing (µCP) technique has been widely used to prepare lateral structures of monolayers among other lithography techniques.[4-7] It is used to compare the quality of homogenous monolayers between the stamping and ink jet printing. Three aspects are of importance: (i) both techniques are considered as fast and straight printing methods, (ii) lateral structures can be prepared by both methods, and (iii) due to relatively short immobilization time for both techniques, the monolayers can equilibrate which may result in reduced quality of the corresponding monolayers. The same monolayer was also prepared by immersion (under equilibrium condition) which is expected to yield the most perfect monolayer. Hexadecanthiol is chosen as the system since its long alkane chains have proven to yield a good insulating property.[8, 9]

The quality of the prepared monolayers was first characterized by cyclic voltammetry. As a control, the response of an unmodified gold electrode was also measured. Figure 3.2(a) exhibits the voltammograms of $Fe(CN)_6^{-3}$

recorded of the monolayers produced by the three techniques. The voltammograms reveal that the gold surfaces are insulated by the hexadecanthiol as seen from the suppression of the faradaic currents in the range of two orders of magnitude.

a b

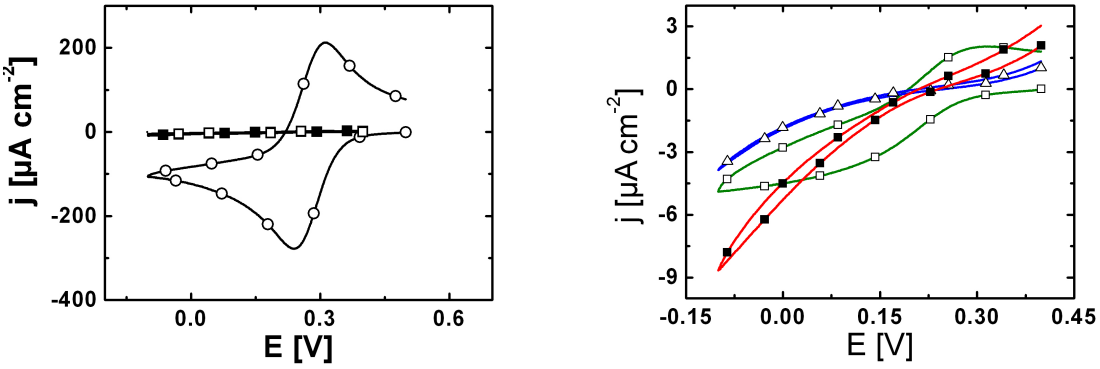


**Figure 3.2** Cyclic voltammograms of 1 mM $K_3[Fe(CN)_6]$ in 0.1 M KCl at a bare gold electrode (O) and at HS-$(CH_2)_{15}$-$CH_3$ modified electrodes prepared by IJP (■), *µ*CP (□), and immersion (Δ).(a) The insulating property of hexadecanthiolate monolayers on gold and (b) the zoomed voltammograms of hexadecanthiol in respect to the immobilization techniques used.

Figure 3.2(b) presents a closer look to examine in more detail the insulating behavior of the three electrodes. The voltammograms show that the monolayer prepared by immersion possesses the highest insulating property with current density less than 500 pA $cm^{-2}$. The current densitiy of the monolayer prepared by inkjet printing is in the range of 1 µA $cm^{-2}$ with no peak formation in the forward and backward scans. However, shallow and broad peaks which are centered around the $Fe(CN)_6^{-3}$ standard potential ($E^0$) are

observed in both scans for the monolayer prepared by μCP indicating a slow permeation of the electroactive species which probably travel through pinholes and/or non–ideal packing of the monolayer. Many reports[9-16] have described that the molecular structures of monolayers prepared by μCP comprise mixtures of different structures, liquids and crystalline domains. Commensurate molecular packing domains are found more in the middle of the relief area while liquid type arrangements are pronounced at the border of a structure. The diversities stem from the different mechanical contact, properties of the stamps used, the size of the relief structure, the time of contact, the thiolate concentration and the solvents used. Increasing the thiolate ink concentration to 100 mM has been reported to improve the molecular packing reaching to that prepared by immersion.[17]

## 3. 2 Electrochemical Impedance Measurements on Monolayers of Alkanethiolates

More detailed information about the structure of self–assembled monolayers can be obtained from electrochemical impedance spectroscopy (EIS). EIS allows characterizations of surfaces, layers or membranes by introducing a frequency range across the interfaces.[18-23] The EIS measurement is conducted by applying a sinusoidal ac potential to the monolayer modified gold at the working electrode. A sinusoidal current response then flows between the working and the counter electrode (Figure 3.3). The resulting vector between the applied voltage (E) and the current (I) over a broad frequency

range (ω) yields the impedance vector (Z) (see equation 3.1). The phase angle (ϕ) denotes the phase shift between vector E and vector I at a given frequency.

$$Z(\omega) = \frac{E(\omega)}{I(\omega)} \tag{3.1}$$

The EIS spectra can be performed as a Bode plot (log |Z| vs ϕ(ω)) or as a Nyquist plot (Z' vs Z") in which the impedance factor is separated into the real (Z') and imaginary (Z") parts according to the equation 3.2:

$$Z = Z' + jZ'' = Z_0 \cos\phi + jZ_0 \sin\phi \tag{3.2}$$

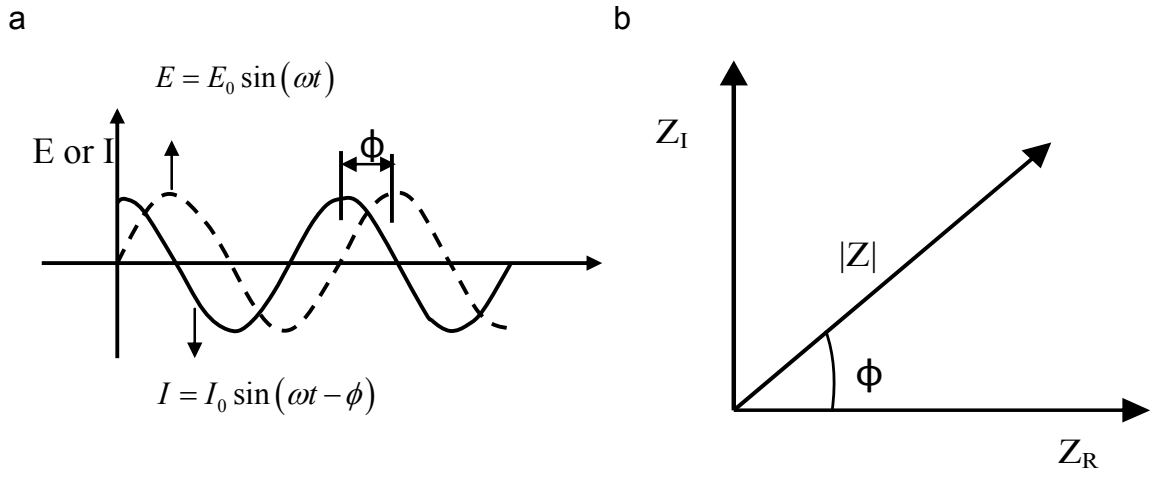


**Figure 3.3** Impedance spectroscopy. Sinusoidal waves (a) and Nyquist plot (b).

The resulting spectra are then analyzed according to an appropriate electrical equivalent circuit model system and the information is calculated by a nonlinear least square fitting procedure. Randles equivalent circuit is the most common circuit to describe monolayer systems (Figure 3.4(a)). In this circuit

four elements are identified: Resistance, capacitance, constant phase element, and Warburg impedance. The functions of the elements are described below.

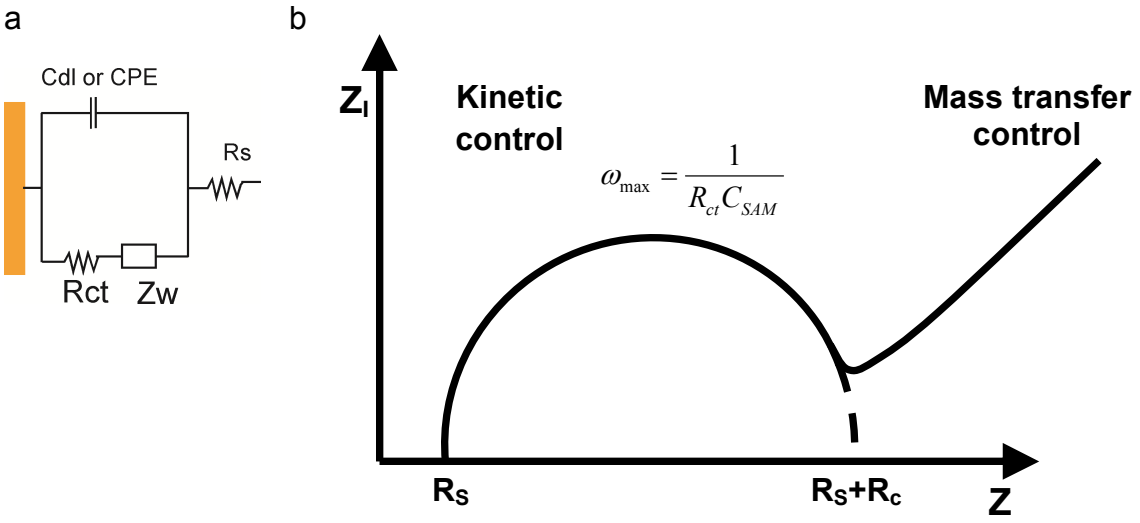


**Figure 3.4** Randles equivalent circuit displays electrical interface response (a). Faradaic nyquist plot with highlighted analysis of the electrical elements (b).

In the faradaic Nyquist impedance plot, there are two regions distinguished depending on the frequency range (Figure 3.4(b)). The first region is the part of the spectra resembling a semicircle (higher frequency range). In this frequency range, the electron transfer kinetic shows up. The magnitude of the monolayer capacitance ($C_{ML}$) and the charge transfer resistance ($R_{ct}$) can be read from the radius of the semicircle on the imaginary axis and on the real axis, respectively. In the lower frequency range, the semi infinite diffusion of ions and mass transfer of the redox species at the interface determine the spectra. They appear as a straight line with slope close to unity. The region is also termed as Warburg impedance (W) element.

So called non–ideal behavior, such as asymmetrical semi–circle, is often observed in the EIS measurements. The nonideality may arise from surface roughness[24-26]. In order to quantify the deviations, a constant phase element (CPE) is introduced and replaces the $C_{ML}$ with α as a correction factor[23, 26-28]. The CPE would be equal to $C_{ML}$ if α = 1 and it deviates from 1 according to the surface roughness.

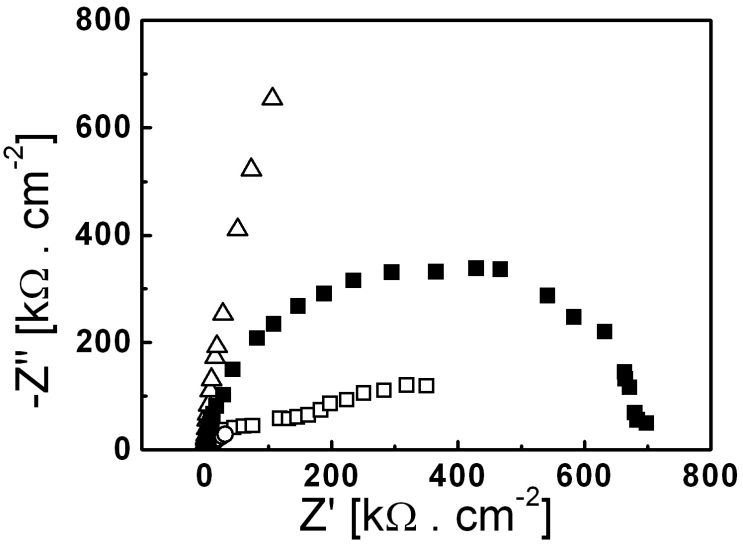


**Figure 3.5** Electrochemical impedance spectroscopy of unmodified (O) and HS $(CH2)_{15}$-$CH_3$ modified electrodes: IJP (■), *μ*CP (□) and immersion (Δ) in 1 mM $K_3[Fe(CN)_6]$/0.1 M KCl. *E*(dc) = 0.2 V vs Ag|AgCl.

The hexadecanthiol monolayers immobilized by the three techniques was characterized by EIS. The EIS spectrum of the bare electrode was also recorded. The resulting Nyquist plots of the probes are presented in Figure 3.5. The deposition techniques evidently affect the overall spectra, especially the diameter of the semi–circle. As mentioned earlier, the outcome spectra were

analyzed using Randles equivalent circuit with its circuit modification. The data are summarized in Table 3.1.

**Table 3.1** Results from Electrochemical Impedance Measurements

| | $R_s$ (C[$R_{ct}$ $Z_W$]) | | $R_s$(Q[$R_{ct}$Zw]) | | |
|---|---|---|---|---|---|
| | $R_{ct}$ [KΩ $cm^{-2}$) | C (μF $cm^{-2}$) | $R_{ct}$ (KΩ $cm^{-2}$) | $Y_o$ (Ω$cm^{-2}s^n$) | n |
| Bare Au[a)] | 0.281 | 16.2 | 0.339 | 8.2 x $10^{-6}$ | 0.87 |
| HDT μCP | 98.7 | 1.06 | 116.48 | 0.81x $10^{-6}$ | 0.95 |
| HDT IJP | 667 | 0.995 | 674 | 2.23 x$10^{-6}$ | 0.993 |
| HDT Immersion | 10800 | 0.52 | 11300 | 0.95x $10^{-6}$ | 0.987 |

(a) The data were obtained from extended frequency window (100 KHz to 10 mHz)

The insulating property of the hexadecanthiol is denoted by the diameter of the semi–circle following the sequence of immersion > IJP > μCP. The corresponding charge transfer resistances ($R_{ct}$) have been calculated. The $R_{ct}$ values of IJP– and immersion modified electrodes are comparable to those reported in literature for medium and short immersion time, both spectra show no Warburg lines, indicating good insulation[29, 30]. On the other hand, the $R_{ct}$ value of *μ*CP modified electrode is lower than those of IJP and immersion, and a Warburg line at lower frequencies is observed. The slope of the Warburg line is below 45° which indicates defects on the monolayer with large separation[30]. These facts again give an evidence of pinholes in the *μ*CP monolayer. In addition, the extracted capacitances magnitudes of the systems investigated are in the same range and inline with other reports.[8, 19,31]

Bearing in mind that the insulating properties of monolayer modified electrodes are seldom perfect, the estimation of the so–called fractional surface coverage (Θ) becomes an important aspect in quantifying the quality of immobilized monolayers. The EIS method has been proven to provide a more reliable value in estimating Θ as compared to cyclic voltammetry where the Θ values are calculated solely from peak currents ratios.[21] Sabatani et al. [32] proposed a model to estimate the Θ from the ratio of the charge transfer between bare electrode ($R_{ct}^{0}$) and monolayer modified electrode ($R_{ct}^{SAM}$), according to equation 3.3:

$$1-\theta = \frac{R_{ct}^{0}}{R_{ct}} \tag{3.3}$$

In this equation, it is assumed that the electron transfer on the defect sites undergoes a planar diffusion. However, Finklea et al.[33] and others[20, 32, 34], based on the work of Tokuda et al.[35] and Amatore et al. [36], pointed out that at higher surface coverage (e.g. 1 – Θ < 0.1) the defect sites are described as disk arrays embedded in an insulating plane. Therefore, a mass transfer associated with microarrays parameters should be taken into account. Based on this model, each defect site on the monolayer corresponds to the nearly isolated radial diffusion profiles at higher frequency range. The real impedance component is expressed as:

$$Z_{f}^{'}(\omega) = \frac{R_{ct}}{(1-\theta)} + \frac{\sigma}{(\omega)^{1/2}} + \frac{\sigma}{\left[(1-\theta)(\omega)^{1/2}\right]} \tag{3.4}$$

The Θ magnitude is derived from the slope m of $Z'_f$ vs. $\omega^{-½}$ at higher frequency range, according to equation 3.5:

$$1-\theta=\frac{\sigma}{m-\sigma} \qquad (3.5)$$

The Warburg slope σ is obtained from unmodified bare gold at lower frequency range.

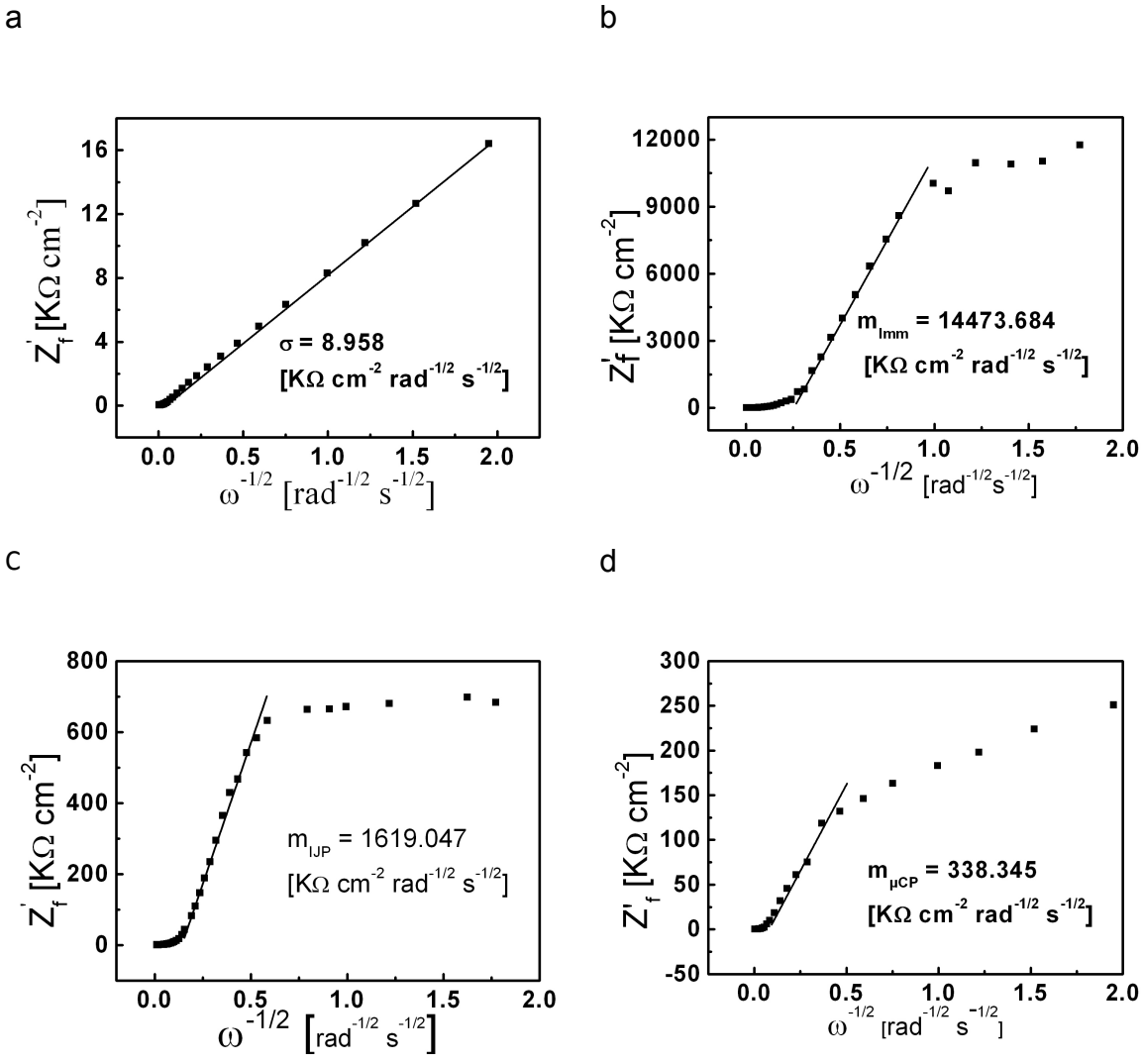


**Figure 3.6** Faradaic impedance of $Z'_f$ v.s. $\omega^{-1/2}$ of 1 mM $[Fe(CN)_6]^{-3}$ with 0.1 M KCl as the supporting electrolyte. Corresponding slopes at low-frequency region of each system are presented.

Figure 3.6 exhibits the $Z'_f$ vs. $\omega^{-½}$ of the systems investigated and the corresponding slope values. Plot (a) shows that $Z'_f$ varies linearly with $\omega^{-½}$ denoting Warburg impedance with slope of σ. It is also confirmed that the presence of monolayers alter qualitatively the subsequent plots, which is strongly related to the insulating properties of the monolayers. The surface coverage values estimated from equation 3.3 and equation 3.5 are summarized in Table 3.2. The resulting Θ values from both equations present the same tendency, i.e. the sequence immersion > IJP > µCP. The CV results follow the EIS results qualitatively. However, there is a difference in magnitude of Θ values calculated from equation 3.4 and equation 3.5. The Θ values calculated from eq. 3.5 are closer to the real state of the monolayers in which the $Z'_f$ comprises not only charge transfer resistance but also a mass transfer term associated with the microarray behavior[33], defect on the monolayers.

Overall, the results suggest that the monolayer of hexadecanthiol immobilized by the three techniques form an insulating monolayer with high surface coverage. The monolayer prepared by immersion overnight has the closest packed and the densest arrangement. This makes sense considering the adsorption kinetic[37-39], i.e. that in the initial step the thiolate moieties adsorb rapidly on a surface with Θ reaching 90%. Subsequently, the molecules rearrange themselves into a commensurate packed structure. On the other hand, the adsorption kinetic of a monolayer prepared by µCP or inkjet printing may be influenced by the fast printing technique. The molecular arrangement and insulating properties were further characterized by PMIRRAS and SECM.[40] From the positions and from the full width at half maximum (fwhm) of CH

stretching and bending modes, the average molecular arrangement of hexadecanthiolates prepared by IJP and immersion are almost identical, whereas μCP again shows lower crystallinity. Similar trends, results from the approaching curve mode in SECM. Here, IJP could be considered as a non–drying printing technique, like in μCP. Therefore, the monolayer prepared by IJP can benefit from the time before the solvent evaporates totally to rearrange it self. Overprinting of drops on a surface could possibly fill or refill the defects and increase the quality. In addition, a current study shows that molecular arrangement of monolayers on patterns prepared by μCP possesses better quality (i.e. close to that by immersion) than in a large plane.[41]

**Table 3.2** Fractional surface coverage of monolayers investigated

| | Θ* | Θ** |
|---|---|---|
| HDT μCP | 0.997 | 0.9727 |
| HDT IJP | 0.9996 | 0.9944 |
| HDT Immersion | 0.99997 | 0.9994 |

*) the values were calculated from eq. 3.3. **) the values were calculated from eq. 3.5

## 3. 3 Monolayer Formation on Evaporating Droplets

In this section, a phenomenon of monolayers stemming from single droplet is studied. This is of importance because the final structure of homogenous printing consists of an accumulation of neighboring, overshot droplets. The quality of inkjet–printed droplets in the 50 to several 100 μm range

is influenced by different parameters, such as the drop sizes, solvent–solute spreading, molecular diffusion of thiol molecules via the gas phase or via surface gliding after and during solvent evaporation, and the precision of positioning a series of droplets on the substrate. In the printer used, the droplet size is controlled by the piezo element and the volume is in range of 3 pL. As it is seen in Figure 3.1, the Epson printer shoots exclusively twins of droplets, the primary drop and its satellite, which is typical for Epson printers.[42]

The following processes are encountered during the process of inkjet printing: (i) Drops ejection from the nozzles tip, (ii) Flying of the drops in a free gap to a surface, (iii) Drops impact on the surface (iv) Spreading of the drop and (v) Drying. Ejection and flying phenomena have been described in chapter 1. In this section, the phenomenological study of impaction, spreading, and drying are emphasized. In printing “normal” ink on papers, the deposition quality is strongly influenced by interactions between the substrate (e.g. papers) and the absorbent material (e.g. inks). Surface modifications of paper surfaces are commonly conducted in the paper industries to meet the specific end–user requirements. To obtain a well shaped dot, excessive absorption of the liquid and the ink should be prevented while still allowing the ink to spread laterally.

On a solid non–absorptive surface, such as gold surface, the drops can be bouncing, spreading or splashing, depending on the condition of impaction[43-45]. Significant parameters include the properties of the drops, the properties of the substrate, kinetic parameters of the drop and the drop–to–substrate interactions[46]. In inkjet printing, spreading rather than bouncing or splashing is mostly encountered[43]. The drops expand radially reaching their maximal

diameter. Before reaching the final diameter, a drop can undergo expansion and contraction to dissipate excess energy from impact process[46]. The spreading takes only microseconds before the final diameter is reached (Figure 3.7).

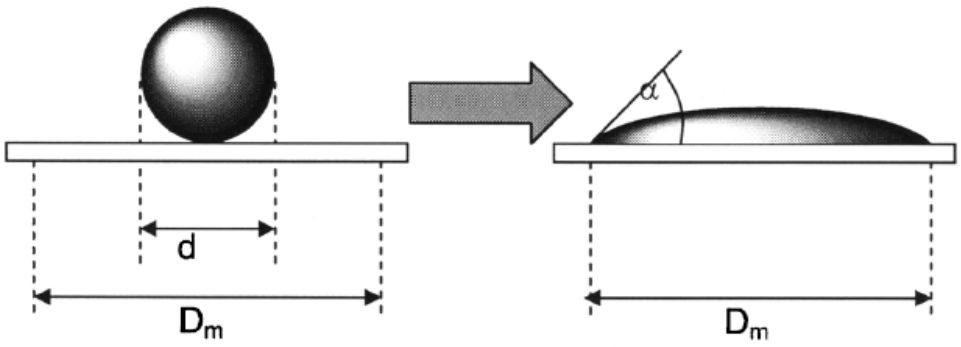


**Figure 3.7** Impaction and spreading of a drop on a flat non–adsorptive surface.[46]

The relative magnitude of a droplet diameter after and before spreading is termed as spreading ratio, (D'). For millimeter size drops, gravity affects the spreading ratio whereas on micrometer sized drops (i.e. inkjetted drops), the effect of gravity is less dominant.[46-48] Herein, liquid properties such as viscosity and surface tension have a more dominant effect. [46, 49] The ink properties used in this work are optimized to be as close as possible to the properties of the original EPSON inks. Glycerol which is normally used as a thickener is chosen as a co-solvent to increase, especially, the viscosity of the ink. The viscosity of 2.5 cPas is found to be suitable for the thiol system which is slightly lower than that of original ink (3.9 cPas).

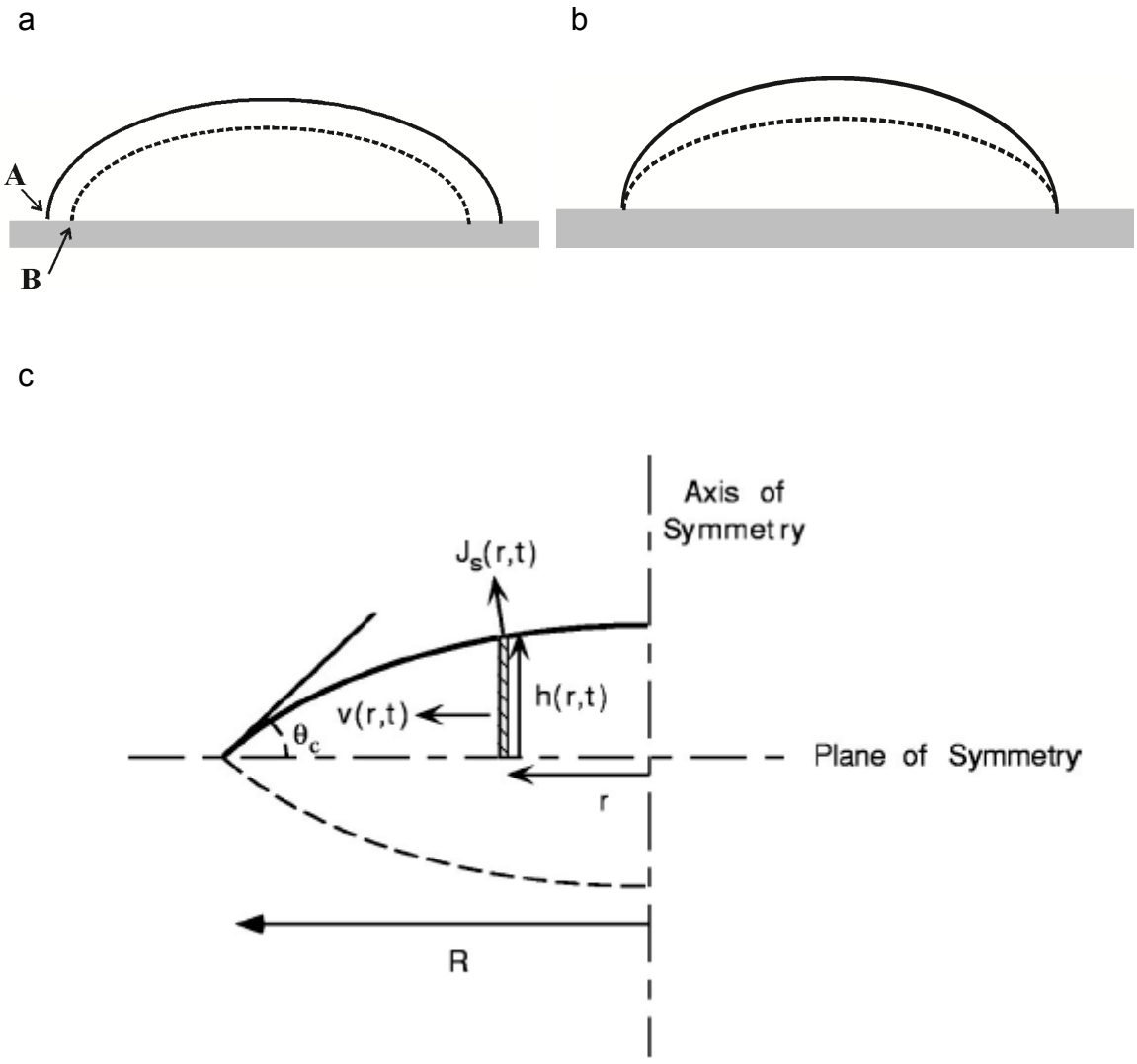


**Figure 3.8** Schematic of droplet–evaporation process of non-pinned edges doroplet (a) and pinned edges droplet (b). The mass transfer model during evaporation (c).[50, 51]

The droplet evaporation process and its influence on the resulting monolayer have been examined. An often observed phenomenon relating to evaporating solutions or suspensions on a surface is a ring–like deposit. The phenomenon is well–known as coffee stain effect which is named after a common dark ring deposit of coffee grains on a glass bottom occurring not only

in inkjet printing but also on drop–casting and spin–coating. Herein, the solutes in the droplets seem to be dragged to the droplets' boundary edge and rested there.

The phenomenon of coffee stains was first analyzed by Deegan et al.[50, 51] They observed ring–like deposits on various kind of surfaces, solvents and environmental conditions. The ultimate factors responsible for the creation of ring–like deposits are contact line pinning and fast evaporation from the edge of the drop. A general model of evaporating droplets is shown in Figure 3.8. A ring–like deposit will be created as soon as the interface boundary line is pinned on a surface. Herein, drag flows are created to compensate the fast evaporation at the droplet perimeter which induces forces driving outwardly. The magnitude of mass loss rate during evaporation ($J_s$) is linearly proportional to the distance between droplet radius (R), and the evaporated element (r), where R and r are influenced by the contact angle of the droplet, Φ (equation 3.6 and 3.7). The flows are able to transfer 100% of the solutes to the boundary edge. The model is in line with that of Hu and Larson[52] who reported that such drag flows dominate when the contact angle of the droplet is 2 – 4°. On the other hand, a uniform deposit will be obtained in the case of a non–pinned contact line whereby the interface boundary line shifts to the inner part as the evaporation propagates. They observed that uniform deposits will be resulted from droplets evaporated on a smooth Teflon surface and on lid covered glass.[51]

$$J_s (r,t) \sim (R - r)^{-\lambda} \qquad (3.6)$$

$$\lambda = \frac{(\pi - 2\theta)}{(2\pi - 2\theta)} \tag{3.7}$$

Ring–like deposits are unexpected in our system, even though they have been applied in studying DNA microarrays[53] and in preparing microstructure relief of etched polymer[54]. Convection flows are believed to bring back the solute from the perimeter to the innerside of the droplet, resulting in homogenous deposits.[55,56] The phenomenon is termed as Benard–Marangoni convection flows. The onset of the convection flows can be estimated by the Marangoni number (Ma),[57, 58] as shown in equation 3.8:

$$Ma = \frac{\Delta\gamma L}{\mu D_{AB}} \tag{3.8}$$

The $\Delta\gamma$ denotes the surface tension difference between the solvents used; L is the diameter of the droplet, μ is the viscosity of the solvent mixture, and $D_{AB}$ is the diffusion coefficient of the solvents used which was equal to 1.48 x $10^5$ $cm^2$ $s^{-1}$.[59]

The physical properties of the solvent used in ink are summarized in Table 3.3, with the droplet diameter d of 100 μm, the calculated Ma is 1.13 x $10^5$. The value is far more than $M_c$, the critical Marangoni number, an onset number of convection flow. Kaneda et al.[60] pointed out that the evaporation rate makes an effect on the resulting film configuration. Based on their study on inkjetted drops with diameter in the range of 30 – 100 μm, a homogenous drop was obtained at slower evaporation rate even though the drop edges are

pinned. They pointed out that the viscous effect, as a result of solute concentration, retards the outward flows. De Gans and Schubert[57] applied the similar principle, mixing high and low boiling point solvents in the ink used, to obtain homogenously printed films.

Beside many reports about coffee stain and the Marangoni on colloidal[58, 61, 62] and other systems[54, 63, 64], Biestch et al.[65] reported that the coffee stain effect can also be encountered in a monolayers system. They observed that a ring–like deposit which resulted after etching was created at low concentration of thiolates in the ethanolic ink. However, in a similar experiment, an enlargement of the drop diameter was observed, as the thiolates concentration in the ink increased (see Figure 3.9). Comparing the original Epson ink droplets on photopaper consisting of a pair of droplets (Figure 3.9(a)), the shape of the ethanol/glycerol ink on gold suggests that the pair has coalesced leading to the ellipsoidal shape observed in Figure 3.9(b). Droplets created with different thiol concentrations in the ink exhibits pairs of separate droplets as shown in Figure 3.9 (c) - (e). The size of the spots is approximately 30 $\mu$m for the 0.5 mM thiolate ink and 40 – 50 $\mu$m for the 1mM thiolate ink, and the center–to–center separation is 70 or 95 $\mu$m, respectively. At an ink concentration of 3 mM, a larger, ellipsoidal spot is visible (Figure 3.9(e)). The sizes of the optically observed glycerol ellipsoid in Figure 3.9(b) and the ellipsoidal spot observed with SECM for 3 mM ink are comparable, whereas the pairs of spots observed with SECM for 0.5 and 1 mM ink (30 $\mu$m and 40 – 50 $\mu$m diameter, respectively), as shown in Figure 3.9 (c) and (d), resemble those of original ink on paper (Figure 3.9(a)). As mentioned before, the coffee stain effect is

observed after solvents evaporation, but this is not the case for the deposited thiolates of the same droplet. Thus, in the system examined, thiol absorption from the ink onto the gold seems to be faster than the lateral spreading of the ethanol/glycerol. This is nicely reflected in the series of SECM measurements with varying thiol concentrations (Figure 3.9 (c) - (e)). In other words, thiol SAM disk diameters comparable to the impact diameter of the droplet can be achieved for well-adjusted minimum thiol concentration. Our results give evidence that surface reaction is faster than the lateral spreading even though viscous effect and in combination with Marangoni flow circulation also play a role, especially for the non–interacting glycerol.

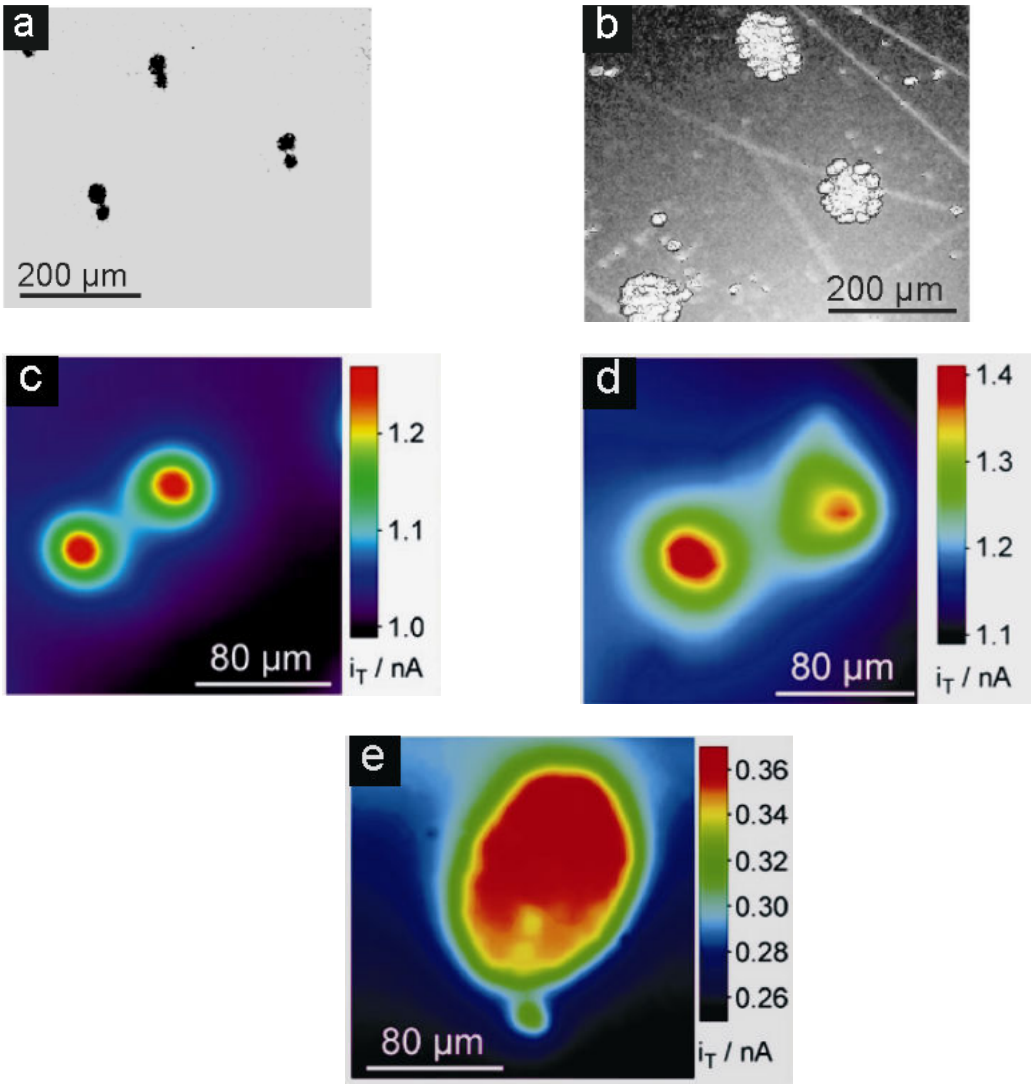


**Figure 3.9** Single inkjet disks prepared at 1% color density: (a) optical micrograph of Epson color on paper; (b) optical micrograph of HS-$(CH_2)_{10}$-COOH/glycerol ink on gold (washing step omitted); (c-e) SECM images of HS-$(CH_2)_2$-COOH ink on gold backfilled with HS-$(CH_2)_{15}$-$CH_3$ using HS-$(CH_2)_2$-COOH of 0.5 mM (c), 1 mM (d), 3 mM (e). Results are part of collaboration with University of Oldenburg and were published elsewhere.[40]

## 3. 4 References

(1) Beeson, R., Desktop inkjet product and perfromance study. In *IS&T Non - Impact Printing Conference*, San Diego, CA, 2002.

(2) Dubois, L. H.; Nuzzo, R. G. *Annual Review of Physical Chemistry* **1992**, *43*, 437-463.

(3) Widrig, C. A.; Chung, C.; Porter, M. D. *Journal of Electroanalytical Chemistry* **1991**, *310*, 335-359.

(4) Shadnam, M. R.; Kirkwood, S. E.; Fedosejevs, R.; Amirfazli, A. *Langmuir* **2004**, *20*, 2667-2676.

(5) Golzhauser, A.; Geyer, W.; Stadler, V.; Eck, W.; Grunze, M.; Edinger, K.; Weimann, T.; Hinze, P. *Journal of Vacuum Science and Technology B* **2000**, *18*, 3414-3418.

(6) Heister, K.; Zharnikov, M.; Grunze, M.; Johansson, L. S. O.; Ulman, A. *Langmuir* **2001**, *17*, 8-11.

(7) Zharnikov, M.; Grunze, M. *Journal of Vacuum Science & Technology B* **2002**, *20*, 1793-1807.

(8) Boubour, E.; Lennox, R. B. *Langmuir* **2000**, *16*, 4222-4228.

(9) Love, J. C.; Estroff, L. A.; Kriebel, J. K.; Nuzzo, R. G.; Whitesides, G. M. *Chemical Reviews* **2005**, *105*, 1103-1169.

(10) Helmuth, J. A.; Schmid, H.; Stutz, R.; Stemmer, A.; Wolf, H. *Journal of the American Chemical Society* **2006**, *128*, 9296-9297.

(11) Perl, A.; Reinhoudt, D. N.; Huskens, J. *Advanced Materials* **2009**, *21*, 2257-2268.

(12) Quist, A. P.; Pavlovic, E.; Oscarsson, S. *Analytical and Bioanalytical Chemistry* **2005**, *381*, 591-600.

(13) Larsen, N. B.; Biebuyck, H.; Delamarche, E.; Michel, B. *Journal of the American Chemical Society* **1997**, *119*, 3017-3026.

(14) Eberhardt, A. S.; Nyquist, R. M.; Parikh, A. N.; Zawodzinski, T.; Swanson, B. I. *Langmuir* **1999**, *15*, 1595-1598.

(15) Losic, D.; Shapter, J. G.; Gooding, J. J. *Langmuir* **2001**, *17*, 3307-3316.

(16) Balmer, T. E.; Schmid, H.; Stutz, R.; Delamarche, E.; Michel, B.; Spencer, N. D.; Wolf, H. *Langmuir* **2005**, *21*, 622-632.

(17) Love, J. C.; Wolfe, D. B.; Haasch, R.; Chabinyc, M. L.; Paul, K. E.; Whitesides, G. M.; Nuzzo, R. G. *Journal of the American Chemical Society* **2003**, *125*, 2597-2609.

(18) Mirsky, V. M.; Riepl, M.; Wolfbeis, O. S. *Biosensors & Bioelectronics* **1997**, *12*, 977-989.

(19) Boubour, E.; Lennox, R. B. *Journal of Physical Chemistry B* **2000**, *104*, 9004-9010.

(20) Campina, J. M.; Martins, A.; Silva, F. *Journal of Physical Chemistry C* **2007**, *111*, 5351-5362.

(21) Janek, R. P.; Fawcett, W. R.; Ulman, A. *Langmuir* **1998**, *14*, 3011-3018.

(22) Nahir, T. M.; Bowden, E. F. *Electrochimica Acta* **1994**, *39*, 2347-2352.

(23) Subramanian, R.; Lakshminarayanan, V. *Electrochimica Acta* **2000**, *45*, 4501-4509.

(24) Douglass, E. F.; Driscoll, P. F.; Liu, D. L.; Burnham, N. A.; Lambert, C. R.; McGimpsey, W. G. *Analytical Chemistry* **2008**, *80*, 7670-7677.

(25) Kerner, Z.; Pajkossy, T. *Electrochimica Acta* **2000**, *46*, 207-211.

(26) Strutwolf, J.; O'Sullivan, C. K. *Electroanalysis* **2007**, *19*, 1467-1475.

(27) Brug, G. J.; Vandeneeden, A. L. G.; Sluytersrehbach, M.; Sluyters, J. H. *Journal of Electroanalytical Chemistry* **1984**, *176*, 275-295.

(28) Sadkowski, A. *Journal of Electroanalytical Chemistry* **2000**, *481*, 222-226.

(29) Diao, P.; Guo, M.; Tong, R. T. *Journal of Electroanalytical Chemistry* **2001**, *495*, 98-105.

(30) Sabatani, E.; Cohenboulakia, J.; Bruening, M.; Rubinstein, I. *Langmuir* **1993**, *9*, 2974-2981.

(31) Porter, M. D.; Bright, T. B.; Allara, D. L.; Chidsey, C. E. D. *Journal of the American Chemical Society* **1987**, *109*, 3559-3568.

(32) Sabatani, E.; Rubinstein, I.; Maoz, R.; Sagiv, J. *Journal of Electroanalytical Chemistry* **1987**, *219*, 365-371.

(33) Finklea, H. O.; Snider, D. A.; Fedyk, J.; Sabatani, E.; Gafni, Y.; Rubinstein, I. *Langmuir* **1993**, *9*, 3660-3667.

(34) Diao, P.; Guo, M.; Tong, R. T. *Chinese Chemical Letters* **2000**, *11*, 1085-1088.

(35) Tokuda, K.; Gueshi, T.; Matsuda, H. *Journal of Electroanalytical Chemistry* **1979**, *102*, 41-48.

(36) Amatore, C.; Saveant, J. M.; Tessier, D. *Journal of Electroanalytical Chemistry* **1983**, *147*, 39-51.

(37) Bain, C. D.; Troughton, E. B.; Tao, Y. T.; Evall, J.; Whitesides, G. M.; Nuzzo, R. G. *Journal of the American Chemical Society* **1989**, *111*, 321-335.

(38) Schwartz, D. K. *Annual Review of Physical Chemistry* **2001**, *52*, 107-137.

(39) Schreiber, F. *Progress in Surface Science* **2000**, *65*, 151-256.

(40) Rianasari, I.; Walder, L.; Burchardt, M.; Zawisza, I.; Wittstock, G. *Langmuir* **2008**, *24*, 9110-9117.

(41) Lis, D.; Peremans, A.; Sartenaer, Y.; Caudano, Y.; Mani, A. A.; Dreesen, L.; Thiry, P. A.; Guthmuller, J.; Champagne, B.; Cecchet, F. *Journal of Physical Chemistry C* **2009**, *113*, 9857-9864.

(42) Beeson, R., Ink Jet Office & Home Desktop Inkjet Products Performance Study. In *29th Ink Jet and Thermal Printing Conferences* 2002.

(43) Rein, M. *Fluid Dynamics Research* **1993**, *12*, 61-93.

(44) Yarin, A. L. *Annual Review of Fluid Mechanics* **2006**, *38*, 159-192.

(45) Richard, D.; Quere, D. *Europhysics Letters* **2000**, *50*, 769-775.

(46) Park, H.; Carr, W. W.; Zhu, J. Y.; Morris, J. F. *American Institute of Chemical Engineers Journal* **2003**, *49*, 2461-2471.

(47) Dong, H. M.; Carr, W. W.; Bucknall, D. G.; Morris, J. F. *American Institute of Chemical Engineers Journal* **2007**, *53*, 2606-2617.

(48) Asai, A.; Shioya, M.; Hirasawa, S.; Okazaki, T. *Journal of Imaging Science and Technology* **1993**, *37*, 205-207.

(49) Bechtel, S. E.; Bogy, D. B.; Talke, F. E. *IBM Journal of Research and Development* **1981**, *25*, 963-971.

(50) Deegan, R. D.; Bakajin, O.; Dupont, T. F.; Huber, G.; Nagel, S. R.; Witten, T. A. *Nature* **1997**, *389*, 827-829.

(51) Deegan, R. D.; Bakajin, O.; Dupont, T. F.; Huber, G.; Nagel, S. R.; Witten, T. A. *Physical Review E* **2000**, *62*, 756-765.

(52) Hu, H.; Larson, R. G. *Journal of Physical Chemistry B* **2002**, *106*, 1334-1344.

(53) Blossey, R.; Bosio, A. *Langmuir* **2002**, *18*, 2952-2954.

(54) de Gans, B. J.; Hoeppener, S.; Schubert, U. S. *Advanced Materials* **2006**, *18*, 910-914.

(55) Girard, F.; Antoni, M.; Faure, S.; Steinchen, A. *Langmuir* **2006**, *22*, 11085-11091.

(56) Maroto, J. A.; Perez-Munuzuri, V.; Romero-Cano, M. S. *European Journal of Physics* **2007**, *28*, 311-320.

(57) de Gans, B. J.; Schubert, U. S. *Langmuir* **2004**, *20*, 7789-7793.

(58) Park, J.; Moon, J. *Langmuir* **2006**, *22*, 3506-3513.

(59) Lusis, M. A.; Ratcliff, G. A. *American Institute of Chemical Engineers Journal* **1971**, *17*, 1492-1496.

(60) Kaneda, M.; Ishizuka, H.; Sakai, Y.; Fukai, J.; Yasutake, S. *American Institute of Chemical Engineers Journal* **2007**, *53*, 1100-1108.

(61) Smith, P. J.; Shin, D. Y.; Stringer, J. E.; Derby, B.; Reis, N. *Journal of Materials Science* **2006**, *41*, 4153-4158.

(62) Fischer, B. J. *Langmuir* **2002**, *18*, 60-67.

(63) Lim, J. A.; Lee, W. H.; Lee, H. S.; Lee, J. H.; Park, Y. D.; Cho, K. *Advanced Functional Materials* **2008**, *18*, 229-234.

(64) Haupt, M.; Miller, S.; Sauer, R.; Thonke, K.; Mourran, A.; Moeller, M. *Journal of Applied Physics* **2004**, *96*, 3065-3069.

(65) Bietsch, A.; Hegner, M.; Lang, H. P.; Gerber, C. *Langmuir* **2004**, *20*, 5119-5122.

# Chapter 4: Lateral Structuring of Monolayers on Gold Surfaces

(This work is a part of a collaboration with University of Oldenburg and shared results are presented)

The capabilities of the inkjet printer as a straight forward, low cost tool to prepare microelectrodes are examined. Microdisk and band electrodes are easily prepared by printing droplets at low color intensities and lines, respectively. The corresponding electrochemical microelectrode behaviors are examined. It is also demonstrated that well defined band electrodes can be prepared easily by printing simultaneously a blocking and conductive thiols from two channels.

## 4. 1 Gold–based Microelectrode Fabrications

The result presented in the previous chapter has encouraged stepping a head into some obvious applications, i.e. the microelectrode fields. A microelectrode is defined as a conductive material with a dimension from a few to hundreds of micrometers, typically in the range of 100 μm, whereas a macroelectrode is in the range of at least several millimeters.[1, 2] For electrochemical analysis and sensor applications, microelectrodes have gained much research interest.

Recently, Compton et al.[3] reported a review about techniques used to fabricate different types and materials of microelectrodes. In this chapter, gold–based microelectrodes which are used in this work are highlighted. The gold–based materials are mostly used for electrochemical analysis because gold has high conductivity, well established protocols for its modifications as flat

materials or available as nanoparticles. It has been widely applied as a model substrate to study interfaces phenomena. There are two routes to fabricate microelectrodes, i.e. templating and molecular assembly.[3]

(a) Templating

In this method, treatments such as sputtering, etching and polishing are involved. Generally, the gold plates in the form of grids or wires with a size in the range of submicrons or micrometers are molded into thermosetting polymers, such as epoxy to fabricate microelectrode arrays. The resulting arrays are in 2-D either disks[4] or rectangular shaped[5] and each microelectrode can be addressed individually. Another approach is growing gold wires in polycarbonate porous membrane via electroless deposition method.[6] The initial microelectrode arrays are in 2D. When selective etching of the polycarbonate is introduced, a 3-D microelectrode array is obtained. By utilizing a similar approach, Zoski et al.[7] improved the polycarbonate based template method to fabricate regularly spaced, addressable microregions of nanoelectrode arrays. Furthermore, a high throughput of 3-D pyramid–like gold arrays has been fabricated[8, 9]. Herein, the resulting submicron size is originated from the size of fiber apexes that are shaped by multiple etching treatments.

(b) Molecular Assembly

In molecular assembly, the presence of microelectrodes was first discovered from the investigations on partially blocking of electrodes as a result of non–perfect monolayer modifications. The defects were then found to be useful to study kinetic of monolayer formation (see chapter 1). Due to the size, the defects have been found to be applied as microelectrodes. The nano- and

micrometersized of the defects have been observed by microscopic methods. Monolayer studies carried out by scanning tunneling microscopy and atomic force microscopy revealed that pit defects in the size of several nanometers on thiolates monolayers deposited on gold (single crystal or polycrystalline) show strong correlation of the relative arrangement of the thiolates and the gold substrate.[10-13]

On–purpose techniques have also been used to produce microelectrodes. Below three techniques are highlighted: selective desorptions, lithography, and printing. (i) In the selective desorption, chemsorbed thiolates on a gold surface are detached selectively to leave fractions of refreshed bare gold surfaces. In the electrochemical desorption, a certain potentials range is applied to the modified electrode in which the thiolates are oxidized and consequently, the sulfur–gold bond breaks. Only the exposed surfaces undergoes desorption and they can be used for immobilization of other systems, such as electrically addressable biological receptors[14] or thiolated DNA probes.[15] The selective desorption can also be done by making use of an electron beam or laser.[16, 17] However, the spatial resolution of microstructure prepared by selective desorption can not be adjusted and therefore, the resulting microelectrodes are arranged in random arrays.

The microcontact printing technique has caught most interest in preparing microstructures. Herein, the arrangement and lateral resolution is dependent on the reliefs on the stamp produced from a master that was fabricated by photolithography. Microelectrodes in the range of several micrometers until submicrometer size have been prepared.[18-20] Many reports

exhibited the applications of the stamped microstructures to study the specific interaction of biological moieties on monolayers.[21-25]

Only a few studies[26, 27] use the inkjet printing technique to prepare microelectrodes. The ultimate advantage is that no master is required which leads to a faster process. Therefore, it is of interest to explore further the capability of the inkjet printing technique on non–conventional substrates, i.e. gold electrodes. The resulting microstructures can be analyzed by electrochemical methods. Inkjet printing of thiols, with conventional printer, is limited to the structures of 40 µm in diameter or ellipsoidal structure of 40 x 80 µm because of satellite formation discussed in chapter 3.

### 4. 2 Electrochemical Behavior of Macro- and Microelectrodes

Owing to their small size, the electrochemical responses of the microelectrodes differ from those of macroelectrodes. Generally, the transition between macro- and microelectrodes behavior depends on the electrode dimension as compared to the thickness of the diffusion layer. Under diffusion control, the mass transport is driven by a concentration gradient at the electrode interface. Fick's laws describe the flux (i.e. rate of diffusion) and the concentration of an electroactive species as function of time and position. According to the first Fick's law, the flux is directly proportional to the concentration gradient. The time dependence on the gradient is reflected by Fick's second law and describes the thickness of the diffusion layer as a function of electrolysis time. This layer comprising the gradient is termed as

diffusion layer with a thickness, δ. For a planar semi–infinite diffusion, the diffusion layer thickness is expressed as:[2]

$$\delta = \sqrt{\pi Dt} \tag{4.1}$$

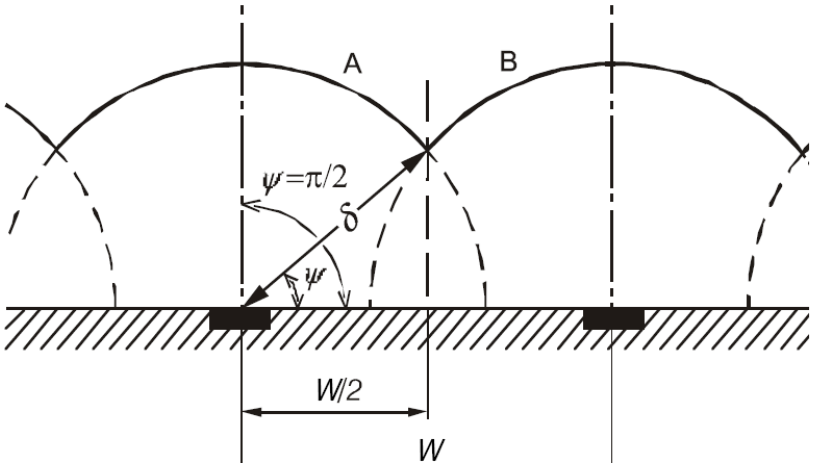


**Figure 4.1** Overlapping phenomena of diffusion layers built from a nearest pair of microelectrodes.[2]

Comparing δ and electrode size r (i.e. thickness and radius) leads to two limiting cases:

**a.** For δ <<< r, the flux occurs only in the inner parts of electrode surface and therefore, linear diffusion dominates. The current response is similar the conventional electrode with only smaller magnitude (Figure 4.1(a)).

**b.** For δ >>> r, the flux covers up the electrode surface. The diffusion at the electrode edges (i.e. edge effect) become important and so-called radial diffusion dominates. The current response amplifies and can resemble a steady–state transport (Figure 4.1(b)). In case of microelectrode arrays,

the overlapping diffusion layers between the nearest electrode pairs reduce the magnitude of the overall current response.

In this work, the fabrication of microelectrodes by inkjet printing technique in the form of disks and bands is demonstrated. The electrochemical responses are analyzed and the electrode morphologies are examined.

### 4.2.1 Disk Microelectrodes

Microdisk electrode arrays have been widely used for electroanalytical purposes. The disk microelectrodes are commonly arranged in a regular hexagonal or square lattice or in a random manner. The geometrical features of microdisks allow tuning of the signal and sensitivity, e.g. by control of the size and/or the distances between the electrodes. In addition, further manipulations of the surface allow for chemical modifications, towards (bio)sensor applications.[28, 29]

In this work, random microdisk electrode arrays were prepared by inkjet printing. The preparation is based on the appropriate choice of the densities of inkjetted droplets covering the surface. Before printing microdisk electrodes of thiolates, the coverage densities of the droplets upon color intensities adjustment were conducted. The experiments served as calibration and control. The printed droplets were analyzed under optical microscope.

At low color intensities, the droplet–satellite pairs are well separated whereas they become closer to each other and overlap as the color intensity increases. With the printer used, well–separated disk electrodes are obtained

for 1% to 10% color intensity. Partial overlapping starts in the range of 30 % color intensity and consequently, at 100 % color intensity all area is extensively overprinted. The size of the disk microelectrodes arrays produced by the original ink are in the range of 40 µm, as shown in Figure 4.2 and Table 4.1.

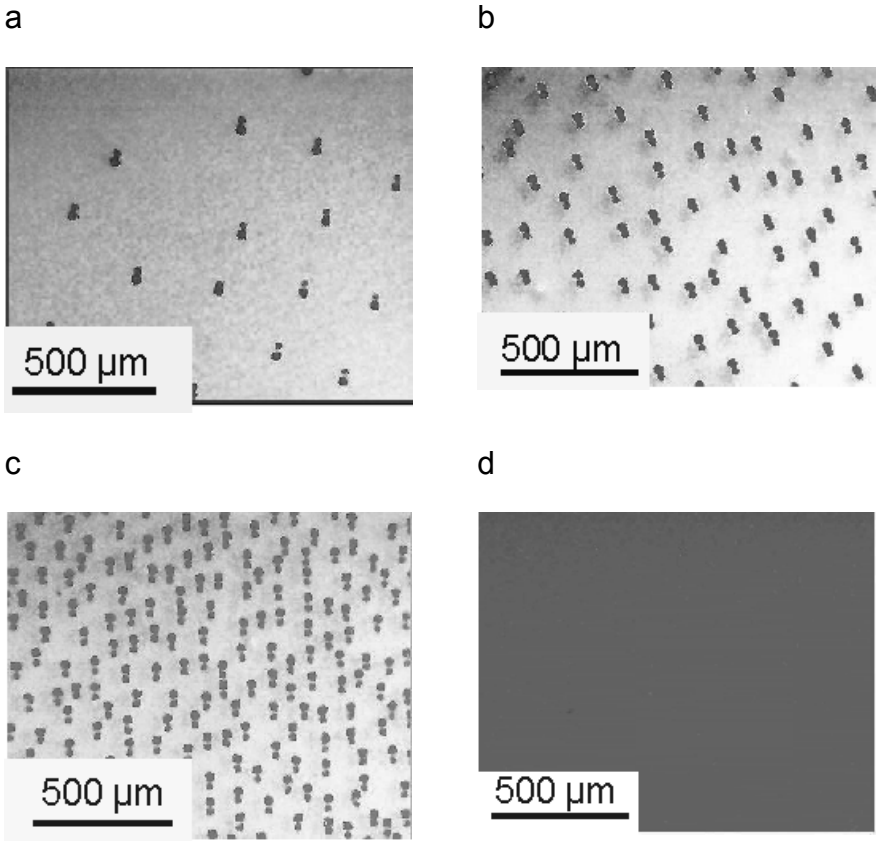


**Figure 4.2** Microscopic view of ink jetted original Epson ink on photo paper using (a) 1%, (b) 4%, (c) 10%, and (d) 100% color density on a surface of ~2.6 $mm^2$.

**Table 4.1** Color density, dot – dot distance, and surface coverage

| Color density [29] | 100 | 50 | 10 | 4 | 1 |
|---|---|---|---|---|---|
| Average distance of dots' center to center, dc-c [µm] | Fully overlap | < 40 | 80.3 | 107.14 | 392.86 |
| Surface occupation [%] | 100 | >80 | 23.46 | 8.9 | 1.85 |

The thiolate microdisk electrodes were prepared by printing mercaptopropionic acid of 1 mM in ethanol/glycerol ink on gold plates and the rest of the area was modified by hexadecanthiol by backfilling in ethanol for at least 1 h. Color intensities of 1, 4, 10, 50 and 100 % were introduced. The allover conducting and insulating behaviors of printed mercaptopropionic acid backfilled with hexadecanthiol were then investigated by cyclic voltammetry.

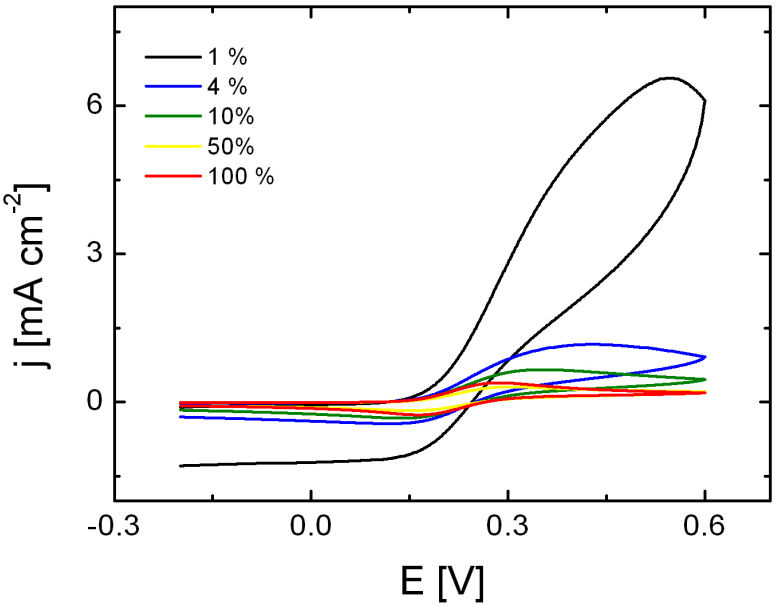


**Figure 4.3** Cyclic voltammograms of 1 mM ferrocenylethanol in 0.1 M KCl at HS-$(CH_2)_2$-COOH random array microdisk electrodes printed at different color densities. Substrates were backfilled with HS-$(CH_2)_{15}$-$CH_3$.

The voltammetric responses of ferrocenethanol (1 mM) on disks microelectrodes presented in Figure 4.3 were obtained from the center–to–center distances ($d_{c\text{-}c}$) of the nearest droplet pairs in the range of 0 – 392 µm. The scan rate used was 100 $mVs^{-1}$. Increasing color intensity leads to more droplets ejected from the printhead and consequently, the $d_{c\text{-}c}$ become smaller.

According to equation 4.1, the diffusion layer thickness is in the range of 142 µm ($D = 8 \times 10^{-10}$ $m^2$ $s^{-1}$ and $v = 100$ mV $s^{-1}$). From Table 4.1, it is obviously seen that a steady state behavior could be attained only at 1 % color intensity, even though the presence of satellites may be a complicated way.

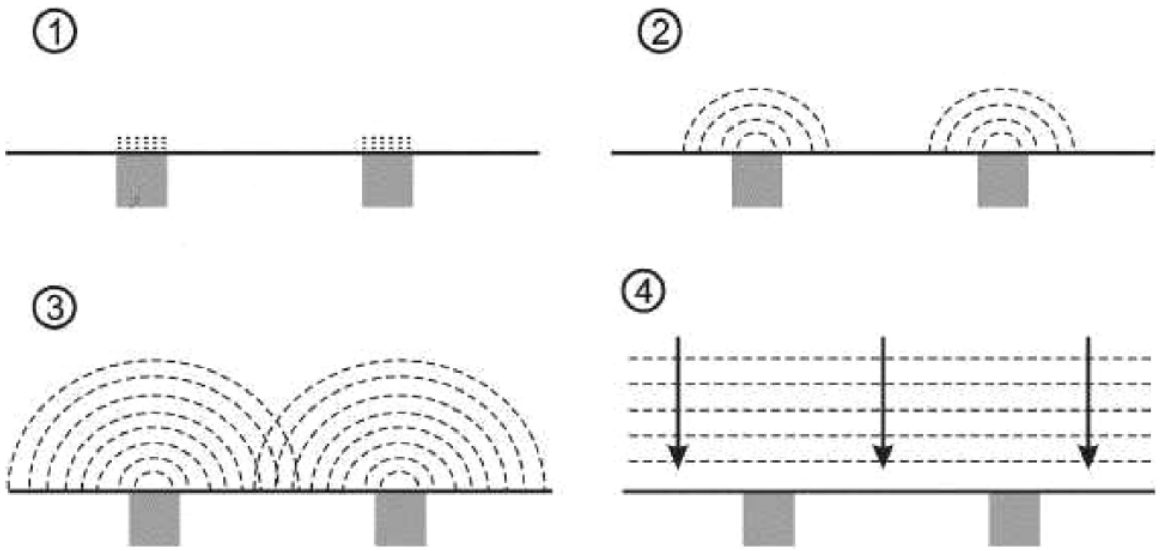


**Figure 4.4** Categories of diffusion layers on microdisk electrodes: Individual small diffusion layers (1), individual radial diffusion layers (2), overlapping of individual diffusion layers (3), and linear diffusion due to highly overlapping diffusion layers.[30]

The effect of overlapping diffusional spaces (also called as shielding effect) amplifies as the color intensity increases. The active sites (microelectrodes) get close to each other and the diffusion fields merge accordingly leading to an all-over planar diffusion layer (see Figure 4.3). Therefore, a transition from the steady state to conventional semi–infinite

responses is observed as a function of scan rate and electrode density. Such an interpretation is supported by peak–to–peak separation for forward and reverse scans, which becomes smaller and closer to the range of 59 mV for the case of 50% and 100% color intensities.

Theories and numerical simulations to elucidate the behavior of microdisk arrays (i.e. regular or random) have been developed.[30-34] Recently, Compton and coworkers suggested guidelines to analyze the electrochemical responses of microdisk electrodes arrays.[30, 32, 33] They derived and summarized four categories of diffusion layers in microdisk electrodes (Figure 4.4).

Bearing in mind that a diffusion layer extends proportionally with time, the development of the categories depicted above can be followed according to the scan rate (Table 4.2). Because most of the droplets are overlapping at 50% and 100%, they belong to the category – 4. The categories facilitate further insight into the voltammograms obtained as a function of scan rates. For example, the random microdisk array prepared with 10% color intensity with $d_{c\text{-}c}$ of 80.3 µm fits well to follow the categories changing. Herein, at 20 $mVs^{-1}$, a quasi–reversible voltammogram is obtained with peak–to–peak separation of 150 mV. The shape of voltammogram shifts to a sigmoidal shape for the scan rates of 500 mV $s^{-1}$ to 2000 mV $s^{-1}$. As it is described, the diffusion layers are fully overlapping at 20 mV $s^{-1}$ whereas they are partially overlapping at higher scan rates. The same principle also applies for the arrays prepared with 1 % and 4% color intensities (see appendix A for the voltammogram series). However, the presence of satellites affects the voltammogram shapes and yield to a combined behavior result. Thus, the results suggest that the complete behavior

of the microdisk array (category – 2) can not be obtained by the printer used in this study.

**Table 4.2** Classifications of the overall diffusion layers on the printed 10% disk microelectrodes. $D \approx 8 \times 10^{-10}$ m$^2$ s$^{-1}$.

| Scan rate [mV s$^{-1}$] | 20 | 50 | 100 | 500 | 1000 | 2000 |
|---|---|---|---|---|---|---|
| δ [µm] | 317 | 200 | 142 | 63 | 45 | 32 |
| Category | 4 | 4 | 4 | 2-3 | 2-1 | 2-1 |

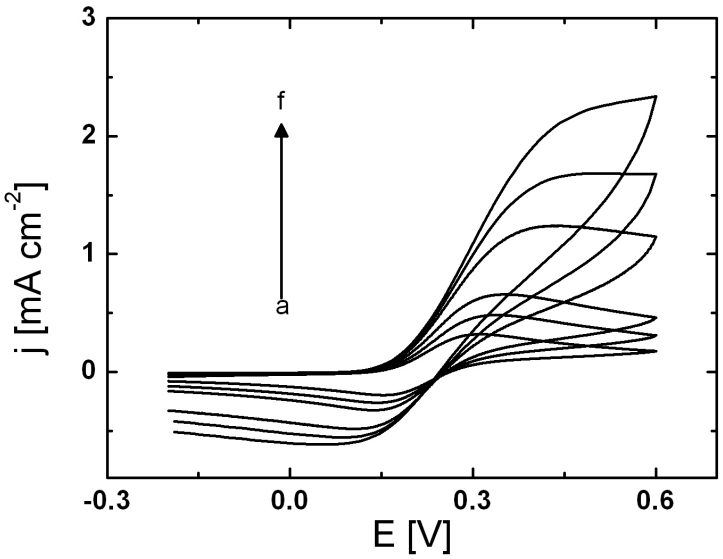


**Figure 4.5** Cyclic voltammograms of 1 mM ferrocenylethanol in 0.1 M KCl at HS-$(CH_2)_2$-COOH random array microdisk electrodes printed at 10 % color densities. Voltammograms show development of overall diffusion layers with scan rate of (a) 20 mV s$^{-1}$, (b) 50 mV s$^{-1}$, (c) 100 mV s$^{-1}$, (d) 500 mV s$^{-1}$, (e) 1000 mV s$^{-1}$, and (f) 2000 mV s$^{-1}$. Substrates were backfilled with HS-$(CH_2)_{15}$-$CH_3$.

### 4.2.2 Band Electrodes

Similar to disk electrodes, the band electrodes can be arranged as a single electrode or in array form (e.g. regular, random, or interdigitated arrays).[35, 36] In this work, band electrodes were prepared by printing side–by–side two thiols with different chain length. The band electrodes comprise mercaptopropionic acid or mercaptoundecanoic acid while the gap between the bands comprises hexadecanthiol. Hence, in the cyclic voltammetry, an electrochemically conducting strip within an insulating environmental was expected.

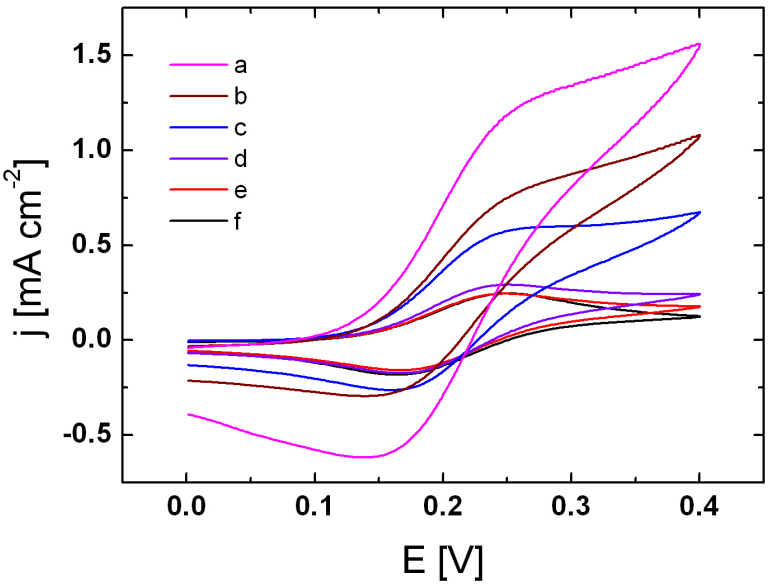


**Figure 4.6** Voltammograms of ferrocenylethanol (1 mM) in 0.1 M KCl at 100 mV $s^{-1}$ on band electrodes prepared by IJP using two-channel printing 1 mM HS-$(CH_2)_2$-COOH in EtOH/glycerol (channel 1) and HS-$(CH_2)_{15}$-$CH_3$ in EtOH/glycerol (channel 2), band widths: 300 $\mu$m (a), 500 $\mu$m (b), 1 mm (c), 3 mm (d), 5 mm (e), and 10 mm (f).

One of the interesting characteristics of the band (micro)electrodes is the geometrical dimension. Two–dimensional structures of a band (micro)electrode is featured by a small width–to–length ratio, i.e. the length can be centimeters while the width is in the micrometer range. Thus, the length contributes to the resulting current magnitude whereas the diffusion profile (i.e. hemicylindrical diffusion) is controlled by width.[37] This is in contrast to microdisk electrodes where the diffusion profile is controlled by the radius of the disks (i.e. the radial diffusion profile).

The electrochemical microelectrode behavior of an inkjetted single band electrode is presented in Figure 4.6. The band width is varied from 300 µm to 1000 µm. Simultaneous printing of the band electrodes is not only interesting for the fabrication of the microelectrode, but also to demonstrate the capability of inkjet–printed lines on a nonabsorptive surfaces. The CVs of ferrocenylethanol at the band electrodes denotes that the highest current density is obtained for a band width of 300 µm. The voltammogram shape is sigmoidal wave, as expected for a microelectrode. A transition of micro–to–macro electrode behavior is observed as the band width increases and the response of the 1 mm band electrode is identical with that of a macroelectrode.

Since the gold surface is nonabsorptive, the droplets spread and it was found that the limit of the inkjet printer used in this study are lines of 300 µm. This is demonstrated by the wavy edge of the line, indicating some misdirecting of the drops at the perimeter (see Figure 4.7(a) – (c)). The printing ability in preparing parallel lines was also demonstrated. Well–shaped lines consisting of

three parallel lines of 500 µm width were recorded by SECM (see Figure 4.7 (d)). More detail explanations regarding the SECM measurements are presented elsewhere.[27]

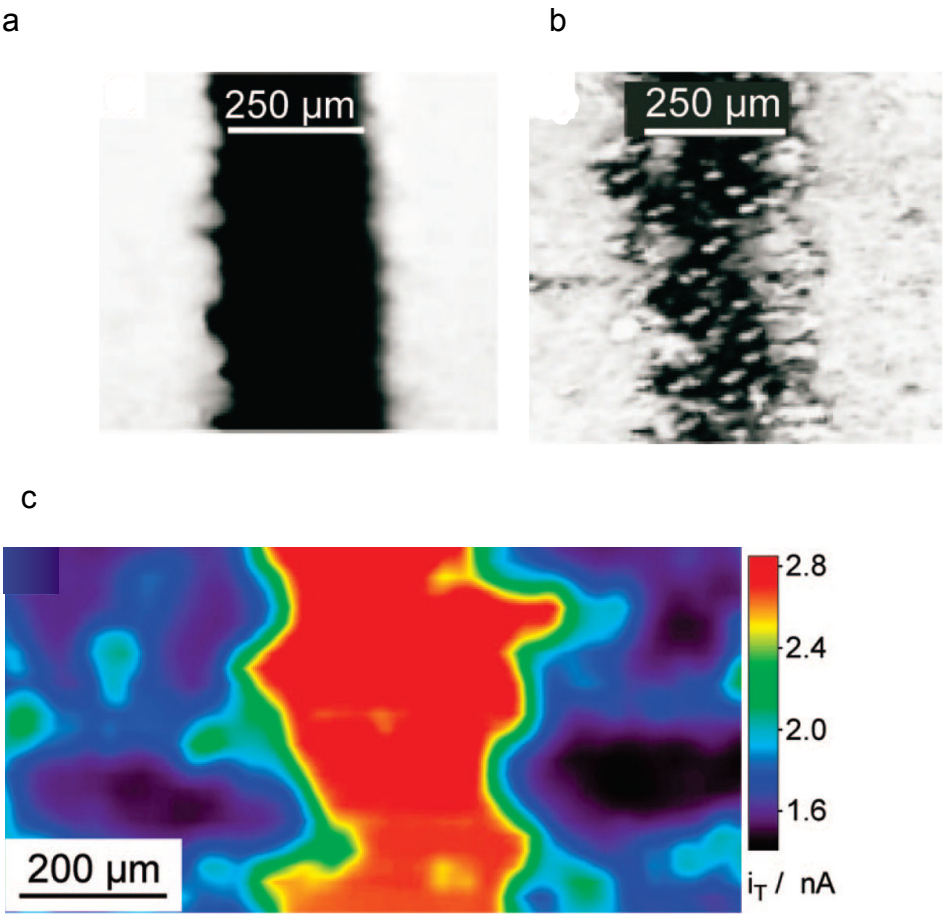


**Figure 4.7** IJP structures. (a, b) Optical micrograph of 300 *µ*m band structures, (a) Epson ink on paper and (b) HS-$(CH_2)_{10}$-COOH SAM line embedded in HS-$(CH_2)_{15}$-$CH_3$ on gold prepared in a single print job developed by water vapor condensation. (c) SECM image of a 300 *µ*m band structure of HS-$(CH_2)_{11}$-$NH_2$ embedded in HS-$(CH_2)_{15}$-$CH_3$. (d) SECM image of three HS-$(CH_2)_2$-COOH lines of 500 *µ*m width at 1000 *µ*m spacing embedded in HS-$(CH_2)_{15}$-$CH_3$. The results are a part of collaboration with University of Oldenburg and was published elsewhere.[27]

An important application of inkjetted band electrodes is their use for electrochemical sensing. The sensing mechanism is based on so — called "ion gatting" whereby the protonable terminal group of a SAM interacts electrostatically with the redox – active probe ions in the solution.[38, 39] Such a switchable line was prepared by inkjet printing amino undecanethiol while the rest area was backfilled with hexandecanthiol. The tunneling and blocking phenomena is demonstrated by SECM as shown in Figure 4.8. More detail explanations are presented elsewhere.[27]

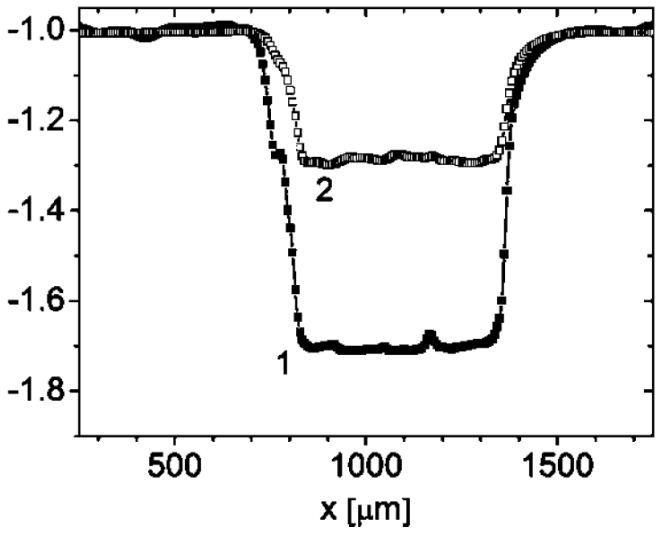


**Figure 4.8** SECM line scans at different pH values across a HS-$(CH_2)_{11}$-$NH_2$ SAM pattern backfilled with HS-$(CH_2)_{15}$-$CH_3$: curve 1 (filled symbols), pH 2.8 (open configuration); curve 2 (open symbols), pH 10.6 (closed configuration). Results are a part of collaboration with University of Oldenburg and was published elsewhere.[27]

## 4. 3 References


(1) Forster, R. J. *Chemical Society Reviews* **1994**, *23*, 289-297.

(2) Stulik, K.; Amatore, C.; Holub, K.; Marecek, V.; Kutner, W. *Pure and Applied Chemistry* **2000**, *72*, 1483-1492.

(3) Huang, X. J.; O'Mahony, A. M.; Compton, R. G. *Small* **2009**, *5*, 776-788.

(4) Lee, C. Y.; Tan, Y. J.; Bond, A. M. *Analytical Chemistry* **2008**, *80*, 3873-3881.

(5) Wu, H. P. *Analytical Chemistry* **1993**, *65*, 1643-1646.

(6) De Leo, M.; Kuhn, A.; Ugo, P. *Electroanalysis* **2007**, *19*, 227-236.

(7) Zoski, C. G.; Yang, N. J.; He, P. X.; Berdondini, L.; Koudelka-Hep, M. *Analytical Chemistry* **2007**, *79*, 1474-1484.

(8) Szunerits, S.; Walt, D. R. *Analytical Chemistry* **2002**, *74*, 1718-1723.

(9) Szunerits, S.; Garrigue, P.; Bruneel, J. L.; Servant, L.; Sojic, N. *Electroanalysis* **2003**, *15*, 548-555.

(10) Losic, D.; Shapter, J. G.; Gooding, J. J. *Journal of Solid State Electrochemistry* **2005**, *9*, 512-519.

(11) Banner, L. T.; Richter, A.; Pinkhassik, E. *Surface and Interface Analysis* **2009**, *41*, 49-55.

(12) Lee, S.; Bae, S. S.; Medeiros-Ribeiro, G.; Blackstock, J. J.; Kim, S.; Stewart, D. R.; Ragan, R. *Langmuir* **2008**, *24*, 5984-5987.

(13) Sondaghuethorst, J. A. M.; Schonenberger, C.; Fokkink, L. G. J. *Journal of Physical Chemistry* **1994**, *98*, 6826-6834.

(14) Riepl, M.; Mirsky, V. M.; Wolfbeis, O. S. *Mikrochimica Acta* **1999**, *131*, 29-34.

(15) Strutwolf, J.; O'Sullivan, C. K. *Electroanalysis* **2007**, *19*, 1467-1475.

(16) Olsen, C.; Rowntree, P. A. *Journal of Chemical Physics* **1998**, *108*, 3750-3764.

(17) Tender, L. M.; Worley, R. L.; Fan, H. Y.; Lopez, G. P. *Langmuir* **1996**, *12*, 5515-5518.

(18) He, H. X.; Li, Q. G.; Zhou, Z. Y.; Zhang, H.; Li, S. F. Y.; Liu, Z. F. *Langmuir* **2000**, *16*, 9683-9686.

(19) Libioulle, L.; Bietsch, A.; Schmid, H.; Michel, B.; Delamarche, E. *Langmuir* **1999**, *15*, 300-304.

(20) Delamarche, E.; Schmid, H.; Bietsch, A.; Larsen, N. B.; Rothuizen, H.; Michel, B.; Biebuyck, H. *Journal of Physical Chemistry B* **1998**, *102*, 3324-3334.

(21) Grunwald, C.; Eck, W.; Opitz, N.; Kuhlmann, J.; Wolf, C. *Physical Chemistry Chemical Physics* **2004**, *6*, 4358-4362.

(22) Zhao, C.; Zawisza, I.; Nullmeier, M.; Burchardt, M.; Taduble, M.; Witte, I.; Wittstock, G. *Langmuir* **2008**, *24*, 7605-7613.

(23) Park, T. J.; Lee, S. Y.; Lee, S. J.; Park, J. P.; Yang, K. S.; Lee, K. B.; Ko, S.; Park, J. B.; Kim, T.; Kim, S. K.; Shin, Y. B.; Chung, B. H.; Ku, S. J.; Kim, D. H.; Choi, I. S. *Analytical Chemistry* **2006**, *78*, 7197-7205.

(24) Zhou, Y.; Valiokas, R.; Liedberg, B. *Langmuir* **2004**, *20*, 6206-6215.

(25) Howell, S. W.; Inerowicz, H. D.; Regnier, F. E.; Reifenberger, R. *Langmuir* **2003**, *19*, 436-439.

(26) Richter, E. M.; Munoz, R. A. A.; Bertotti, M.; Angnes, L. *Electrochemistry Communications* **2007**, *9*, 1091-1096.

(27) Rianasari, I.; Walder, L.; Burchardt, M.; Zawisza, I.; Wittstock, G. *Langmuir* **2008**, *24*, 9110-9117.

(28) Justin, G.; Rahman, A. R. A.; Guiseppi-Elie, A. *Electroanalysis* **2009**, *21*, 1125-1134.

(29) Laczka, O.; Ferraz, R. M.; Ferrer-Miralles, N.; Villaverde, A.; Munoz, F. X.; del Campo, F. J. *Analytica Chimica Acta* **2009**, *641*, 1-6.

(30) Davies, T. J.; Compton, R. G. *Journal of Electroanalytical Chemistry* **2005**, *585*, 63-82.

(31) Lee, H. J.; Beriet, C.; Ferrigno, R.; Girault, H. H. *Journal of Electroanalytical Chemistry* **2001**, *502*, 138-145.

(32) Belding, S. R.; Dickinson, E. J. F.; Compton, R. G. *Journal of Physical Chemistry C* **2009**, *113*, 11149-11156.

(33) Menshykau, D.; Huang, X. J.; Rees, N. V.; del Campo, F. J.; Munoz, F. X.; Compton, R. G. *Analyst* **2009**, *134*, 343-348.

(34) Amatore, C.; Saveant, J. M.; Tessier, D. *Journal of Electroanalytical Chemistry* **1983**, *147*, 39-51.

(35) Streeter, I.; Compton, R. G. *Journal of Physical Chemistry C* **2007**, *111*, 15053-15058.

(36) Streeter, I.; Fietkau, N.; Del Campo, J.; Mas, R.; Munoz, F. X.; Compton, R. G. *Journal of Physical Chemistry C* **2007**, *111*, 12058-12066.

(37) Wehmeyer, K. R.; Deakin, M. R.; Wightman, R. M. *Analytical Chemistry* **1985**, *57*, 1913-1916.

(38) Degefa, T. H.; Schon, P.; Bongard, D.; Walder, L. *Journal of Electroanalytical Chemistry* **2004**, *574*, 49-62.

(39) Schon, P.; Degefa, T. H.; Asaftei, S.; Meyer, W.; Walder, L. *Journal of the American Chemical Society* **2005**, *127*, 11486-11496.

# Chapter 5: Mixing and “Gradient” Formations of Thiolates by Inkjet Printing on Gold

Chemical surface gradients have been considered as a straight forward tool to investigate interfacial phenomena. The capabilities of the inkjet to dispense picolitre drops and the presence of multichannels on its printhead have opened a new technique to prepare gradients of monolayers in a controled manner. Herein, it is attempted to prepare the monolayer gradients either by printing from one channel or simultaneously from two channels. The gradient steepness which is indicated by the gradual change of the surface modifier composition is derived from the electrochemical responses in cyclic voltammetry. The mixing behaviors of the monolayers are also investigated by condensation observed under optical microscope.

## 5.1 Chemical Gradient of Thiolates on Gold Surfaces

A mix of two constituents (e.g. two different thiolates) forming a single monolayer allows a superior control in respect to the surface chemical properties on a certain area depending on mixing parameters adjusted, such as functional groups and chain length. The role of the surface properties is significant in elucidating phenomena at the interfaces, for example, the effect of surface wettability and its influences on the protein adhesion, the attachment and growth of cells or bacteria, or the haptotaxis of a neuron cell.[1-3] Mixed SAMs are also useful to avoid a high density of surface functional groups which lead to steric hinderances or less ordered structure due to bulky terminal

functional groups. Furthermore, introducing different compositions of functional groups on the same surface plane provide a template for investigating selective reactions on the surfaces.

In the conventional way, each parameter is investigated by preparing many individual samples and requiring many measurement repetitions. This approach takes much time and materials to investigate single interface phenomenon. However, when the change of the surface properties is prepared in a gradual manner on a plane surface, the physicochemical phenomena encountered on the systems can be investigated in a fast and effective way, as each position is related to a certain mol fraction. In addition, the resulting gradient offers flexibility in changing the different parameters on the same surface. Much data can be resolved in minimum of time, which is also known as a combinatorial approach.

Generally, two paths are described in the preparation of a chemical gradient of thiolates in monolayers, i.e. top down and bottom up. In the top down path, a homogenous monolayer immobilized on a surface is modified gradually to form a gradient. The modifications are conducted, for example, by inducing a gradually change of potential along the surface plane, so that the thiolates desorb in a gradual manner depending on the induced potential at a given position.[4-8] Subsequently, the exposed bare gold surfaces, due to desorption of the thiolates, are immersed in another thiol solution to modify the exposed areas. In a similar way, mixture of thiolates can be prepared by selective etching by using a laser beam[9, 10] or dip pen lithography[11]. Inducing a

single, homogenous thiolate monolayer into a second thiolate solution can also result in a mixed, binary monoalyers.[12]

In the bottom up path, the gradual surface properties are built by modifying along the bare surface plane by thiolates adsorbate in a gradual manner. The bottom up path is more preferable than the aforementioned top-down, because the surface properties on a surface are easier to adjust. Herein, different mixtures of thiolates are prepared by immersion–based, soft–lithography, and inkjet printing techniques. In the immersion–based techniques, the gradient can be prepared by cross diffusion of two thiols solution thorough a porous sepandex membrane[13, 14], immersing the substrates into a solution comprising two thiolates[15, 16], and inducing sequential steps of immersions[17, 18]. In the soft-lithographic technique, the mass transfer of the thiolates from the stamp bulk to the surface determines the steepness of the resulting gradient. Kraus et al.[19] utilized a triangle–shaped polydimethylsiloxane stamp to prepare a gradient of single thiolate whereby the mass–transfer and diffusion depending on the variation of the stamp thickness was investigated.

Despite the flexibilities and the well controlled system of inkjet printing technique, preparations of thiolates gradients by the inkjet printing technique are less explored.[20] In the inkjet printing technique, a gradient of thiols in a monolayer can be prepared by (i) printing a monolayer with changing density and immersing the printed thiols into the second thiolate solution (backfilling) and (ii) printing two thiolate solutions from different solution channels simultaneously with increment and decrement densities. To the latter, the ink channels at the printhead are already calibrated and the data can be applied as

the references. In this work, the printing–backfilling sequence as well as the simultaneous printing paths are exploited. The resulting surface compositions, the steepness of the gradients and the mixture behaviors of the binary thiolates are investigated.

## 5.2 Preparation of a Ferrocene Monolayer Gradient by Applying One Inkjet Channel.

In this section, the preparation of gradient of monolayers by backfilling is explored. The thiol solution was filled into the yellow cartridge and different color intensities (i.e. different molar fractions) were printed onto different gold substrates. Subsequently, the substrates were immersed into the second thiol solution to modify the rest area.

a b

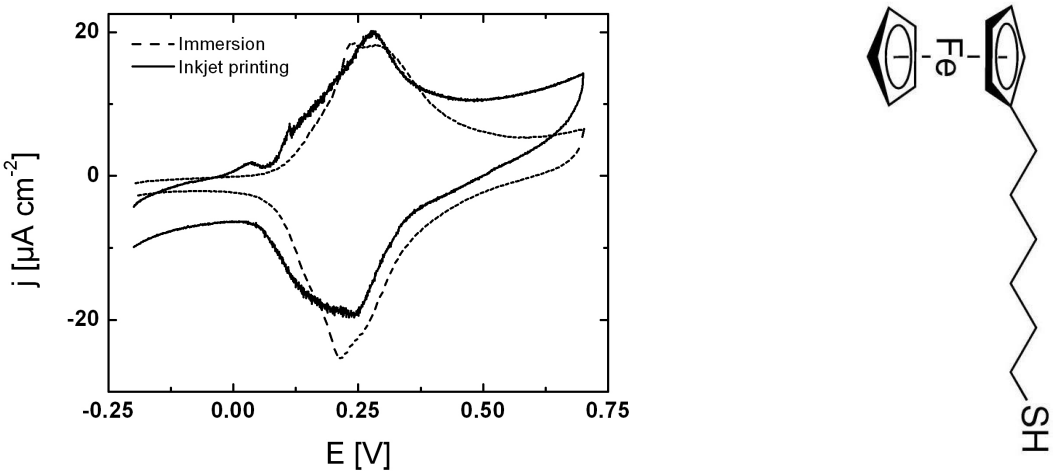


**Figure 5.1** Cyclic voltammograms in 1 M $HClO_4$ of ferrocenylhexanethiol prepared by immersion and inkjet printing with scan rate of 100 mV $s^{-1}$ (a) and chemical structure of 6 – ferrocenyl hexanethiol (b).

A convenient way to determine a surface composition is to label one of the thiols with an electroactive group. Ferrocene functionalized thiols are interesting candidates for this purpose. The ferrocene group is an outer–sphere redox active molecule (Figure 5.1(b)). The electroactive response can be detected by the non–destructive electroanalytical method (e.g. cyclic voltammetry) which can be performed within minutes. Incorporation of ferrocene functionalized thiols in mixed monolayers with n-alkanethiolates has been widely studied, for example as models in electron transfer on surfaces[12, 21, 22] or in understanding the defect phenomenon on monolayers[23]. The surface coverage of ferrocene functionalized thiol can be determined by intergrating the voltammetric wave to obtain surface charges (Q) and dividing the charge by the number of electron involved (n), Faradaic constant (F), and the surface area of the substrate (A), as shown in equation 5.1.

$$\Gamma = \frac{Q}{nFA} \tag{5.1}$$

As a first attempt, 2 mM ferrocenylhexanthiol solution was printed homogenously on planar gold surfaces. The result is compared with the same monolayer prepared by immersion overnight. Figure 5.1(a) presents the corresponding voltammogram responses. The surface coverages obtained are $3.6 \times 10^{-10}$ mol cm$^{-2}$ and $2.7 \times 10^{-10}$ mol cm$^{-2}$ for the immersed and inkjet printed samples, respectively. Chidsey et al.[21] reported that the maximum coverage of ferrocene on gold (111) is $4.5 \times 10^{-10}$ mol cm$^{-2}$ with an assumption that the ferrocene moieties are in form of spheres with a diameter of 6.6 Á. The surface

coverages obtained in this experiment are lower than the calculated value which is explained by the poorly packing due to shorter alkane chain.

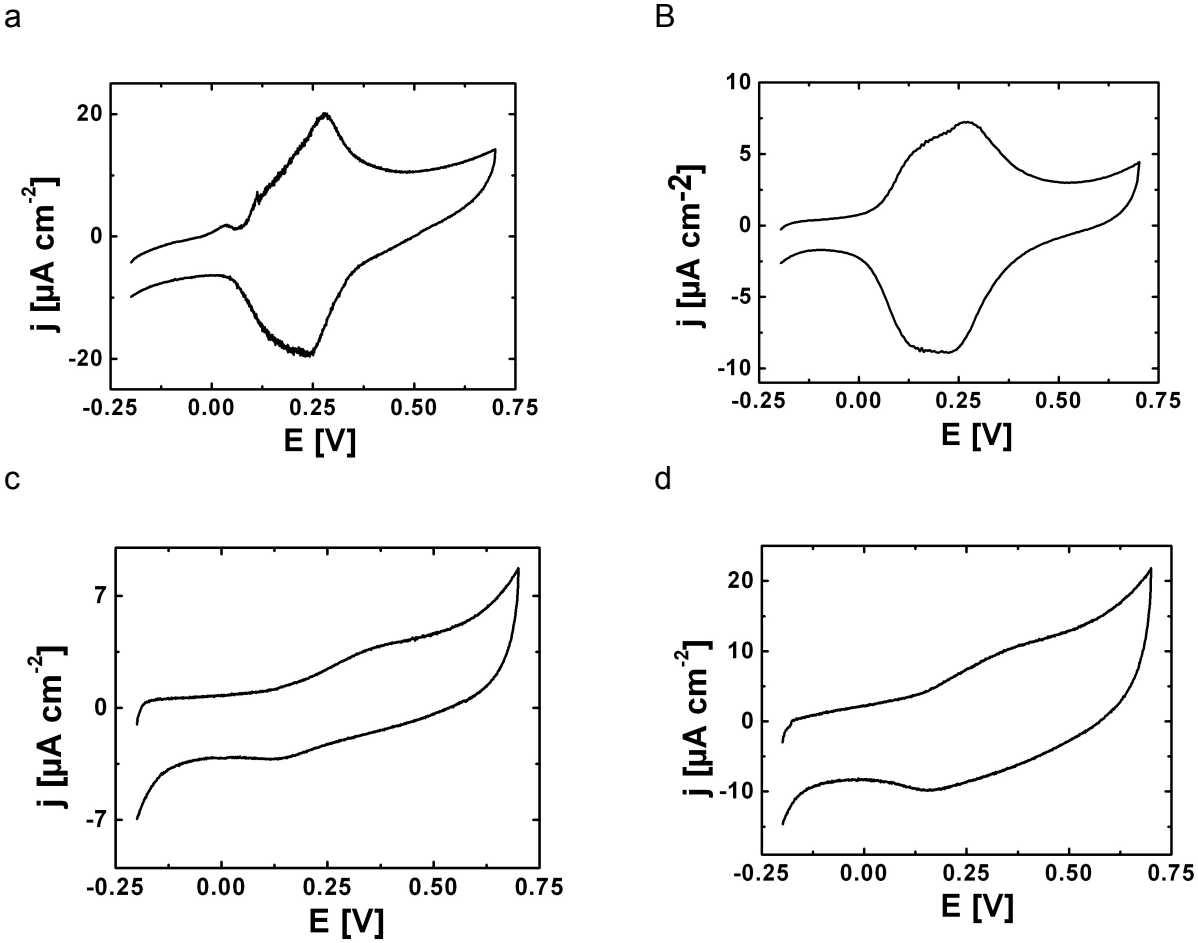


**Figure 5.2** Cyclic voltammogram of ferrocenylhexanthiol printed of different color intensities: 100% (a), 50% (b), 10% (c) and 1% (d). No backfilling step is conducted. Supporting electrolyte is 1 M $HClO_4$ and scan rate is 100 $mVs^{-1}$.

The “gradient” was then prepared by printing the same solution containing ferrocenylhexanol with different color intensities and the voltammograms were recorded (Figure 5.2). A gradual decrease of ferrocene coverage with the color intensities was observed. The surface coverages are 2.7 x $10^{-10}$ mol $cm^{-2}$, 1.5 x $10^{-10}$ mol $cm^{-2}$, 0.3 x $10^{-10}$ mol $cm^{-2}$, and 0.2 x $10^{-10}$

mol $cm^{-2}$ for 100%, 50%, 10%, and 1%, respectively. At higher ferrocene coverage (Figure 5.2(a)), ferrocene oxidation and reduction peaks are symmetric with peaks separations less than 90 mV indicating a fast rate of electron transfer. However, the peaks become broaden, asymmetric, and shifted (i.e. towards positive and negative for oxidation and reduction, respectively) at lower ferrocene coverages (Figure 5.2(b) - (d)). The voltammogram responses of 10% and 1% color intensities also exhibit high capacitive current due to the presence of unmodified area on the gold surfaces.

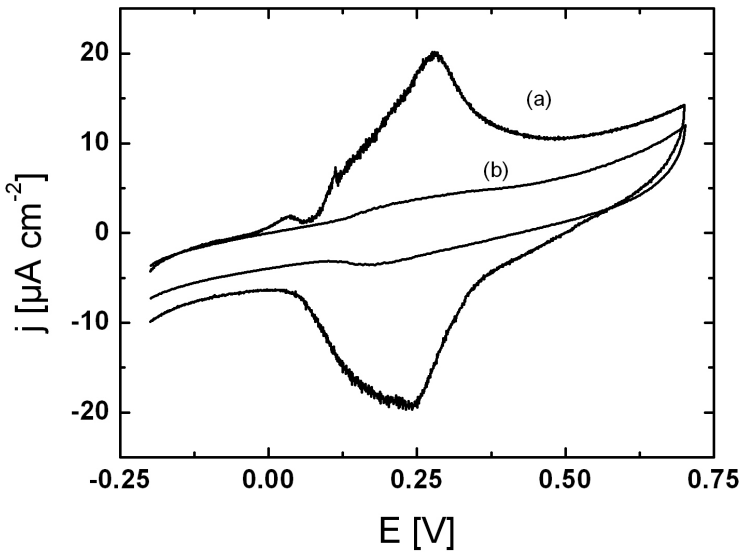


**Figure 5.3** Cyclic voltammograms of inkjetted ferrocenylhexanthiol: before (a) and after (b) immersion in 1 mM Hexanthiol overnight. Supporting electrolyte is 1 M $HClO_4$ and scan rate is 100 mV $s^{-1}$.

To prepare a binary gradient, each printed substrate comprising different concentration of ferrocene was directly immersed into the second alkanethiol solution. The backfilling solution was 1 mM hexanethiol in absolute ethanol. The

voltammogram responses show almost no current (Figure 5.3(b)). It seems that more than 90% of the ferrocenehexanethiolates are replaced by hexanthiolates. Immersing the inkjetted ferrocenylhexanethiol in 1 mM butanethiol for 1h also reveal the same results, i.e. the voltammograms exhibit only capacitive behavior (see Figure B.1 in appendix B).

a b

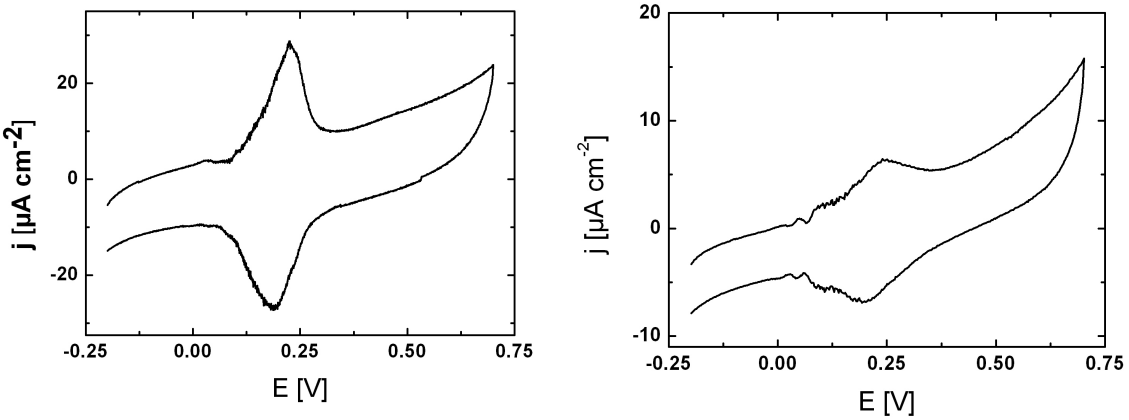


**Figure 5.4** Exchange reaction on butanethiolates (a) and hexanthiolates (b) on gold after immersion in 1 mM ferrocenylhexanethiol. Corresponding ferrocene coverage is 1.9 x $10^{-10}$ mol $cm^{-2}$ and 4.8 x $10^{-11}$ mol $cm^{-2}$ for butanethiols and hexanethiol, respectively. Supporting electrolyte is 1 M $HClO_4$ and scan rate is 100 mV $s^{-1}$.

The exchange reaction is then examined with the reverse sequence, where the alkanethiol was printed first and then the substrates were immersed in 1 mM ferrocenylhexanethiol solution. As a control experiment, electrodes overnightly immersed in butanethiol and hexanethiol were subsequently immersed in the ferrocenylalkanethiol for 1h (Figure 5.4). The resulting voltammograms demonstrate that the exchange reaction also occurs in this

sequence, i.e. the ferrocene thiolates replace the first thiol during the second immersion. The results suggest that a longer alkanechain length is required to avoid exchange reaction during immersion.

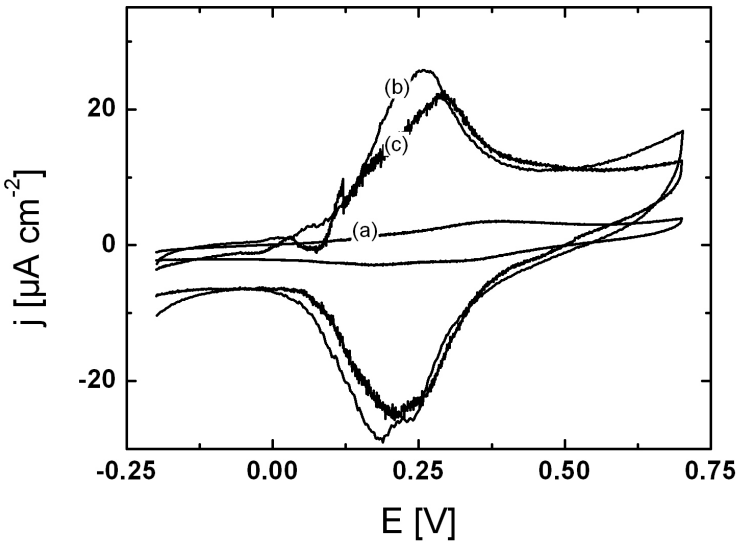


**Figure 5.5** Exchange reaction on hexadecanethiol inkjetted at 100 % (a) and 10% (b) color intensities on gold substrates after immersion in 1 mM ferrocenylhexanethiol. Voltammogram of inkjetted ferrocenylhexanthiol at 100 % color intensity (c). Supporting electrolyte is 1 M $HClO_4$ and scan rate is 100 mV $s^{-1}$.

The gold substrates were printed using solutions containing hexadecanthiol and subsequently the substrate was immersed in 1 mM ferrocenylhexanthiol for 1h. The resulting voltammogram from 100% color intensity exhibits a negligible exchange reaction to the ferrocenethiolates (Figure 5.5(a)). However, the voltammogram response obtained from 10% color intensity is similar to that obtained from 100% color intensity (Figure 5.5(b) and (c)), which is astonishing. Such broadened voltammogram features were also observed by Chidsey et al.[21] for the ferrocene teminated alkanethiols

($Fc(CH_2)_nSH$). They pointed out that broadened features may be caused by interactions between ferrocene at higher surface concentration. The thermodynamically ideal surface chemistry may be exhibited by the presence of a polar ester group in the ferrocene terminated alkanechain, e.g. $FcCO_2H(CH_2)_nSH$, at low surface concentration. Thus, the results suggest that at 10% color intensity, the ferrocene functional groups are close enough to interact to each other, which results in a voltammogram feature resembling to that of 100%. Another factor that could play a role is the roughness of the gold surface which may induce exchange reactions during backfilling.[20, 23-25]

## 5.3 Preparation of a Direct Binary Monolayers Gradient by Applying Simultaneous Printing

In the previous section, it was described that the monolayer gradients prepared by printing only from one channel is prone of exchange reactions after backfilling into the second thiol solution. This may lead to a miscalculation of the surface concentration. Since the printhead consists of several channels, the preparations of monolayer gradients making a use of dual channels are exploited.

Each of magenta and cyan channels consists of two different reservoirs. In applying two channels, two varieties of preparing gradients are distinguished that are pixel–based and droplet–based gradients. In the pixel–based gradient, the compositions are built by arranging the combinations of pixel–sized colors cells on a surface plane. The resulting compositions on the surface were calculated from the absorbance spectra of the EPSON inks used. The pixel with

side length of 40 μm was found to be the smallest that can be printed by the inkjet printer. Table 5.1 represents the surface composition ejected from each color combination in the pixel–based gradient. The corresponding spectra are presented in Figure B.2 in appendix B. In the droplet–based gradients, the compositions are adjusted by varying the color hues. The volume densities ejected from the ink reservoirs are already calibrated, as described in chapter 2, and the selective combinations are presented in Table 5.2 and Table B.1 in appendix B.

**Table 5.1** Surface compositions results from Magenta and Cyan channels on the pixel–based mixtures.

| Magenta, M [26] | $A_{520\ nm}$ (a) | $\Gamma_M \times 10^{-9}$ (b) [mol $cm^{-2}$] | $n_M$ | $n_C$ | $\Gamma_C \times 10^{-9}$ (b) [mol $cm^{-2}$] | $A_{610\ nm}$ (a) | Cyan, C [%] |
|---|---|---|---|---|---|---|---|
| 0 | 0 | 0 | 0 | 1 | 0.5602 | 2.0628 | 100 |
| 25 | 0.438 | 0.1981 | 0.32 | 0.68 | 0.4188 | 1.542 | 75 |
| 50 | 0.8 | 0.3618 | 0.56 | 0.44 | 0.2845 | 1.0476 | 50 |
| 75 | 1.1241 | 0.5084 | 0.78 | 0.22 | 0.1460 | 0.5376 | 25 |
| 100 | 1.517 | 0.6860 | 1 | 0 | 0 | 0 | 0 |

(a) Values are corrected toward Absorbance at 900 nm
(b) Surface concentration for 1 mM thiol solution

**Table 5.2** Surface compositions results from Magenta and Cyan channels on the droplet–based mixtures.

| Magenta,M [%] | $\Gamma_M$ [mol $cm^{-2}$] | $x_M$ | $x_C$ | $\Gamma_C$ [mol $cm^{-2}$] | Cyan, C [%] |
|---|---|---|---|---|---|
| 100 | 0.7432 | 1 | 0 | 0.0000 | 0 |
| 64 | 0.7213 | 0.76 | 0.24 | 0.2291 | 36 |
| 48 | 0.4838 | 0.50 | 0.50 | 0.4806 | 52 |
| 28 | 0.2032 | 0.25 | 0.75 | 0.6064 | 72 |
| 0 | 0.0000 | 0 | 1 | 0.5543 | 100 |

The surface coverage and the corresponding composition of each thiolate in the resulting gradient were analyzed by applying electrostatic binding of the electroactive compounds. The amine functionalized group on aminoundecane thiol was selected to provide a favorable electrostatic binding site for the negatively charged Fe(II). A neutral thiol, dodecanethiol, was selected as the complementary thiol in the gradient. After printing, the substrates comprising each combination were directly immersed into 1 mM $K_4[Fe(CN)_6]$ for 3 h at pH = 4. The electrostatic binding between the ammonium and the Fe(II) moieties was analyzed by cyclic voltammetry. The amount of Fe(II) was estimated by integration of the charge under the anodic wave according to equation 5.1.

To obtain surface confinement of redox centers binding on a monolayer, they should be located on top of the monolayer or they are well exposed. Figure 5.6 shows the series of cyclic voltammograms of the tailored monolayer composition prepared via pixel–based and droplet–based mixing. The peaks are generated due to one–electron oxidation and reduction of the adsorbed Fe(II). In the cyclic voltammetry, the surface confinement is characterized by symmetric waves with a half width of 3.53RT/nF (90.6 mV at 25 °C) and the current is proportional to the scan rate applied.

In the voltammograms recorded, non–ideal broad waves without well defined peaks formation are observed. The presence of peak broadening as reported are attributed to spatial dispersion of the redox centers (i.e. Fe(II)) which induces lateral interactions between them.[27-30] The presence of a large, closely located Fe(II) redox center are obviously revealed by highest current

density recorded from the pure aminoundecanethiolate probe. In the mixture thiolate probes, the broad peak features are persistent, even though it is expected that the redox centers are well separated. However, the current densities are decreased accordingly pointing to a decrement of the Fe(II) redox centers on the monolayer. Since the Fe(II) redox centers are not covalently attached on the monolayer, they could also permeate into loosely packing domains of the monolayers. Such surface heterogeneities may contribute to the broadening of voltammograms.[31] In addition, it is also found that the currents recorded for each mixture system are linearly proportional to the scan rates supporting the surface confinement of the Fe(II) redox centers. The linearity factors, $R^2$, are presented in Table B.2 and Table B.3 (appendix B).

a b

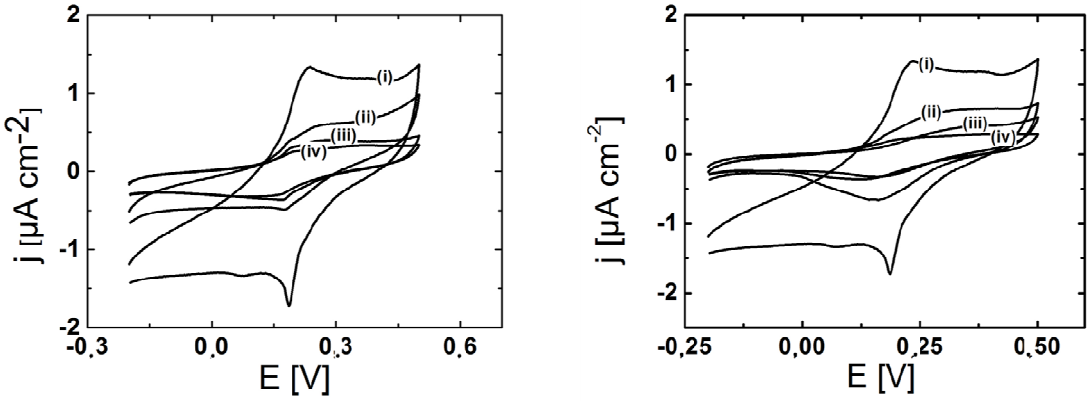


**Figure 5.6** Cyclic Voltammogram series of inkjetted monolayer mixtures prepared by droplet–based (a) and pixel–based (b). Ratios of amino undecanethiol (AUT) dodecanethiol (DDT) in the mixtures are 100:0 (i), 75:25 (ii), 50:50 (iii), and 25:75 (iv). Supporting electrolyte is 0.1 M KCl and scan rate is 20 mV $s^{-1}$.

Figure 5.7 shows the surface coverage obtained from the “tailored gradient” of binary monolayers prepared by droplet–based and pixel–based. The linear change in the plot gives an evidence for the tailored mixing of the two modifiers on the surface assuming selective interaction between Fe(II) and the ammonium terminal groups (Compare also with the calibration from the original EPSON inks (see Table 5.2)). A similar tendency of a gradual changing in the monolayer gradient is also observed from the system of amino undecanethiol and mercaptoundecanoic acid (MUA) which was prepared by the pixel–based approach (see Figure 5.8).

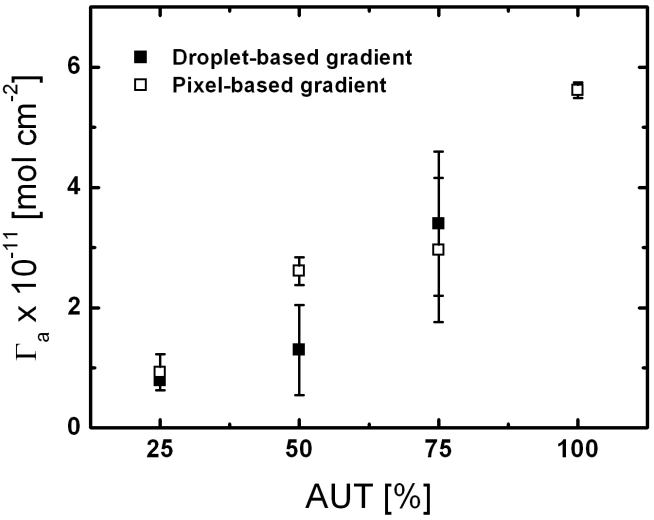


**Figure 5.7** Surface coverages derived by electrostatic interactions of monolayer gradients comprising amino undecanethiol (AUT) and dodecanethiol (DDT). Measurements were conducted in the presence of supporting electrolyte 0.1 M KCl and scan rate is 20 mV $s^{-1}$.Error bars are taken from average of repetitive measurements of each composition.

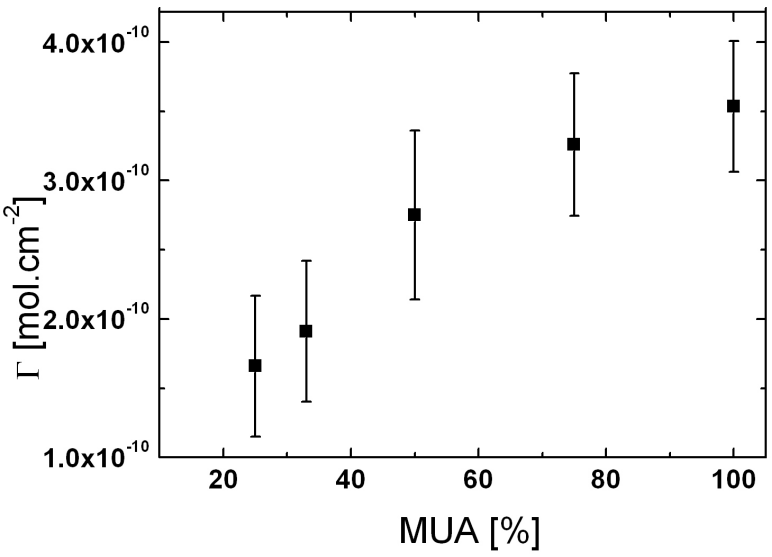


**Figure 5.8** Surface coverages derived by electrostatic interactions of monolayer surfaces comprising tailored amino undecanethiol (AUT) and mercaptopropionic acid (MUA) mixtures prepared by the pixel–based printing approach. Measurements were conducted in the presence of 0.1 M KCl as the supporting electrolyte and scan rate of 20 mV $s^{-1}$.

Variations of the surface coverages affect the steepness of the resulting gradient. From the earlier studies of mixed monolayers prepared by coadsorption, the results revealed that the molar ratios of the thiols in the solution are not necessarily the same as those deposited on the surface (after modification).[32, 33] Some studies show a very short transition from one domain to the other in the gradient.[7, 34, 35] This problem can be resolved if the surface composition depending on the position can be adjusted. In the inkjet printer, the printing system is fully computer controlled, whereby a shooting ordinate can be addressed precisely. The results above have demonstrated the potential of the inkjet printing system in delivering controllable surface composition in the

gradient. The variations in the gradient, especially in the steepness, can be manipulated easily and open many possibilities in the filed of combinatorial chemistry.

## 5.4 Morphology of Tailored Monolayers Mixtures

In preparing a mixture of binary monolayers, it is a challenge to obtain a homogenous binary monolayers coverage. Frequently, phase segregations of two thiols domains in a binary mixture are observed. From numerous studies, it is concluded that the phase segregation (or preferential adsorption) of the thiolates is mainly related to the chain length differences which give a rise to a large energy differences for the different combinations between short and long chain interactions. [25, 33, 36, 37] In coadsorptions, the preferential adsorption of one thiolate in a mixture occurs during the dynamic formation of the SAMs. In the case of sequential absorptions, the phase segregation occurs during the backfilling step (the effect of the exchange reaction was demonstrated in section 5.1).

Segregated phases in binary thiolate mixtures have been reported, starting from several nanometers. Kakiuchi et al.[38, 39] combined cyclic voltammetry and Scanning Tunneling Microscopy (STM) to investigate the morphology of such monolayer mixtures prepared by coadsorption. The data obtained from reductive desorption peaks and the corresponding STM micrographs revealed different degrees in mixture homogenities. Mixtures containing the same chain length show a more homogenous mixing with nanoscale segregated islands than mixtures with a large difference in the chain

length of its constituent.[40, 41] The presence of nanoscale islands was also observed by atomic force microscopy (AFM).[17, 37, 42]

The morphologies of binary mixtures have important implications in two aspects. The first concern is the understanding and the elucidation of the mixing behavior in binary monolayers, and the second is the correlation between nano- or microscale structures with the macroscale properties.

a. MUA : DDT = 25 : 75

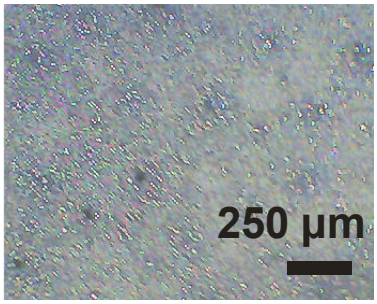


b. MUA : DDT = 50: 50

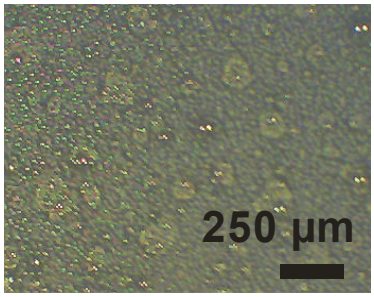


c. MUA : DDT = 75 : 25

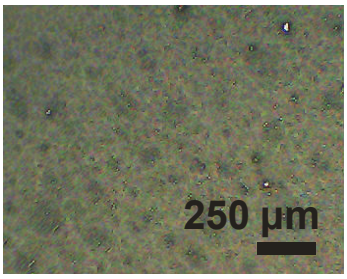


d. MUA : DDT = 50 : 50

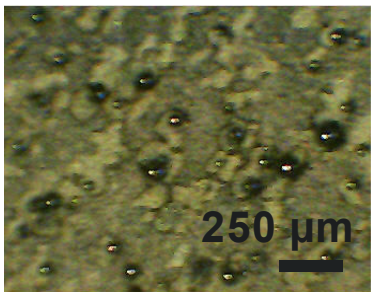


**Figure 5.9** Different combinations of pixel–based monolayer mixtures comprising mercaptoundecane thiol and dodecanthiol (pixel side length of 40 µm). (a) – (c) are inkjetted with glycerol/ethanol = 1:6 (v/v) while (d) is inkjetted with glycerol / ethanol = 1:50 (v/v).

As a morphological study, a mixture of mercapto undecanoic acid and dodecanethiol was prepared by inkjet printing. As described in the previous section, the mixing behaviors of the monolayers prepared by pixel–based and

droplet–based mixing were explored. The carboxylate and the methyl end groups of the thiols provide different surface hydrophobicity. By cooling the substrate using a custom–made Peltier element attached on the optical microscopy system, the mixing behaviors of the monolayer mixtures can be observed from the condensation of water vapor on the surface.

As described previously, the mixture compositions in the pixel–based approach were defined by arranging pixilated squares on a plane surface using Corel Draw X3. The pixels of 40 µm length were chosen because at that size overlapping of the inks (EPSON) spots shot from two channels were observed. It was expected that the thiol inks behave similarly. However, macroscale phase separations, in the order of 100 µm, on the monolayer gradient prepared by pixel–based mixing are evident from Figure 5.9. It also observed that the drop placements do not follow the pixilated patterns of the master, even though the pixel size and the corresponding patterns have been observed using the original EPSON inks on paper. Differences in the ink properties affect the precision of drops depositions. Some smearing is observed as the glycerol to ethanol ratio is decreased by factor ca. 10. However, this is still not sufficient to mix the thiolates (Figure 5.9(d)).

A higher degree of mixing was observed in the thiolate mixtures prepared by droplet–based approach (Figure 5.10). However, it is not proven that the thiolates are fully mixed. Phase segregations in the size or below the limit of the optical resolution can not be observed and Microscopic techniques with higher resolution are required, such as STM or AFM, to solve the possible phase segregations. Unfortunately, the inkjet printer used does not allow for

optimization of droplet formation at the nozzle and the placement of droplets on the substrate. These options are only available on high–end commercial inkjet printers, such as Dimatix.

a. MUA : DDT = 100 : 0

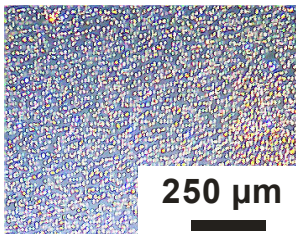


b. MUA : DDT = 50 : 50

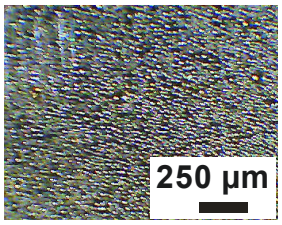


**Figure 5.10** Drop–based monolayer mixture comprising mercaptoundecane thiol and dodecanthiol inkjetted with glycerol /ethanol = 1:6 (v/v).

Another attempt to visualize the mixing behavior of the two thiols, especially those prepared by the drop–based approach, is to couple functionalized fluoro–beads to ω–alkanethiol. Amine- and carboxylate functionalized fluoro beads were chosen to be coupled to the carboxylate- and amine terminated thiols, respectively, via electrostatic interactions and/or amide formation.

Prior to coupling the functionalized beads on the continous mixture of thiols (i.e. the chemical gradient), preliminary experiments were performed to examine the specificity of the bead–to–thiols binding under reaction conditions. A line of 500 µm width of ω–alkanethiols ($NH_2$– and COOH– terminals groups) and the environment comprising neutral alkanethiol (i.e. dodecanethiol) were printed simultaneously. Home–made transparent gold plates were used as substrates

Formation of the bead–thiols linkage was carried out by immersing the printed probes into a bead solution of a certain pH. The electrostatic interactions depend on the pKa of the functional groups and the pH of the solutions. In the first test, 2 mM amino undecanethiol and 2 mM dodecanthiol inks were printed for the line and the background, respectively. The carboxylate functionalized beads solution with particle concentration of 2.65 x $10^{10}$ $ml^{-1}$ were prepared from the stock colloid solution. The pH of the bead solutions were adjusted by phosphate buffer (10 mM). Figure 5.11 shows the optical micrographs of the bead tagged monolayers at pH 5, 7, and 8. At pH 5, an inhomogeneous line is observed where more beads are deposited on the line boundary than on the inner part. At pH 7 and 8, droplets containing the beads are aligned in the center of the lines.

The charges present on the interacting functional groups regulate the electrostatic interactions. The solution pH determines the degree of protonation of amine on the gold|SAM and the carboxylate groups on the beads. The surface $pK_{1/2}$ of aminoundecathiol and carboxylate are approximately 7 and 6, respectively.[43, 44] At a pH close to $pK_{1/2}$ value, approximately half of the functionalized groups will be charged. At pH < $pK_{1/2}$, most of the functionalized groups are protonated, whereas they are deprotonated at pH > $pK_{1/2}$. In all three pHs studied, an attractive electrostatic interaction is expected. However, the micrographs suggest that non–specific interactions play an important role. Beads are also found in the background area (Figure 5.11(d)) which indicates the domination of non–specific interactions. A reverse electrostatic interaction

(i.e. amine groups on the beads and carboxylate groups on the surface) was also performed, but the results were similar.

a

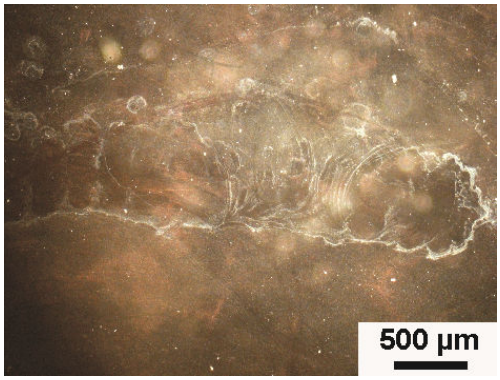


b

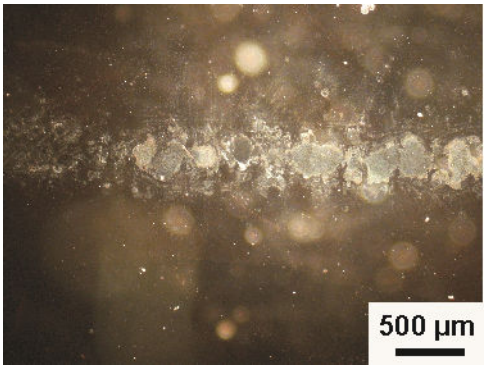


c

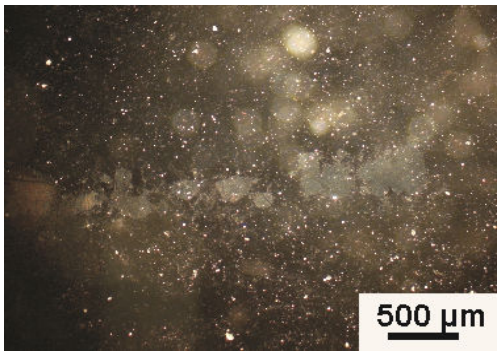


d

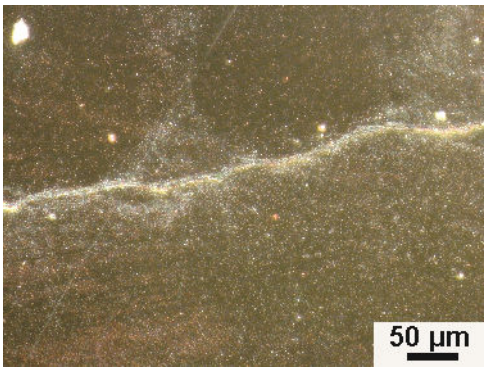


e

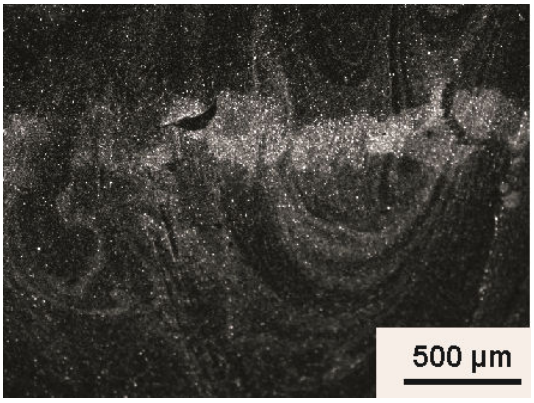


**Figure 5.11** Micrographs of the carboxylate functionalized beads coupled to the amine functionalized monolayers on gold. Panels (a) – (d) show optical micrographs of bead–to–thiols prepared at pH 5 (a) and (d), 7 (b), and 8 (c). Panel (e) shows coupling via amide formation of respective system.

Other factors beside electrostatic interactions may also lead to unexpected behaviors. It has been reported that surface energy differences play a role in the colloid particles adsorption.[45, 46] It is observed that the absorption of functionalized beads are preferentially on hydrophobic surfaces, even though hydrophilic functional groups were available on the perimeter of the particles. Such adsorption behavior points to the domination of hydrophobic nature of polystyrene despite the presence of carboxylate functional groups on the bead surface. In addition, loss of stability in the bead solution may occur upon pH adjustment, which causes agglomeration or precipitation of the beads.

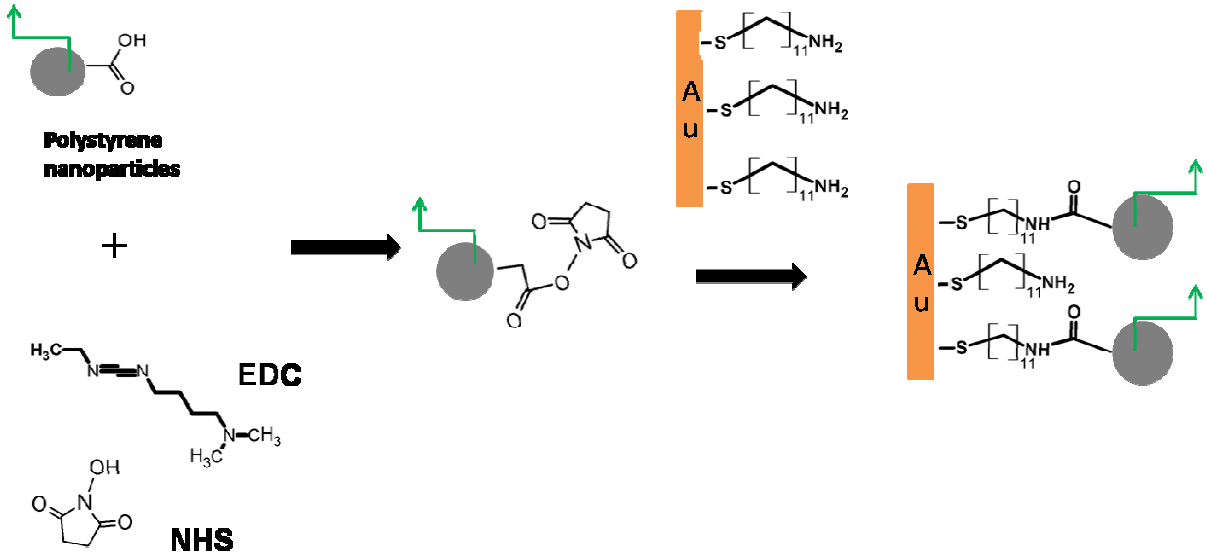


**Figure 5.12** Schematic diagram showing covalent attachment of carboxylate functionalized beads onto amine terminated monolayers via amide formation.

Coupling of the functional beads via amide formation is also described in literatures.[5, 47, 48] This reaction was also applied in the present study. The printed line consists of amino undecanethiol, whereas the background consists of dodecanethiol. The carboxylate functional groups on the beads are covalently

bonded to the carboxylate via the formation of NHS ester groups on the line, according to the reaction below:

From the observations under fluorescence laser microscope, the probes also suffered from non–specific interactions (Figure 5.11(e)). Fluorescence is also observed in the dodecanethiol areas. Coupling via amide formation has been widely used in coupling biomolecules on surfaces. In the amide formation, the presence of the NHS esters on the surface is crucial for successful amide coupling. Therefore, additional surface characterization methods such as FT–IR or XPS is needed in order to optimize the NHS ester formation before the coupling steps.[49, 50]

## 5.5 References

(1) Tidwell, C. D.; Ertel, S. I.; Ratner, B. D.; Tarasevich, B. J.; Atre, S.; Allara, D. L. *Langmuir* **1997**, *13*, 3404-3413.

(2) Smith, J. T.; Kim, D. H.; Reichert, W. M. *Combinatorial Chemistry & High Throughput Screening* **2009**, *12*, 598-603.

(3) Smith, J. T.; Tomfohr, J. K.; Wells, M. C.; Beebe, T. P.; Kepler, T. B.; Reichert, W. M. *Langmuir* **2004**, *20*, 8279-8286.

(4) Liu, L. Y.; Ratner, B. D.; Sage, E. H.; Jiang, S. Y. *Langmuir* **2007**, *23*, 11168-11173.

(5) Plummer, S. T.; Wang, Q.; Bohn, P. W.; Stockton, R.; Schwartz, M. A. *Langmuir* **2003**, *19*, 7528-7536.

(6) Wang, Q.; Bohn, P. W. *Journal of Physical Chemistry B* **2003**, *107*, 12578-12584.

(7) Plummer, S. T.; Bohn, P. W. *Langmuir* **2002**, *18*, 4142-4149.

(8) Strutwolf, J.; O'Sullivan, C. K. *Electroanalysis* **2007**, *19*, 1467-1475.

(9) Ballav, N.; Shaporenko, A.; Terfort, A.; Zharnikov, M. *Advanced Materials* **2007**, *19*, 998-1000.

(10) Burgos, P.; Geoghegan, M.; Leggett, G. J. *Nano Letters* **2007**, *7*, 3747-3752.

(11) Fuierer, R. R.; Carroll, R. L.; Feldheim, D. L.; Gorman, C. B. *Advanced Materials* **2002**, *14*, 154-157.

(12) Collard, D. M.; Fox, M. A. *Langmuir* **1991**, *7*, 1192-1197.

(13) Riepl, M.; Ostblom, M.; Lundstrom, I.; Svensson, S. C. T.; van der Gon, A. W. D.; Schaferling, M.; Liedberg, B. *Langmuir* **2005**, *21*, 1042-1050.

(14) Lestelius, M.; Engquist, I.; Tengvall, P.; Chaudhury, M. K.; Liedberg, B. *Colloids and Surfaces B-Biointerfaces* **1999**, *15*, 57-70.

(15) Frederix, F.; Bonroy, K.; Laureyn, W.; Reekmans, G.; Campitelli, A.; Dehaen, W.; Maes, G. *Langmuir* **2003**, *19*, 4351-4357.

(16) Chambers, R. C.; Inman, C. E.; Hutchison, J. E. *Langmuir* **2005**, *21*, 4615-4621.

(17) Morgenthaler, S. M.; Lee, S.; Spencer, N. D. *Langmuir* **2006**, *22*, 2706-2711.

(18) Morgenthaler, S.; Lee, S. W.; Zurcher, S.; Spencer, N. D. *Langmuir* **2003**, *19*, 10459-10462.

(19) Kraus, T.; Stutz, R.; Balmer, T. E.; Schmid, H.; Malaquin, L.; Spencer, N. D.; Wolf, H. *Langmuir* **2005**, *21*, 7796-7804.

(20) Sankhe, A. Y.; Booth, B. D.; Wiker, N. J.; Kilbey, S. M. *Langmuir* **2005**, *21*, 5332-5336.

(21) Chidsey, C. E. D.; Bertozzi, C. R.; Putvinski, T. M.; Mujsce, A. M. *Journal of the American Chemical Society* **1990**, *112*, 4301-4306.

(22) Rowe, G. K.; Creager, S. E. *Langmuir* **1991**, *7*, 2307-2312.

(23) Lee, L. Y. S.; Lennox, R. B. *Physical Chemistry Chemical Physics* **2007**, *9*, 1013-1020.

(24) Allara, D. L.; Nuzzo, R. G. *Langmuir* **1985**, *1*, 45-52.

(25) Bain, C. D.; Evall, J.; Whitesides, G. M. *Journal of the American Chemical Society* **1989**, *111*, 7155-7164.

(26) Laczka, O.; Ferraz, R. M.; Ferrer-Miralles, N.; Villaverde, A.; Munoz, F. X.; del Campo, F. J. *Analytica Chimica Acta* **2009**, *641*, 1-6.

(27) Laviron, E. *Journal of Electroanalytical Chemistry* **1974**, *52*, 395-402.

(28) Matsuda, H.; Aoki, K.; Tokuda, K. *Journal of Electroanalytical Chemistry* **1987**, *217*, 15-32.

(29) Angersteinkozlowska, H.; Klinger, J.; Conway, B. E. *Journal of Electroanalytical Chemistry* **1977**, *75*, 45-60.

(30) Calvente, J. J.; Andreu, R.; Molero, M.; Lopez-Perez, G.; Dominguez, M. *Journal of Physical Chemistry B* **2001**, *105*, 9557-9568.

(31) Benitez, G.; Vericat, C.; Tanco, S.; Lenicov, F. R.; Castez, M. F.; Vela, A. E.; Salvarezza, R. C. *Langmuir* **2004**, *20*, 5030-5037.

(32) Folkers, J. P.; Laibinis, P. E.; Whitesides, G. M.; Deutch, J. *Journal of Physical Chemistry* **1994**, *98*, 563-571.

(33) Folkers, J. P.; Laibinis, P. E.; Whitesides, G. M. *Langmuir* **1992**, *8*, 1330-1341.

(34) Ballav, N.; Shaporenko, A.; Krakert, S.; Terfort, A.; Zharnikov, M. *Journal of Physical Chemistry C* **2007**, *111*, 7772-7782.

(35) Liedberg, B.; Tengvall, P. *Langmuir* **1995**, *11*, 3821-3827.

(36) Kang, J. F.; Ulman, A.; Liao, S.; Jordan, R. *Langmuir* **1999**, *15*, 2095-2098.

(37) Mizutani, W.; Ishida, T.; Yamamoto, S. I.; Tokumoto, H.; Hokari, H.; Azehara, H.; Fujihira, M. *Applied Physics A* **1998**, *66*, S1257-S1260.

(38) Hobara, D.; Ota, M.; Imabayashi, S.; Niki, K.; Kakiuchi, T. *Journal of Electroanalytical Chemistry* **1998**, *444*, 113-119.

(39) Kakiuchi, T.; Iida, M.; Gon, N.; Hobara, D.; Imabayashi, S.; Niki, K. *Langmuir* **2001**, *17*, 1599-1603.

(40) Stranick, S. J.; Atre, S. V.; Parikh, A. N.; Wood, M. C.; Allara, D. L.; Winograd, N.; Weiss, P. S. *Nanotechnology* **1996**, *7*, 438-442.

(41) Stranick, S. J.; Parikh, A. N.; Tao, Y. T.; Allara, D. L.; Weiss, P. S. *Journal of Physical Chemistry* **1994**, *98*, 7636-7646.

(42) Tamada, K.; Hara, M.; Sasabe, H.; Knoll, W. *Langmuir* **1997**, *13*, 1558-1566.

(43) Degefa, T. H.; Schon, P.; Bongard, D.; Walder, L. *Journal of Electroanalytical Chemistry* **2004**, *574*, 49-62.

(44) Bhat, R. R.; Genzer, J. *Nanotechnology* **2007**, *18*.

(45) Fan, H. Y.; Lopez, G. P. *Langmuir* **1997**, *13*, 119-121.

(46) Grabar, K. C.; Smith, P. C.; Musick, M. D.; Davis, J. A.; Walter, D. G.; Jackson, M. A.; Guthrie, A. P.; Natan, M. J. *Journal of the American Chemical Society* **1996**, *118*, 1148-1153.

(47) Shuster, M. J.; Vaish, A.; Szapacs, M. E.; Anderson, M. E.; Weiss, P. S.; Andrews, A. M. *Advanced Materials* **2008**, *20*, 164-167.

(48) Mena, M. L.; Carralero, V.; Gonzalez-Cortes, A.; Yanez-Sedeno, P.; Pingarron, J. M. *Electroanalysis* **2005**, *17*, 2147-2155.

(49) Mougin, K.; Lawrence, M. B.; Fernandez, E. J.; Hillier, A. C. *Langmuir* **2004**, *20*, 4302-4305.

(50) Frey, B. L.; Corn, R. M. *Analytical Chemistry* **1996**, *68*, 3187-3193.

# Chapter 6: Deposition of $CeO_2$ onto Mesoporous Antimony Tin Oxide (ATO) Thin Film by Inkjet Printing

The delivery of cerium dioxide ($CeO_2$) nanocrystals from a precursor solution onto mesoporous antimony tin oxide by inkjet printing technique is described. The deposited mass characterized by quartz microbalance was detected by a frequency shift and follows the Saeurbrey principle. The correlation between $CeO_2$ deposited on the mesoporous system and the changing of porosity is investigated.

## 6.1 $CeO_2$ mixed Thin Oxide Films

Cerium dioxide ($CeO_2$) thin films have been widely investigated and are well known in electrochromic devices as counter electrodes. The ultimate features of $CeO_2$ thin films include maintaining high transmittance characteristic during ion intercalation, high charge storage capacity, and good electrochemical reversibility. However, the kinetics of the ion intercalation in pure $CeO_2$ thin films have been observed to be slower than in the $CeO_2$ mixed with other thin oxide films, such as $TiO_2$, $SiO_2$, $V_2O_5$, $SnO_2$ etc.[1-6] Boudry et al.[1] found the insertion charge of 9.1 mC $cm^{-2}$ with transmittance of 70% from $CeO_2$–$TiO_2$ mixed oxide film which is produced by sol gel method. Keomany et al.[7] reported that the best compositions of $CeO_2$ in $TiO_2$ matrix for application of smart window are in

the range of 25% to 50%. The ion insertion is in the order of two magnitudes higher than in the $CeO_2$ thin film alone.

In this study, $CeO_2$ nanocrystals were delivered onto mesoporous thin film via inkjet printing. As a model for the mesoporous system, mesoporous ATO thin films are used. ATO is an n–type semiconductor with the band gap of 3.3 eV and is particularly interesting for optoelectronics–related applications.[8-10] Coleman et al.[11, 12] applied ATO as an electrochromic material. ATO circuitry was also prepared by using screen printing technique for printed displays. The precursor solution of $CeO_2$ was put into the ink reservoir. Afterwards, cycles of printing–drying–firing were performed repeatedly. The corresponding deposited mass of $CeO_2$ nanocrystals formed after firing was measured by the Quartz Crystal Microbalance (QCM) method.

The common preparation techniques of mixing $CeO_2$ with other oxide materials include sol–gel[7, 13], radio frequency sputtering[14], and Pechini method[6]. These techniques require much effort, for example, to prepare a stable sol and also to obtain homogenous coating. To prepare $CeO_2$ nanocrystals located on the top of a mesoporous oxide thin film would be troublesome in these techniques whereas in the inkjet printing technique this would not be the case. Another advantage of using inkjet printing technique is that the dosage of $CeO_2$ added to a mesoporous thin film can be controlled or adjusted.

The work is focused on the sensitivity of the QCM to detect addition of the nanoparticles, the amount of the inkjetted nanoparticles depending on the

printing cycles, and the stability of the porous networks after nanoparticles depostion.

## 6.2 QCM Measurements on Inkjetted $CeO_2$ Precursor Solution

In QCM method, a quartz crystal substrate is placed between two metals electrodes. An electric field introduced across the crystal causes vibration motions at the crystals' resonant frequency. The mass change ($\Delta m$) on the crystals is detected by the QCM in the frequency shift ($\Delta f_m$) which is expressed in the Sauerbrey equation, as follows:[15]

$$\Delta f_m = -c_l \Delta m \tag{6.1}$$

where $c_l$ is the sensitivity factor.

The application of the Sauerbrey equation for the mesoporous system in liquids has been developed by our group.[16] The QCM measurements under liquid exposure provided additional advantages, such as in–situ observation of ion insertions.[17] In the mesoporous systems, the frequency shift ($\Delta f_T$) is proportional to the areal density of the mesoporous system after firing ($\Delta m_T$). $\Delta m_T$ is also equal to the film thickness of the mesoporous film ($d_T$) multiplied with its macroscopic volumetric density ($\rho_m$), as expressed in equation 6.2 and 6.3.

$$\Delta m_T = -\left(\frac{\Delta f_T}{c_l}\right) = d_T \rho_m \tag{6.2}$$

where

$$\Delta f_T = f_T - f_0 \tag{6.3}$$

and $$d_T = -\frac{\Delta f_T 100}{c_l \rho_T (100 - P)} \quad (6.4)$$

$f_T$ and $f_0$ denote the frequencies of the quartz crystal before and after mesoporous deposition, respectively, in the dry state. P and $\rho_T$ are porosity and mean density of the mesoporous nanocrystal of the mesoporous films, respectively.

Since the mesoporous nanocrystal structures are relatively stabile under certain solvents exposure, a frequency shift is expected in the Sauerbrey–like phenomena due to increasing surface area. Furthermore, the liquid entering the mesoporous film also contributes to the mass changes inside the system. The corresponding frequency shift is expressed in equation 6.5 – 6.7 below. Equation 6.7 is obtained by substituting equation 6.5 with equation 6.4

$$\Delta f = f_l - f_T = -c_1 \left( c_2 \left( \rho_l \eta_l \right) \right)^{1/2} + h\rho_l + \left( \frac{P}{100} \right) d_T \rho_l \quad (6.5)$$

where $$\Delta f_l = f_l - f_T = -c_1 \left( c_2 \left( \rho_l \eta_l \right)^{1/2} + h\rho_l \right) + c_3 \rho_l \Delta f_T \quad (6.6)$$

and $$c_3 = P / \rho_T (100 - P) \quad (6.7)$$

$f_l$ is the frequency read out under liquid exposure while $c_1$ and $c_2$ are the sensitivity factors related to the properties of the liquid. $\rho_l$ and $\eta_l$ are density and viscosity of the liquids while h is mesoporous film thickness.

In this study, three ATO modified crystals with different thicknesses were investigated. The thicknesses of the probes were estimated from the

frequency shifts ($\Delta f_T$) read out in the measurements under Ar gas, whereby the film thicknesses are linearly proportional to $\Delta f_T$ (see equation 6.2 and 6.4).

a b

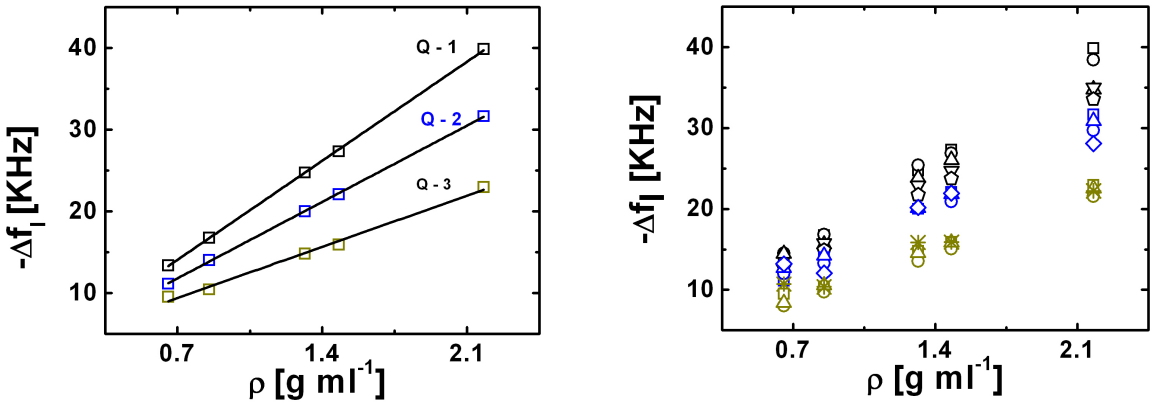


**Figure 6.1** Resonant frequency shift of 6 MHz of ATO- (a) and ATO / n$CeO_2$ modified quartz crystals (b). Numbers of printing–firing cycles (n) follow the order of: □ = 0, ○ = 2, Δ = 4, ∇ = 6,◊ = 8,∗ = 10, and ⌂ = 12. Solvents used are: n-hexane (ρ= 0.6547 $gml^{-1}$), toluene (ρ= 0,8525 $gml^{-1}$), dicholoromethane (ρ= 1.316 g $ml^{-1}$), chloroform (ρ= 1.480 g $ml^{-1}$), and 1,2-dibromomethane (ρ= 2.182 g $ml^{-1}$).

The relationship between $-\Delta f_l$ and $\rho_l$ on the mesoporous ATO modified quartz crystals, according to equation 6.5, is depicted in Figure 6.1(a). The linear relationship discovered in the systems investigated suggests that the first term and the second term of equation 6.5 are less dominant. The first and the second terms refer to the effect of viscous entrainment of the liquids[18] and the liquid trapped in the pores[19], respectively. The linearity is more pronounced on the thicker mesoporous film (Q – 1). The tendency is similar to the mesoporous $TiO_2$ modified quartz crystals reported by our group.[16]

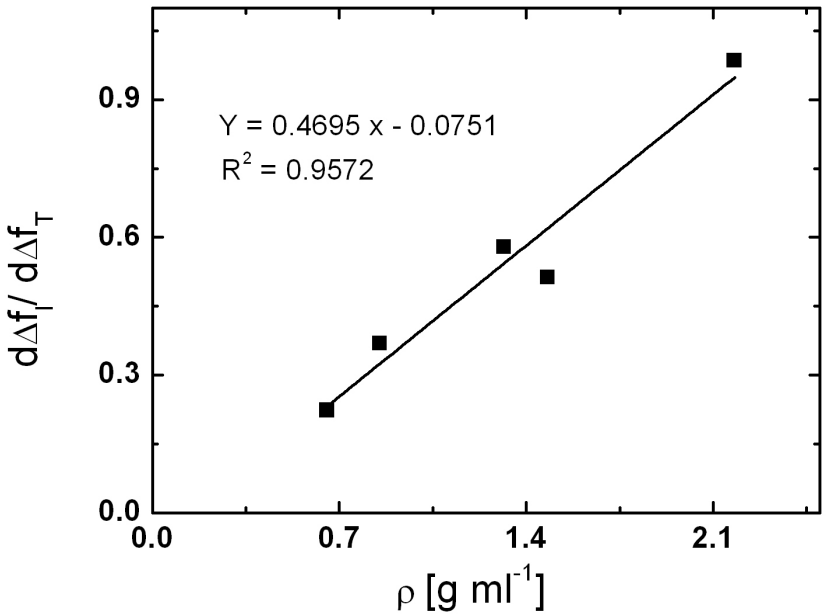


**Figure 6.2** Plot of $d\Delta f_l/d\Delta f_T$ against $\rho_l$ of exposed solvents.

The mass additions of $CeO_2$ nanoparticles after printing–firing cycles (n) which fills the porous networks of ATO nanoparticles are indicated by the shiftings of $\Delta f_l$ (see Figure 6.1 (b)). The frequency shiftings between the printing cycles are more obviously seen in the thicker mesoporous film (i.e. Q – 1, d = 2.5 μm) than in the thinner mesoporous film (i.e. Q – 3, d = 1.1 μm). The overlapping frequency shifts upon $CeO_2$ deposition cycles could be attributed to the contributions of the transversal share wave region developped on the mesoporous surface which is more pronounced in the thin mesoporous film[16] and also to the pore clogging that may limit the mass additions.

Since a linear relationship is found on $-\Delta f_l$ vs $\rho_l$, the contributions of surface phenomena (i.e. the first and second terms in eq. 6.5 and 6.6) can be neglected by doing differentiation of $d\Delta f_l/d\Delta f_T$, as shown below:

$$\frac{d\Delta f_l}{d\Delta f_T} = c_3 \rho_l \tag{6.8}$$

The percentage of porosity of mesoporous ATO modified crystal quartz can be derived from the slope's plot of $d\Delta f_l / d\Delta f_T$ against $\rho_l$. Following equation 6.7 with $\rho_T$ is 6.85 g $cm^{-3}$ yields a porosity of ATO of 76.28%. The changes in porosity upon additions of $CeO_2$ inkjetting cycle are estimated by the slope ratios which are plotted in Figure 6.3. The result suggests that the porosity reaches maximum of 60% after 12 applications of the inkjet–firing cycles.

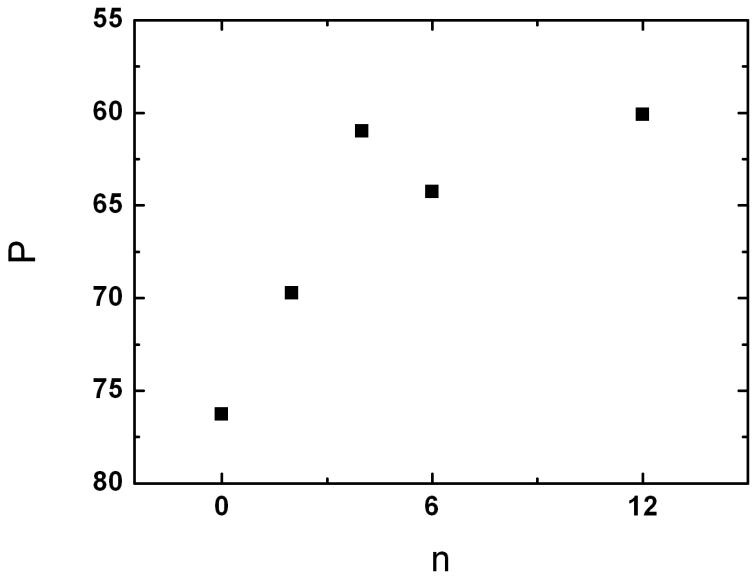


**Figure 6.3** Change in porosities of mesoporous film upon $CeO_2$ inkjet cycles.

The morphology of ATO and ATO/n$CeO_2$ was observed by Scanning Electron Microscopy (SEM). However, the change of porosity upon addition of $CeO_2$ can not be resolved from the micrographs (see Figure 6.4 and Figure C.1 – C.3 in Appendix C) quantitatively. The quantitative analysis of porosity

changes can be obtained by performing statistical simulation as reported by Braginsky et al.[20]

a b

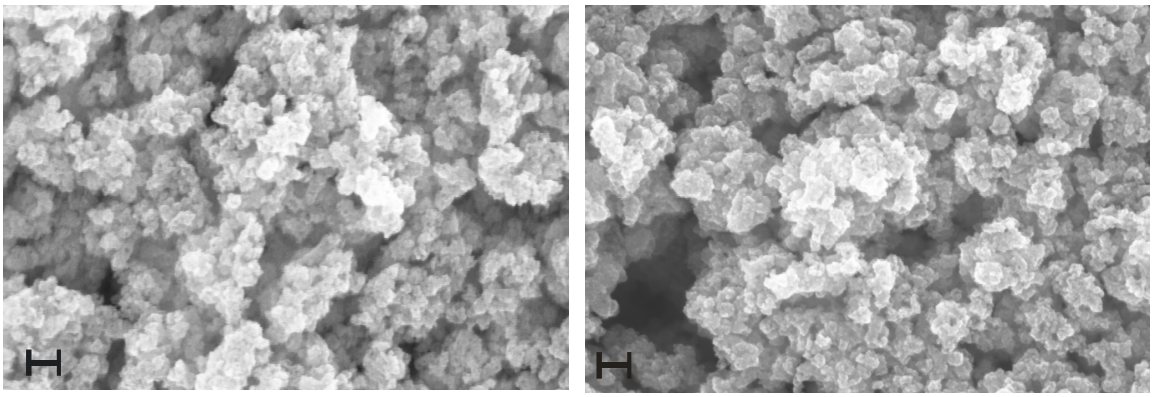

c

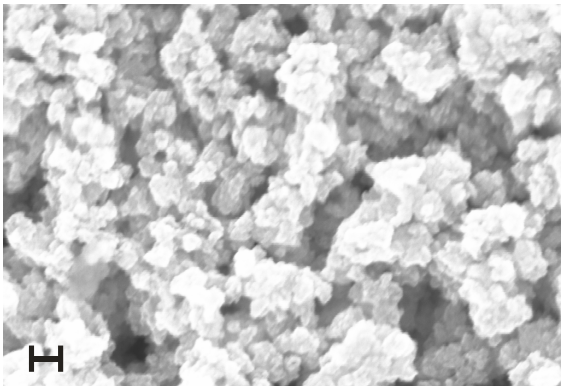

**Figure 6.4** SEM micrographs of (a) ATO, (b) ATO/4$CeO_2$ and (c) ATO/12 $CeO_2$. Bars indicate for 100 nm.

## 6.3 References

(1) Baudry, P.; Rodrigues, A. C. M.; Aegerter, M. A.; Bulhoes, L. O. *Journal of Non-Crystalline Solids* **1990**, 319-322.

(2) Zhu, B.; Liu, Z. G.; Xia, C. R. *Materials Research Bulletin* **1999**, *34*, 1507-1512.

(3) Picardi, G.; Varsano, F.; Decker, F.; Opara-Krasovec, U.; Surca, A.; Orel, B. *Electrochimica Acta* **1999**, *44*, 3157-3164.

(4) Ghodsi, F. E.; Tepehan, F. Z.; Tepehan, G. G. *Electrochimica Acta* **1999**, *44*, 3127-3136.

(5) Zhu, B.; Xia, C. R.; Luo, X. G.; Niklasson, G. *Thin Solid Films* **2001**, *385*, 209-214.

(6) Rosario, A. V.; Pereira, E. C. *Thin Solid Films* **2002**, *410*, 1-7.

(7) Keomany, D.; Petit, J. P.; Deroo, D. *Solar Energy Materials and Solar Cells* **1995**, *36*, 397-408.

(8) Dawar, A. L.; Joshi, J. C. *Journal of Materials Science* **1984**, *19*, 1-23.

(9) Wang, Y. D.; Brezesinski, T.; Antonietti, M.; Smarsly, B. *Acs Nano* **2009**, *3*, 1373-1378.

(10) Marcel, C.; Hegde, M. S.; Rougier, A.; Maugy, C.; Guery, C.; Tarascon, J. M. *Electrochimica Acta* **2001**, *46*, 2097-2104.

(11) Coleman, J. P.; Lynch, A. T.; Madhukar, P.; Wagenknecht, J. H. *Solar Energy Materials and Solar Cells* **1999**, *56*, 375-394.

(12) Coleman, J. P.; Lynch, A. T.; Madhukar, P.; Wagenknecht, J. H. *Solar Energy Materials and Solar Cells* **1999**, *56*, 395-418.

(13) Cuentas-Gallegos, A. K.; Rincon, M. E.; Orozco-Gamboa, G. *Electrochimica Acta* **2006**, *51*, 3794-3801.

(14) Masetti, E.; Varsano, F.; Decker, F. *Electrochimica Acta* **1999**, *44*, 3117-3119.

(15) Buttry, D. A.; Ward, M. D. *Chemical Reviews* **1992**, *92*, 1355-1379.

(16) Schon, P.; Michalek, R.; Walder, L. *Analytical Chemistry* **1999**, *71*, 3305-3310.

(17) McKenzie, K. J.; Marken, F.; Gao, X.; Tsang, S. C.; Tam, K. Y. *Electrochemistry Communications* **2003**, *5*, 286-291.

(18) Kanazawa, K. K.; Gordon, J. G. *Analytical Chemistry* **1985**, *57*, 1770-1771.

(19) Schumacher, R.; Borges, G.; Kanazawa, K. K. *Surface Science* **1985**, *163*, L621-L626.

(20) Braginsky, L.; Shklover, V.; Witz, G.; Bossmann, H. P. *Physical Review B* **2007**, *75*.

# Summary

Inkjet printing has been recognized as an effective and straightforward way to prepare homogenous and/or laterally structured thin film. In this work, the inkjet printing technique is used to deposit thiolate monolayers on gold surfaces and $CeO_2$ nanoparticles on ATO mesoporous thin films. It is chosen as an alternative technique to those commonly used, such as immersion and μCP techniques. Mechanical modifications of the inkjet printer used, ink formulation, and calibrations of the mass deposited were performed. Several highlighted phenomena done in this work studied and achieved are summarized as follows:

i. The insulating property of hexadecanthiolates prepared by inkjet printing is comparable to that prepared by immersion of gold substrates in the thiol solution. The overlapping inkjetted droplets containing thiolates might *self heal* some possible defects and lead to improvements of the total insulating quality of the monolayers.

ii. An interesting phenomenon of inkjetting thiol droplets is that the monolayer does not form a ring–like deposit, whereas a ring–like deposit of glycerol, the co–solvent constituent in the ink, was observed after complete ethanol evaporation. This result suggests that as soon as a droplet impacts a gold surface, the monolayers are formed very fast, so that their depositions are not affected by the solvents evaporation. Another explanation could be that convective Marangoni flows plays role in bringing the thiolates to the innerpart of the droplet.

iii. Random microelectrodes array with diameter of 40 μm can be easily prepared by the inkjet printing using the color density adjustment in graphical program. The electrochemical behavior of the random microelectrode was studied by cyclic voltammetry. A transition of the electrochemical responses from micro- to macroelectrodes was observed. The random microelectrode array could be useful for further modifications related to the study of interfacial phenomena.

iv. The simultaneous printing of two thiols in form of lines with width of 500 μm and the environment was demonstrated. The result shows that linear structures can be prepared by inkjet printing efficiently on non absorbing surfaces, i.e. gold surfaces. Band electrodes (300 μm wide and 1 cm long) can be prepared by printing two different thiols from different channels simultaneously. The electrochemical transition of micro- to macroelectrode behaviors was observed for the printed band electrodes with widths of 300 μm to 1 mm.

v. Benefitting from the multiple channels available at the printhead, the preparation of mixed thiolates on gold was studied. The results revealed that mixed thiols prepared by the printing–backfilling method are prone to highly exchange reactions. In contrast, printing by using two channels opens a possibility to create a gradual mixture of the two thiols, even though phase separation is observed. The morphological study of the mixed thiols using functionalized beads showed negative results. The beads are unfortunately prone to unspecific interactions.

vi. Another study carried out in this work is the inkjet printing of a homogenous layer, i.e. using the inkjet printer as a nanodispenser. Herein, a solution of $CeO_2$ was inkjetted repeatedly on ATO thin films. The deposited mass and the corresponding porosity changes were recorded. The QCM measurements demonstrate the stability of the nanocrystals embedded mesoporous thin film.

# Appendix A

(i) (ii)

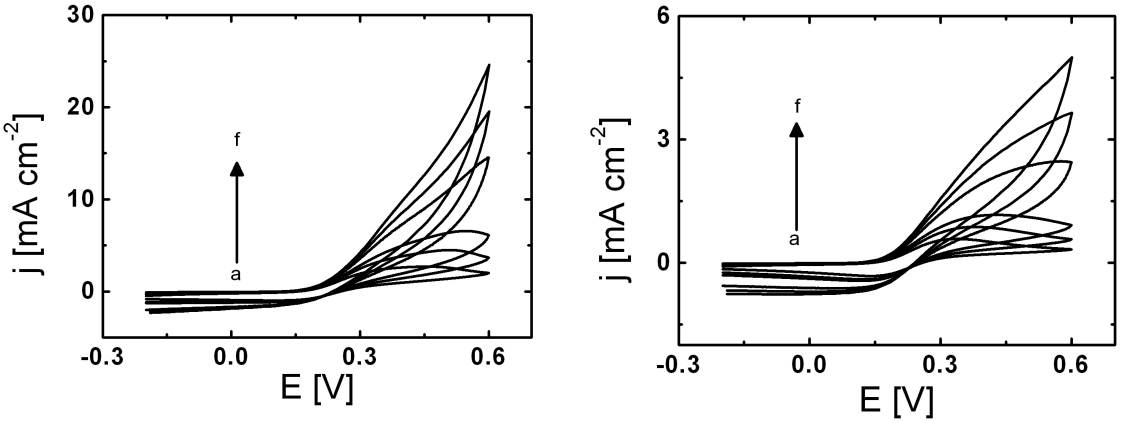


**Figure A.1** Cyclic voltammograms of 1 mM ferrocenylethanol in 0.1 M KCl at HS-$(CH_2)_2$-COOH random array microdisk electrodes printed at 1% (i) and 4% color (ii) intensities. The applied scan rates are (a) 20 mV $s^{-1}$, (b) 50 mV $s^{-1}$, (c) 100 mV $s^{-1}$, (d) 500 mV $s^{-1}$, (e) 1000 mV $s^{-1}$, and (f) 2000 mV $s^{-1}$.

# Appendix B

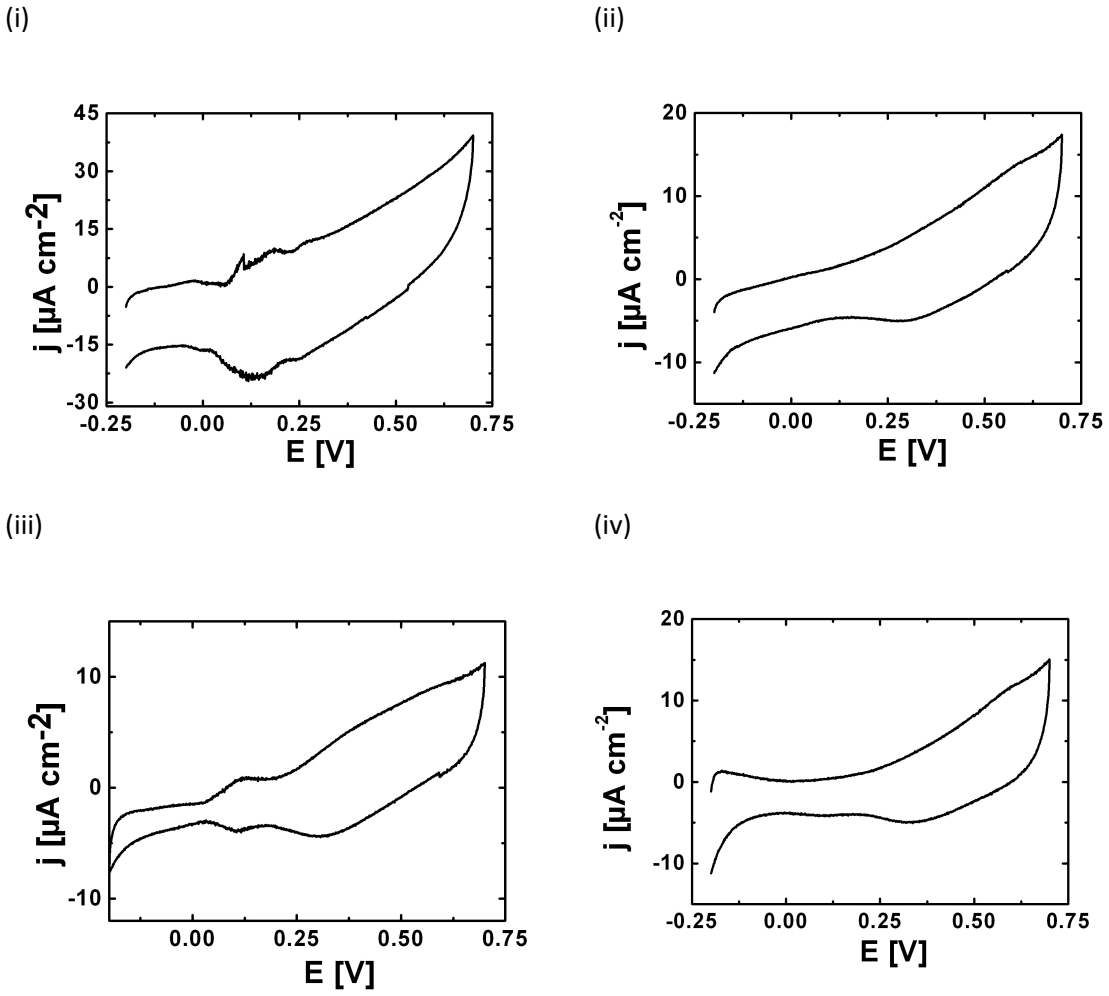


**Figure B.1** Cyclic voltammograms of inkjetted ferrocenylhexanthiol inkjetted from yellow channel at 50% (i), 30% (ii), 10% (iii), and 1% (iv) color intensities which are backfilled with 1 mM Butanethiol. Supporting electrolyte is 1 M $HClO_4$ and scan rate is 100 mV $s^{-1}$.

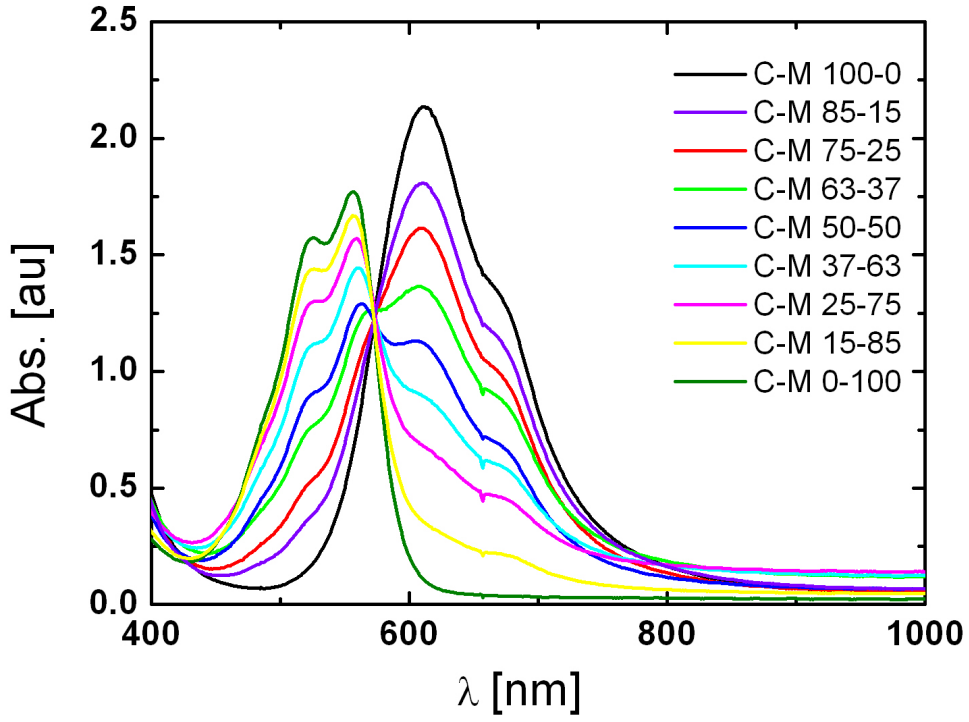


**Figure B.2** Complete spectra of pixel–based mixtures recorded from the original EPSON inks.

**Table B.1** Surface compositions results from Magenta and Cyan channels in the droplet–based mixtures.

| Magenta,M [%] | $A_D$ [au] | $A_L$ [au] | $\Gamma_D 10^{-9}$ [mol cm$^{-2}$] | $\Gamma_L 10^{-9}$ [mol cm$^{-2}$] | $\Gamma_{total}$ [mol cm$^{-2}$] | x M | x C | $\Gamma_{total}$ [mol cm$^{-2}$] | $\Gamma_L$ [mol cm$^{-2}$] | $\Gamma_D$ [mol cm$^{-2}$] | $A_L$ [au] | $A_D$ [au] | Cyan , C [%] |
|---|---|---|---|---|---|---|---|---|---|---|---|---|---|
| 100 | 1.5379 | 0.0877 | 0.7040 | 0.0397 | 0.7437 | 1.00 | 0.00 | 0 | 0 | 0 | 0 | 0 | 0 |
| | 1.4585 | 0.0851 | 0.7053 | 0.0385 | 0.7438 | 1.00 | 0.00 | 0 | 0 | 0 | 0 | 0 | 0 |
| | 1.5291 | 0.0846 | 0.7038 | 0.0383 | 0.7421 | 1.00 | 0.00 | 0 | 0 | 0 | 0 | 0 | 0 |
| 64 | 0.1518 | 1.4351 | 0.0687 | 0.6490 | 0.7176 | 0.76 | 0.24 | 0.2288 | 0.2288 | 0 | 0.8425 | 0 | 36 |
| | 0.1504 | 1.4505 | 0.0680 | 0.6560 | 0.7240 | 0.76 | 0.24 | 0.2294 | 0.2294 | 0 | 0.8448 | 0 | |
| | 0.1469 | 1.4501 | 0.0664 | 0.6558 | 0.7222 | 0.76 | 0.24 | 0.2291 | 0.2291 | 0 | 0.8434 | 0 | |
| 48 | 0 | 1.0749 | 0 | 0.4861 | 0.4861 | 0.50 | 0.50 | 0.4818 | 0.4818 | 0 | 1.7740 | 0 | 52 |
| | 0 | 1.0748 | 0 | 0.4860 | 0.4860 | 0.50 | 0.50 | 0.4814 | 0.4814 | 0 | 1.7727 | 0 | |
| | 0 | 1.0600 | 0 | 0.4794 | 0.4794 | 0.50 | 0.50 | 0.4784 | 0.4784 | 0 | 1.7616 | 0 | |
| 28 | 0 | 0.4546 | 0 | 0.2056 | 0.2056 | 0.25 | 0.75 | 0.6084 | 0.4994 | 0.1091 | 1.8387 | 0.4016 | 72 |
| | 0 | 0.4520 | 0 | 0.2044 | 0.2044 | 0.25 | 0.75 | 0.6028 | 0.4941 | 0.1088 | 1.8191 | 0.4005 | |
| | 0 | 0.4412 | 0 | 0.1995 | 0.1995 | 0.25 | 0.75 | 0.6078 | 0.4978 | 0.1100 | 1.8328 | 0.4052 | |
| 0 | 0 | 0 | 0 | 0 | 0 | 0.00 | 1.00 | 0.5546 | 0.0046 | 0.5501 | 0.0169 | 2.0154 | 100 |
| | 0 | 0 | 0 | 0 | 0 | 0.00 | 1.00 | 0.5555 | 0.0049 | 0.5506 | 0.0179 | 2.0273 | |
| | 0 | 0 | 0 | 0 | 0 | 0 | 1.00 | 0.5527 | 0.0053 | 0.5474 | 0.0197 | 2.0253 | |

**Table B.2** Cyclic Voltammogram series of the inkjetted monolayer mixtures prepared by pixel–based mixtures. Supporting electrolyte is 0.1 M KCl.

| 20 mVs-1 | 50 mVs-1 | 100 mVs-1 | $R^2$ |
|---|---|---|---|
| AUT : DDT = 100 : 0 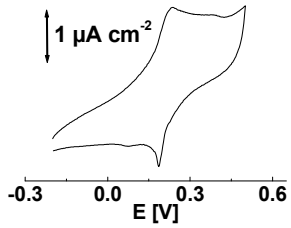  | AUT : DDT = 100 : 0 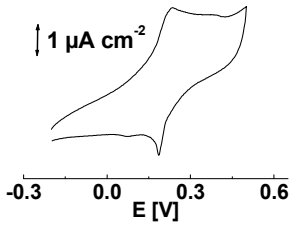  | AUT : DDT = 100 : 0 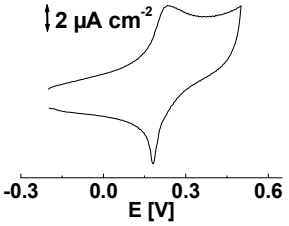  | 0.9959 |
| AUT : DDT = 75 : 25 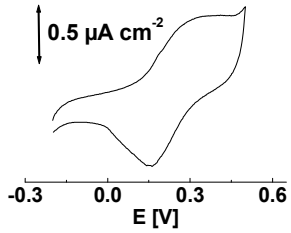  | AUT : DDT = 75 : 25 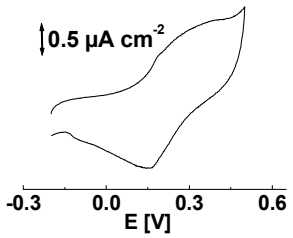  | AUT : DDT = 75 : 25 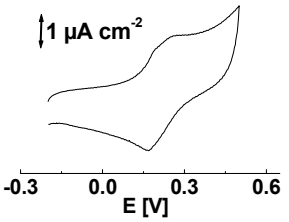  | 0.9285 |
| AUT : DDT = 50 : 50 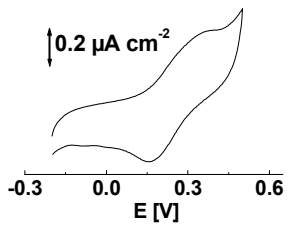  | AUT : DDT = 50 : 50 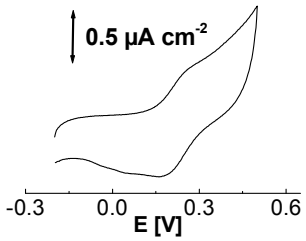  | AUT : DDT = 50 : 50 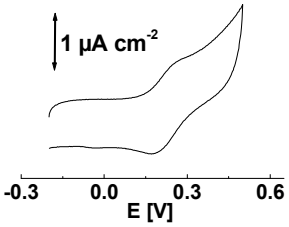  | 0.7244 |
| AUT : DDT = 25 : 75 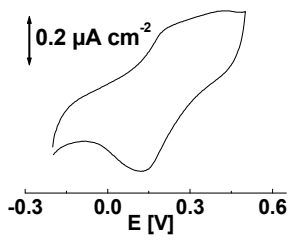  | AUT : DDT = 25 : 75 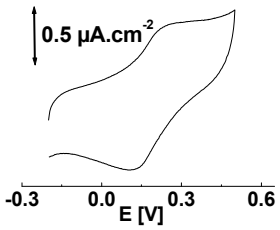  | AUT : DDT = 25 : 75 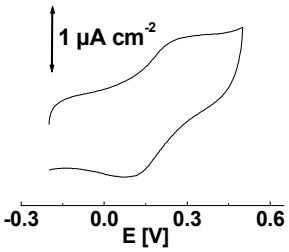  | 0.9675 |

**Table B.3** Cyclic Voltammogram series of the inkjetted monolayer mixtures prepared by droplet–based mixtures. Supporting electrolyte is 0.1 M KCl.

| 20 mVs-1 | 50 mVs-1 | 100 mVs-1 | $R^2$ |
|---|---|---|---|
| AUT : DDT = 100 : 0 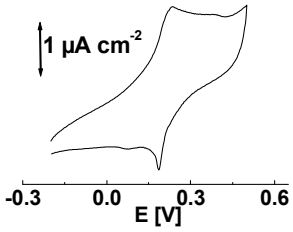  | AUT : DDT = 100 : 0 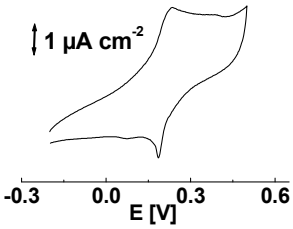  | AUT : DDT = 100 : 0 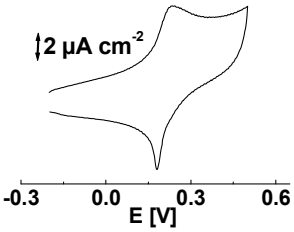  | 0.9959 |
| AUT : DDT = 75 : 25 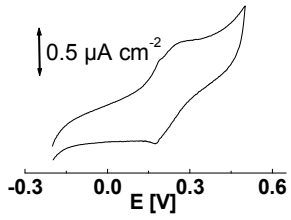  | AUT : DDT = 75 : 25 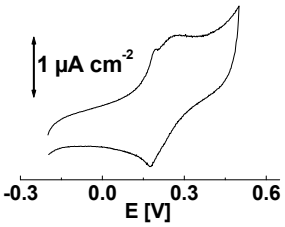  | AUT : DDT = 75 : 25 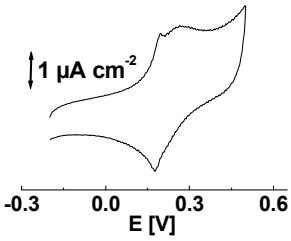  | 0.9998 |
| AUT : DDT = 50 : 50 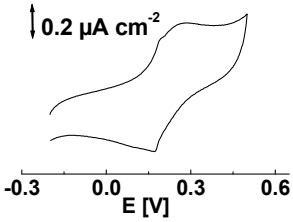  | AUT : DDT = 50 : 50 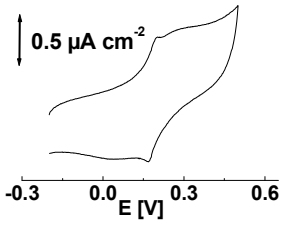  | AUT : DDT = 50 : 50 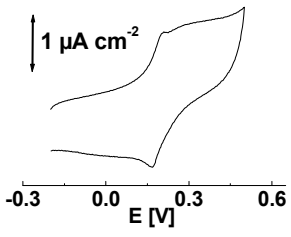  | 0.5887 |
| AUT : DDT = 25 : 75 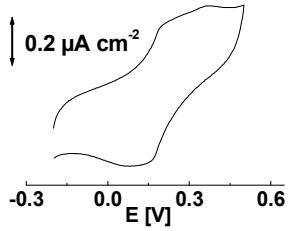  | AUT : DDT = 25 : 75 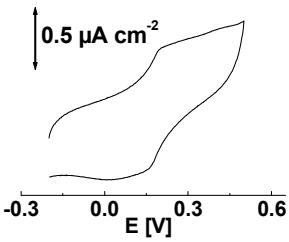  | AUT : DDT = 25 : 75 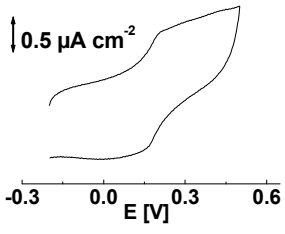  | 0.9776 |

# Appendix C

a

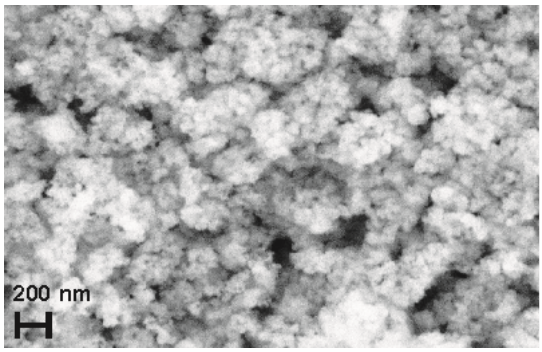


b

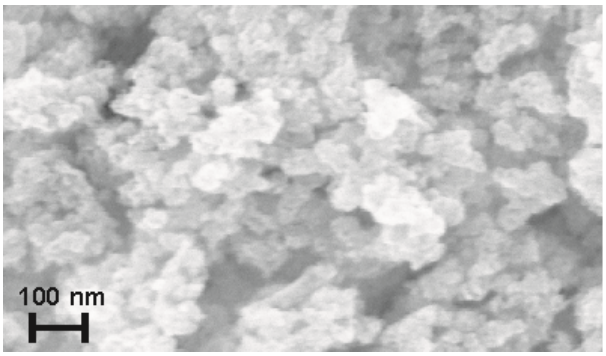


c

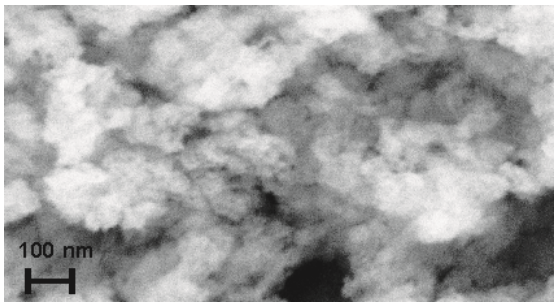


**Figure C.1** SEM micrographs of ATO

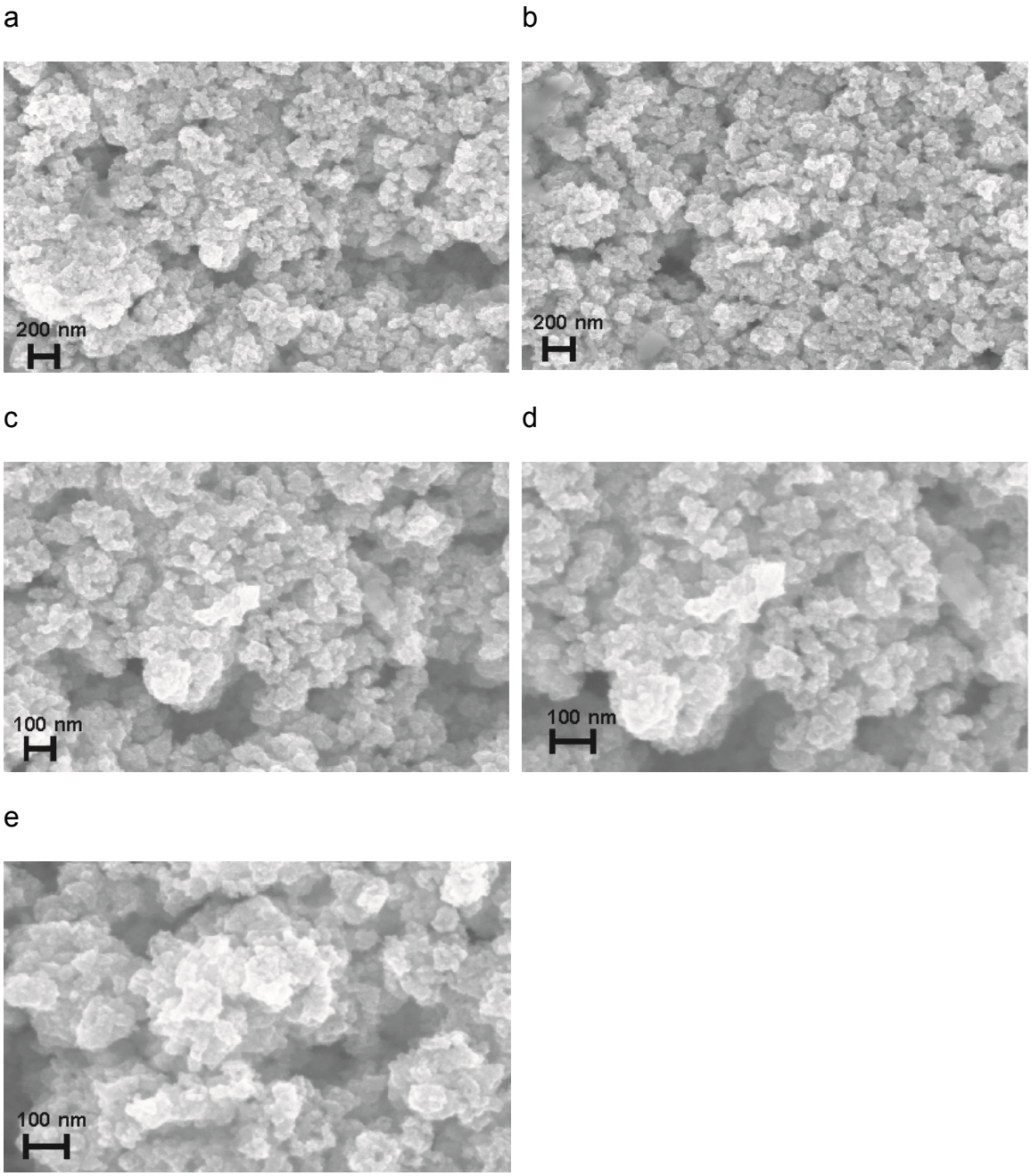


**Figure C.2** SEM micrographs of ATO/4$CeO_2$

a b

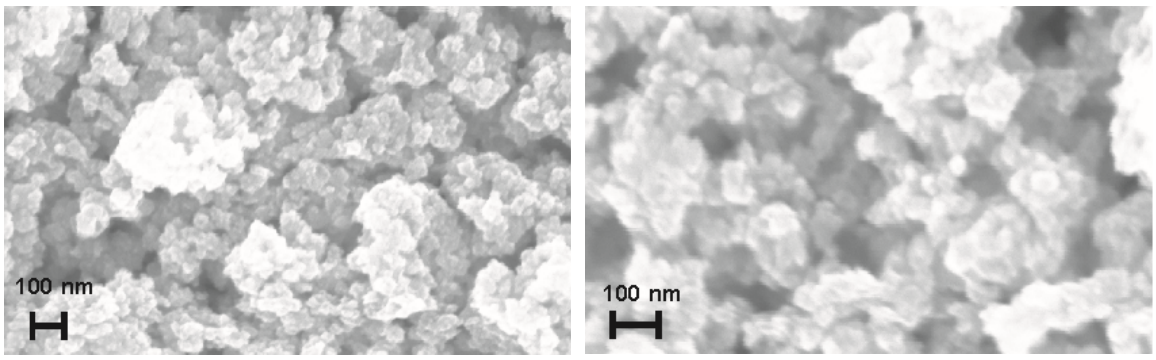


**Figure C.3** SEM micrographs of ATO/12 $CeO_2$

# List of Abbreviations

| | |
|---|---|
| SAM | Self–Assembled Monolayer |
| HDT | Hexadecanthiol |
| DDT | Dodecanthiol |
| AUT | Amino Undecanthiol |
| MUA | Mercapto Undecanoicacid |
| SECM | Scanning Electrochemical Microscopy |
| STM | Scanning Tunneling Microscopy |
| AFM | Atomic Force Microscopy |
| SEM | Scanning Electron Microscopy |
| CVD | Chemical Vapor Deposition |
| QCM | Quartz Microbalance |
| CV | Cyclic Voltammograms |
| EIS | Electrochemical Impedance Sepctroscopy |
| CPE | Constant Phase Element |
| FT–IR | Fourier Transformation Infra Red |
| XPS | X–ray Photoelectron Spectroscopy |
| NHS | *N*-hydroxysuccinimide |
| PMIRRAS | Polarization Modulation Infrared Reflection Absorption Spectroscopy |

# Declaration

I declare that this thesis is a summary of my work and all of material used for the thesis have been duly acknowledged and cited. I have not tried to get PhD degree before.

Osnabrueck, February 8, 2010

Ina Rianasari

# Biography

Ina Rianasari was born in Jakarta, Indonesia. She grew up in Jakarta where she attended school years. From August 1997 to February 2002, she moved to Surabaya – East Java to accomplish Bachelor degree in Chemical Engineering at Sepuluh Nopember Institute of Technology (ITS). During the Bachelor degree, she performed practical courses in petrochemical companies which motivated her to continue study. In October 2002, she was accepted as a master student in Martin Luther University Halle – Wittenberg and enrolled International Master Program “Applied Polymer Science”. After obtaining Master of Science (M.Sc), she joined Prof. L. Walder’s group at University of Osnabrueck in January 2006 as a graduate student and a member of “Non – Linear Optics” Graduate School.